Strategies Towards 3D Engineering of Biocompatible Hydrogels

Inaugural-Dissertation

zur

Erlangung des Doktorgrades

der Mathematisch-Naturwissenschaftlichen Fakultät

der Universität zu Köln

vorgelegt von

Caner Akıncı

aus Istanbul

Berichterstatter/in: Prof. Dr. Annette M. Schmidt

Prof. Dr. Simone Wiegand

Tag der mündlichen Prüfung: 12.12.2023

To my wife

Kurzzusammenfassung

In dieser Arbeit wird das vielseitige Potenzial synthetischer, biokompatibler Polymere zur Herstellung wohldefinierter Hydrogele durch verschiedene Vernetzungsstrategien untersucht. In der ersten Strategie wird der Einsatz von Triblock-Copolymeren auf Basis von Poly(ethylenglykol) (PEG) und Polycaprolacton (PCL) als physikalischen Gelatoren untersucht. Dazu werden PCL-PEG-PCL-Triblock-Copolymere in verschiedenen Blocklängen durch Ringöffnungspolymerisation von ε-Caprolacton unter Verwendung von PEG-Diolen (> 8000 g mol^{-1}) als Makroinitiator synthetisiert. Durch eine Kombination von Methoden wie Größenausschlusschromatographie (SEC) und Kernspinresonanzspektroskopie (^{1}H-NMR) wurden die Synthesebedingungen und der Reinigungsprozess unter Verwendung von Toluol als selektivem Lösungsmittel optimiert, um gut definierte Produkte mit unimodaler Molmassenverteilung zu erhalten. Die gereinigten PCL-PEG-PCL-Triblock-Copolymere werden systematisch analysiert, wobei der Schwerpunkt auf ihrem Sol-Gel-Verhalten und ihren thermischen Eigenschaften liegt. In der nächsten Strategie wird PEG als Matrixmaterial für photovernetzte Netzwerke durch extrusionsbasierten 3D-Druck verwendet. Zu diesem Zweck wird Poly(ethylenglykol)dimethacrylat (PEG$_{8K}$DMA) (8000 g mol^{-1}) mit einem hohen Funktionalisierungsgrad als Vernetzungskomponente verwendet. Um die optimale Zusammensetzung für den Druckprozess zu finden, wird die Lösungsrheologie eingesetzt, sowohl mittels Rotations- als auch Kapillarrheometrie. Dabei erweist sich PEG$_{100K}$ (100000 gmol^{-1}) als ein sehr guter Viskositätsverbesserer. Die systematische Untersuchung von wässrigen PEG$_{8K}$DMA-, PEG$_{100K}$- und deren binären PEG$_{8K}$DMA/PEG$_{100K}$-Lösungen mit unterschiedlichen Massenanteilen zeigt, dass das beobachtete komplexe Fließverhalten von der PEG$_{100K}$-Komponente dominiert wird. In den gedruckten Strukturen werden die PEG-basierten Hydrogelvorläufer mit UV-Licht von 365 nm und Lithiumphenyl-2,4,6-trimethylbenzoylphosphinat (LAP) als Norrish Typ-I-Photoinitiator effizient vernetzt. Dabei wird deutlich, dass die mechanische Integrität und die rheologischen Eigenschaften der photovernetzten Strukturen im Endprodukt von der PEG$_{8K}$DMA-Komponente dominiert werden. Im Hinblick auf die angestrebten Anwendungen werden Modellgitterstrukturen im Extrusionsdruckverfahren hergestellt und nachgehärtet, sowie die Verdruckbarkeit der formulierten Lösungen bewertet. Auf der Grundlage der rheologischen Eigenschaften der jeweiligen Lösung werden verschiedene Herstellungsparameter, wie z. B. die Nadelgeometrie, die Fließgeschwindigkeit und die Aushärtungsgeschwindigkeit getestet. Einige Lösungen, die aus einer PEG-basierten Zusammensetzung bestehen, werden als fortschrittliche Tinten für die Zellverkapselung in extrusionsbasierten 3D-Druckanwendungen vorgeschlagen. Im Rahmen der letzten Strategie wurden photolabile Hydrogele untersucht, die einen UV-labilen Vernetzer enthalten. Hierfür wurden die photochemischen Eigenschaften von drei verschiedenen photolabilen Vernetzern auf Basis von o-Nitrobenzyl (NB) zunächst in Lösung untersucht. Mittels UV-Vis-Spektrometrie werden wichtige Parameter wie der Extinktionskoeffizient, die Geschwindigkeitskonstante und die Quantenausbeute der Photoreaktionen bestimmt. Ein Photolinker (PL$_{carb}$), der eine carbamatverknüpfte labile Bindung enthält, zeigt hinsichtlich der Quantenausbeute eine bessere photolytische Aktivität als die anderen. Die Verbindungen werden mit Acrylamid copolymerisiert und bilden photolabile Hydrogele mit unterschiedlichem Vernetzungsgrad. Schließlich wird die Photodegradation durch UV-Bestrahlung im Gelzustand untersucht, indem die Quellung der Gele in Wasser während oder nach UV-Bestrahlung bei 365 nm verfolgt wird. Schließlich wird eine Top-Down-3D-Photostrukturierung von photolabilen P(AAm)-Hydrogelen durch µm-aufgelöste Multi-Photonen-Lithographie unter Variation der Prozessparameter wie Pulsenergie und Wiederholungsrate erreicht. Die Möglichkeit, z. B. fein verzweigte Gefäßsysteme in solche biokompatiblen Hydrogele zu strukturieren, gilt als vielversprechend für das mikroskalige Engineering von Hydrogelen, z. B. für Tissue-Engineering-Anwendungen.

Abstract

This thesis explores the versatile potential of synthetic, biocompatible polymers to create well-defined hydrogels by following different crosslinking strategies. In the first strategy, the employment of triblock copolymers based on poly(ethylene glycol) (PEG) and polycaprolactone (PCL) for a physical gelation is investigated. Therefore, PCL-PEG-PCL triblock copolymers are synthesized at various block length via ring-opening polymerization of ε-caprolactone, using PEG diols (> 8000 g mol^{-1}) as macroinitiators. Using a combination of methods such as size exclusion chromatography (SEC), nuclear magnetic resonance spectroscopy (^{1}H-NMR), and a purification process in toluene, it is optimized to result in well-defined products with unimodal molar mass distribution. The purified PCL-PEG-PCL triblock copolymers are systematically analyzed with focus on their sol-gel behavior and thermal properties. In the next strategy, PEG is used as the matrix material for photo-crosslinked networks by extrusion-based 3D printing. For this purpose, poly(ethylene glycol) dimethacrylate (PEG$_{8K}$DMA) (8000 g mol^{-1}) with at a high degree of functionalization is used as crosslinking component. To find the optimal composition for the printing process, solution rheology is employed, both by rotational and capillary rheometry. Here, PEG$_{100K}$ (100000 g mol^{-1}) is proven to be a very good viscosity enhancer. Systematic investigation of aqueous PEG$_{8K}$DMA, PEG$_{100K}$, and their PEG$_{8K}$DMA/PEG$_{100K}$ binary solutions at varying mass fractions show that the observed complex flow behavior is dominated by the PEG$_{100K}$ component. In the printed structures, the PEG-based hydrogel precursors are efficiently crosslinked using UV light of 365 nm and lithium-phenyl-2,4,6-trimethylbenzoylphosphinat (LAP) as a Norrish Type-I photoinitiator. In the final product, the mechanical integrity, and rheological properties of the photo-crosslinked structures are dominated by PEG$_{8K}$DMA component. Concerning the aimed applications, model grid structures are prepared by extrusion based printing and post-cured and evaluated concerning the printability of formulated solutions. On the base of the rheological properties of the respective solution, various manufacturing parameters, needle geometry, flow rate, and curing speed are tested. Some solutions consisting of PEG-based composition are suggested as advanced inks for cell encapsulation in extrusion-based 3D printing applications. In the last strategy, photolabile hydrogels containing a UV-labile crosslinker have been investigated. For this, photochemical properties of three different o-nitrobenzyl (NB)-based photo-labile crosslinkers are investigated initially in solution. Using UV-Vis spectrometry, important parameters such as the extinction coefficient, rate constant, and quantum yield of the photoreactions are determined. A photo linker (PL$_{carb}$) containing a carbamate-linked labile bond shows better photolytic activity than the others in terms of quantum yield. The compounds are copolymerized with acryl amide, forming photolabile hydrogels with varying degrees of crosslinking. In the gel state, photodegradation is examined by following the swelling response during or after UV irradiation at 365 nm. Finally, a top-down 3D photopatterning of photolabile P(AAm)-hydrogels is achieved through μm-resolved multi-photon lithography under variation of the process parameters such as the pulse energy and the repetition rate. The possibility to pattern e. g. finely branched vascular systems into such biocompatible hydrogels is highly promising for the micro-scale engineering of hydrogels, e. g. for tissue engineering applications.

Acknowledgment

CONTENTS

1 INTRODUCTION

Hydrogels represent hydrophilic polymers that expand when in contact with water, maintaining their structural integrity due to the presence of physical or chemical crosslinks.[1] These water-swollen gels are used in widespread applications such as for tissue regeneration[2] and facilitating and drug delivery. Hydrogels are highly favorable with remarkable viscoelastic properties owing to their soft and wet nature. It can be employed for cell encapsulation due to its advantageous attributes, including biocompatibility, structural similarity as an extracellular matrix, and customizable chemical and physical properties.[3]

Synthetic polymers are attractive materials to create hydrogels with reproducible properties. Their hydrogels can be fabricated depending on various gelation mechanisms. Physical crosslinking is utilized for responsive hydrogels with change of external stimulus, which assists entanglements, hydrogen bonding, hydrophobic associations, and crystallite microdomains.[4] Chemically crosslinking with various mechanisms, such as photopolymerization and free-radical initiation, can be employed by selecting functional polymers.[5] The crosslinking is crucial to design a hydrogel. It determines the mechanical properties defined as elasticity of modulus, which is proportional to stiffness. The stiffness of hydrogels can be modified according to polymer concentration and crosslinking ratio. Depending on tissue functions, Young's modulus ranges are between 0.1 kPa and 1000 kPa for native soft tissues and organs.[6–8]

Hydrogel precursors for light-mediated reactions, such as photopolymerization, photodegradation, and photopatterning, are attributed to physicochemical, mechanical, and biological properties. These characteristics play a pivotal role in shaping both the processing methods and the ultimate performance of the hydrogel.[9] Photopolymerization can be achieved through a multi-step process involving selective photo-crosslinking reactions of a light-sensitive prepolymer, creating precise architectures and heterogeneous compositions. Photofabrication methods demonstrate their ability to create 3D environments featuring intricate structures and diverse compositions. The fundamental concept of photopolymerization is to utilize monomers or oligomers in a liquid state to provide a solidification upon exposure to a specific wavelength of light.[10] During photocuring, photoinitiators play a crucial role, driving the photochemical reaction below 400 nm.[11] Conversely, photocleavable hydrogels consist of photolabile linkers, which enable real-time control of their tunable dynamic properties by irradiation of light or laser.[12] With the integration of light-based chemistry, hydrogels can permit spatiotemporal control and provide specific reactions within the volume of material by 3D photopatterning techniques.[13]

2 THEORETICAL BACKGROUND

2.1 Rheology

Rheology is a field of science that covers the flow and shear deformation properties of fluids and soft matters to understand their complex behavior.[14]
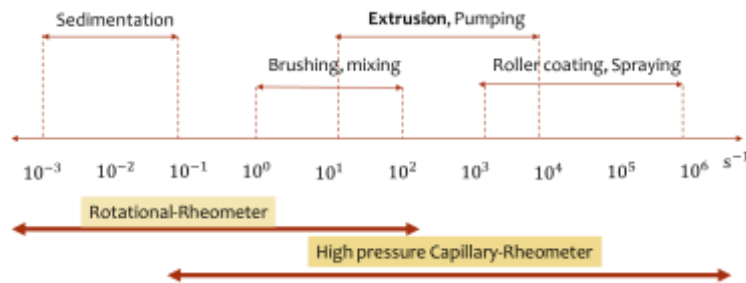
Figure 2.1. The range of shear rates in industrial applications.

Various industrial applications require deep knowledge of the rheological properties, including spraying, pumping, extrusion, and painting (Figure 2.1). Polymeric components are often used as a solution, ink, emulsifier, melt, and suspension agent for a formulation by varying their molar mass, concentration, and solvents. Both rotational and capillary extrusion rheometry are powerful techniques to understand complex behavior of polymeric systems for the addressed variables. [15–18]

Ideally, the viscosity of a liquid and the elasticity of a solid would follow the corresponding linear relationships of Newton's and Hooke's laws, respectively. However, most soft materials have viscoelastic properties, thus showing both elasticity and viscosity characteristics, leading to complex behavior. It is possible to understand the complex response of a material considering the basic parameters of modulus G and viscosity η. The viscoelastic properties can be modeled with these rheological terms. [19–21]
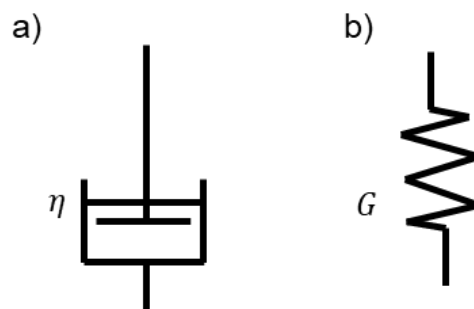
Figure 2.2. a) Dashpot model of a viscous liquid b) Spring model of an elastic solid.

Simple models can describe the behavior under shear or extensional deformations. This proportionality represents the response of an ideal elastic solid. In the dashpot model (Figure 2.2a), the ratio of the shear stress σ to the strain rate $\dot{\gamma}$ (defined as $\frac{d\gamma}{dt}$), gives the viscosity value.[21]

$$\sigma = \eta\dot{\gamma} \tag{2.1}$$

For the spring model (Figure 2.2b), the ratio of stress σ and strain γ is constant and equal to the shear modulus G.[21]

$$\sigma = G\gamma \tag{2.2}$$

These models can be combined to better describe more complex systems in series and parallel models. In contrast, in the case of a serial combination (Figure 2.3a), the Maxwell model describes a viscoelastic fluid, while in the case of a parallel combination (Figure 2.3b), the Kelvin-Voigt model is a model for a viscoelastic solid. [19–21]
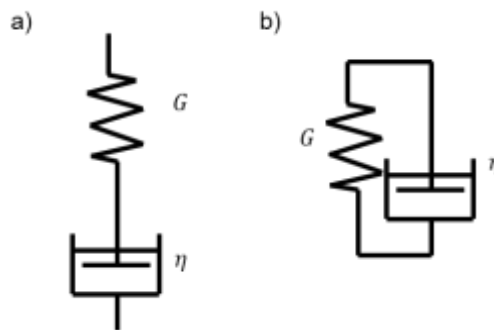
Figure 2.3. a) Maxwell model b) Kelvin-Voigt model.

On the other hand, the strain rate of a Maxwell fluid can be defined by the equation below:[21]

$$\dot{\gamma} = \frac{\dot{\sigma}}{G} + \frac{\sigma}{\eta} \tag{2.3}$$

For a Kelvin-Voigt solid, the stress required for a certain deformation:[21]

$$\sigma = G\gamma + \eta\dot{\gamma} \tag{2.4}$$

Both elasticity and viscosity contribute to both models' equations, which is the description of viscoelasticity.

Theoretically, the fundamental equations of a Hookean solid and a Newtonian liquid do not represent time-related behaviors. When viscous and elastic properties of materials are described in the full range of variables such as shear stress, strain, shear rate, and time, some limitations are observed. For instance, most polymeric solutions can show a shear-thinning or shear-thickening, mainly in a high

shear rate range. It can be described as a non-Newtonian fluid due to a deviation from shear rate dependency.

The comparison of the non-Newtonian fluids with Newtonian fluids as the function of shear rate is shown in Figure 2.4.
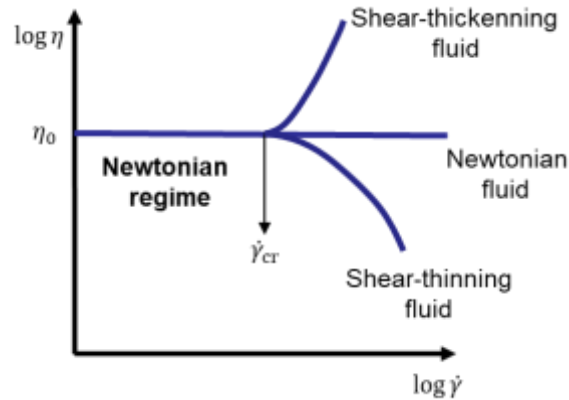
Figure 2.4. Typical viscosity-shear rate curves of Newtonian and non-Newtonian fluids.

Newtonian viscosity is not dependent on the shear rate. In contrast, non-Newtonian viscosity does not show a linear dependence with shear rate.

Its behavior is commonly seen as shear thinning or pseudoplastic flow, in which viscosity decreases with increasing shear rate. Generally, shear thinning flow shows a constant viscosity at relatively low shear rates, called the zero-shear viscosity η_0.

Shear-thickening is a less common non-Newtonian behavior seen in flow under shear, in which viscosity increases with increasing shear rate. A break in viscosity is observed at a critical shear rate $\dot{\gamma}_{cr}$ that determines the shear-thinning or shear-thickening behavior. A power law can mathematically describe the shear rate-dependent region.[14]

A flow curve can be interpreted to estimate the shear rate-dependent viscosity by the equation:[22]

$$\eta = K\dot{\gamma}^{n-1} \tag{2.5}$$

Here; K and n represent the curve-fitting parameters that are the flow consistency coefficient and the power-law index, respectively. For a shear-thinning behavior, the power-law index n is below unity. The smaller the value of the power-law index, the greater the shear-thinning behavior of the fluids. For a shear-thickening behavior, the power-law index is higher than unity. In the case of $n = 1$, Newtonian behavior is considered.

2.1.1 Rotational rheology

Rheological properties can be determined with the help of a shear or an extensional rheometer by performing static or oscillatory measurements. Different types of measurement geometries can be used in rotational rheometers. For the investigation of samples of very low viscosity, the concentric cylinder geometry is preferred, whereas the plate-plate and the cone-plate geometry are used for more viscous materials. A flow curve can be obtained by static measurements. In contrast, dynamic measurement depends on the response of the materials against sinusoidal stress and strain.[14] In case of oscillating values, their amplitudes are formed as two waveforms giving the maximum stress σ_{max} and maximum strain γ_{max} at a constant angular frequency ω.[14]
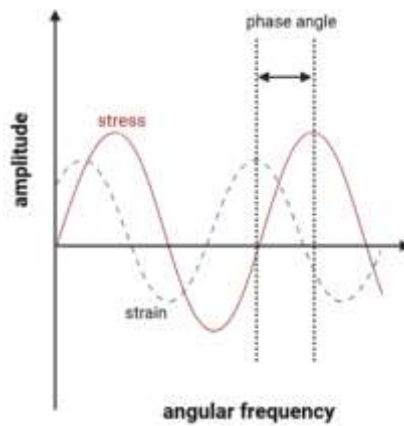
Figure 2.5. Oscillation forms of stress and strain.

The ratio between the oscillating values of σ_{max} and γ_{max} gives the complex modulus G^* as a function of frequency, ω.[14]

$$G^*(\omega) = \frac{\sigma_{max}}{\gamma_{max}} \tag{2.6}$$

δ is the phase angle indicating the time lag between stress and strain amplitude due to sinusoidal oscillation. δ for an ideal viscous liquid is $\frac{\pi}{2}$, while it is zero for an ideal elastic solid. For an ideal viscoelastic material, δ is measured between zero and $\frac{\pi}{2}$.[14]

The Maxwell model (equation 2.2) can be evaluated as the function of ω considering the deformation of a material under oscillation. The complex form of shear rate $\dot{\gamma}^*$ can be written as the function of frequency in the case of sinusoidal deformation.[23]

$$\dot{\gamma}^* = i\omega\gamma_0 e^{i\omega t} = i\omega\gamma^* \tag{2.7}$$

The complex stress $\dot{\sigma}^*$ can be calculated as:[23]

$$\dot{\sigma}^* = i\omega\sigma_0 e^{i(\omega t+\delta)} = i\omega\sigma^* \tag{2.8}$$

G^* is defined as the function of decay time, τ_m:[23]

$$G^*(\omega) = G'(\omega) + iG''(\omega) = G\frac{(\omega\tau_m)^2}{1+(\omega\tau_m)^2} + iG\frac{(\omega\tau_m)}{1+(\omega\tau_m)^2} \qquad (2.9)$$

Here, G' and G'' are the storage and loss modulus, respectively.

Considering the complex viscosity, η^* is:[23]

$$\eta^* = \frac{\sigma^*}{\dot{\gamma}^*} = \frac{\sigma^*}{i\omega\gamma^*} \qquad (2.10)$$

The relationship between G^* and η^* can be written as:[23]

$$\eta^* = \frac{G^*}{i\omega} = \frac{G'+iG''}{i\omega} = \frac{G''}{\omega} - i\frac{G'}{\omega} \qquad (2.11)$$

Similarly, η^* can be concluded as:[23]

$$\eta^* = \eta' - i\eta'' \qquad (2.12)$$

Thus,[23]

$$\eta' = \frac{G''}{\omega} \qquad (2.13)$$

$$\eta'' = \frac{G'}{\omega} \qquad (2.14)$$

In general, η' the real part of the complex viscosity explains the viscosity of the system and can be written as:[23]

$$\eta' = \frac{G\tau_m}{1+(\omega\tau_m)^2} \qquad (2.15)$$

The Maxwell decay time τ_m is: [23]

$$\tau_m = \frac{\eta}{G} \qquad (2.16)$$

Accordingly, η' goes to:[23]

$$\eta' = \frac{\eta}{1+(\omega\tau_m)^2} \qquad (2.17)$$

Hence,[23]

$$\eta'_{\omega\to0} = \eta \qquad (2.18)$$

Thus, for a Newtonian behavior,[23]

$$\eta = \eta(\dot{\gamma}) \qquad (2.19)$$

For a non-Newtonian behavior, viscosity is only valid at lower shear rate:[23]

$$\eta'_{\omega \to 0} \approx \eta(\dot{\gamma})_{\dot{\gamma} \to 0} \tag{2.20}$$

Accordingly, at low shear rates, the magnitude of η^* and v η' are almost equal. The situation can be expressed by:[23]

$$\eta^*_{\omega \to 0} \approx \eta(\dot{\gamma})_{\dot{\gamma} \to 0} \tag{2.21}$$

This expression shows that the contribution of imaginary part of complex viscosity (η'') can be ignored, and η' dominates the oscillation response.

In conclusion, viscosity of a viscoelastic fluid following the Maxwell model behaves like a viscous fluid at low frequencies. Regarding the flow behavior depending on shear rate and frequency, the Cox-Merz rule is commonly used for identifying similarities between the rheological results obtained from steady-state and oscillation tests.[24] The Cox-Merz rule states that the steady-state and complex viscosity are almost similar in equivalence situations.[24] For polymer liquids (solutions), considering the entanglement, the difference between $\eta^*(\omega)$ and $\eta(\dot{\gamma})$ is expected at a high shear rate region. As the difference becomes more distinct between η^* and η, polymer solutions indicate a weak gel behavior, $\eta(\omega) \gg \eta(\dot{\gamma})$. Hence, such polymer solutions cannot obey the Cox-Merz rule.[25] It will be explained in more detail in section 2.1.3.

2.1.2 Capillary extrusion rheology

Capillary rheometry is one of the simple methods to measure viscosity that can provide measurements between 10 s^{-1} - 10000 s^{-1} in the shear rate range.[26] A capillary method can be built simply consisting of a piston-like head, a reservoir, and a capillary layer. Figure 2.6 displays a developed simple capillary extrusion system. The plunger acts as a piston, which activates the movement of the fluid with the applied force into the needle at a velocity.

The theory of capillary extrusion accepts some assumptions for straight-forward data interpretation of some developed equations:[27]

- The flow through the capillary is steady.
- The capillary flow is isothermal.
- No slip conditions at the capillary wall during extrusion.
- The viscosity of the extruded fluid is not pressure-dependent.

According to the represented capillary extrusion system in Figure 2.6, a capillary shear stress and shear rate can be calculated according to the typical curve shown in Figure 2.7.
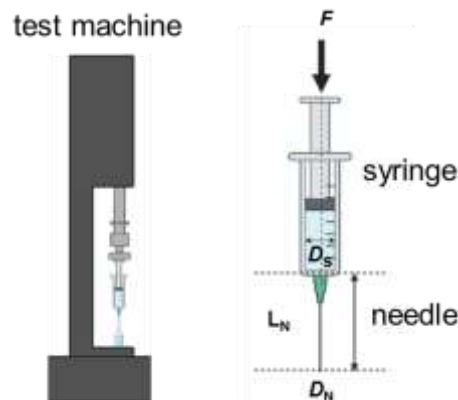
Figure 2.6. Schematic representation of the developed extrusion system.

The first regime represents the restoring forces criteria. The yield represents the transition to the stable flow regime and originates from relaxation processes within the extruded solution. This regime helps to understand the solutions which type of behavior, such as liquid-like and solid-like. The plateau is assigned to the resistance to flow through the capillary. The plateau force determines viscous force F_η, thus viscosity.
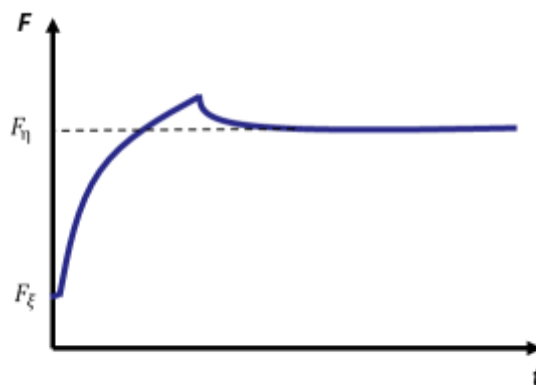
Figure 2.7. A typcial force-time curve obtained from capillary extrusion.

F_η is valid only for the force that results from the fluid's viscosity and flow in the capillary, the total of how much force acts upon the capillary setup. In a practical experiment, however, to set the flow in action, additional force is needed, which refers to the friction of the syringe plunger. It can be assumed to be constant throughout one experiment and independent of the flow rate. Thus, interception of F_ξ from the Poiseuille - Hagen equation is considered a constant. Thus, it is required for each data point to calculate F_ξ by using the plateau value and subtract the intercept value in the corresponding graph.

Under the appropriate conditions, the apparent shear stress can be defined as:[26]

$$\tau_{\text{app}} = \frac{\Delta p}{2L} \tag{2.22}$$

Δp is the pressure drop, and L is the length of the capillary. The shear stress is independent of fluid properties. According to the curve analysis seen in Figure 2.7, Δp can be considered as:[26]

$$\Delta p = \frac{\Delta F}{A} = \frac{F_\eta}{\pi R_{\text{S}}^2} \tag{2.23}$$

Hence;

$$\tau_{\text{app}} = \frac{R_{\text{N}} F_\eta}{2\pi R_{\text{S}}^2 L_{\text{N}}} \tag{2.24}$$

R_{S} is the radius of the reservoir (syringe). The shear rate $\dot{\gamma}$ can be defined as:[26]

$$\dot{\gamma} = \frac{4Q}{\pi R_{\text{N}}^4} \tag{2.25}$$

R_{N} is the radius of the capillary. Q is the flow volume can be calculated as:[26]

$$Q = \pi R_{\text{S}}^2 v \tag{2.26}$$

The apparent wall shear rate $\dot{\gamma}_{\text{app}}$ can be calculated as:[26]

$$\dot{\gamma}_{\text{app}} = \frac{4v R_{\text{S}}^2}{R_{\text{N}}^3} \tag{2.27}$$

However, the experimental analysis of capillary extrusion rheometry shows the real flow behavior as non-Newtonian.

As seen in Figure 2.8 non-Newtonian flow presents slip velocity at capillary walls. Mooney´s approach proposes the slip effect depending on flow rate.[28]

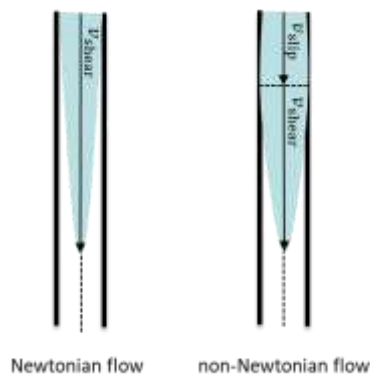Newtonian flow   non-Newtonian flow

Figure 2.8. Schematic representation of Newtonian and non-Newtonian flows through a capillary.

Firstly, n can be calculated, which is related to the shear-thinning effect of the flow through capillary wall, $n < 1$:[26]

$$\eta_{\text{app}} = K \cdot \dot{\gamma}_{\text{app}}^{n-1} \tag{2.28}$$

Assuming non-Newtonian flow, the Rabinowitsch correction is employed to calculate $\dot{\gamma}_{\text{w}}$ at the capillary wall:[26,29]

$$\dot{\gamma}_{\text{w}} = \left(\frac{3n+1}{4n}\right)\dot{\gamma}_{\text{app}} \tag{2.29}$$

The true wall stress τ_{w} can be calculated from:[26,29]

$$n = \frac{d \log \tau_{\text{w}}}{d \log \dot{\gamma}_{\text{app}}} \tag{2.30}$$

The true wall viscosity η_{w} is the ratio of the true wall stress τ_{w} to $\dot{\gamma}_{\text{w}}$:[26,29]

$$\eta_{\text{w}} = \frac{\tau_{\text{w}}}{\dot{\gamma}_{\text{w}}} \tag{2.31}$$

2.1.3 Entanglement

Polymers with their neighboring chains are associated in a solution at adequate molar mass or concentration. The associations can behave as crosslinking agents referring to polymer entanglement. Like rubber elasticity, the entanglement of polymers can be described as a physically crosslinked polymer. Long relaxation times, enhancement in the viscosity, and a rubbery region can appear in the rheology of the polymer solutions owing to the appearance of the entangled polymer network. Entanglement can be investigated by the function of polymer concentration in a solvent at a constant molar mass.[30] A viscosity-shear rate flow curve of polymer solutions typically exhibits three distinct regions, as illustrated in Figure 2.9.
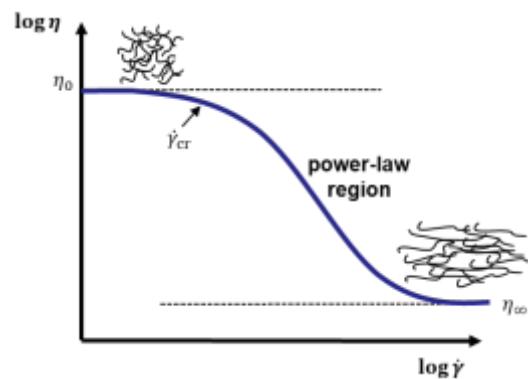

Figure 2.9. A typical viscosity flow curve of polymer solutions to demonstrate shear-thinning.

The viscosity becomes independent from the shear rate up to the critical shear rate, known as zero-shear or Newtonian viscosity. The second region is the shear-thinning region. Here, as the shear rate increases, the viscosity of the solution decreases. This phenomenon occurs as the polymer chains begin to align with an increase in the shear rate, represented by a power-law behavior or non-Newtonian flow. The polymer chains become extensively aligned at high shear rates in the third region. This alignment results in a dramatic reduction in the dynamic viscosities of the solution, a new plateau value defined as infinite shear viscosity η_∞ .[31]

Cross model[32] empirically explains the flow behavior of polymer fluids in a wide range of shear rates. It may be expressed as a kinetic interpretation of non-Newtonian flow[33], the proposed flow equation:

$$\eta = \frac{\eta_0}{1+(\lambda\dot{\gamma})^{1-n}} \tag{2.32}$$

λ is the relaxation time, in case of $\lambda = 1/\dot{\gamma}$, it indicates a transition from the Newtonian region to the power-law region. n is the flow index and measures the non-Newtonian characteristics.

A zero-shear viscosity-concentration graph plotted at log-log scale (Figure 2.10), polymer solutions can be categorized into three groups, dilute, semi-dilute, and concentrated. [31]
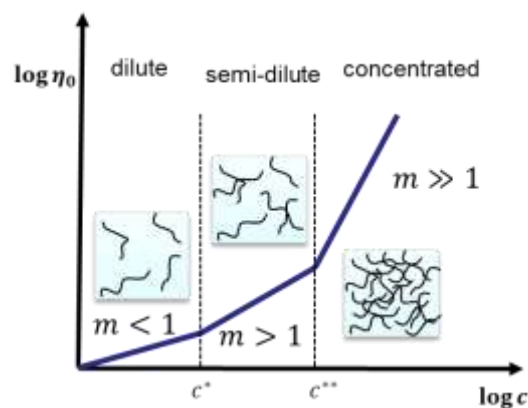
Figure 2.10. Determination of concentration regimes for polymer solutions.

In the diluted regimes, the polymer chains behave as ideal chains and isolate themselves from other chains. In the semi-dilute region, polymer chains can either be entangled or tightly filled with the solvent, which increases viscosity significantly. In the concentrated region, polymer chains behave highly stiff as entangled networks, and shear dependency significantly increases. The critical concentrations c^* and c^{**} indicate a transition from dilute to semi-dilute and from semi-dilute to concentrated regimes, respectively.[31]

2.2   Hydrogels

2.2.1   Classification of hydrogels

Hydrogels are crosslinked polymer networks that can swell by absorbing large amounts of water. The chemical structure of polymer networks determines the physical and mechanical properties of the hydrogels.[1] Hydrogels are made of physical crosslinking or chemical crosslinking (Figure 2.11). Chemical crosslinking can be achieved using chemical crosslinkers[34] or light irradiation.[35,36] Physical crosslinking physical crosslinking can be based on hydrogen bonds[37–39] ionic bonds [40,41] hydrophobic interactions[42] and environmental conditions, such as pH and temperature. Physically crosslinked hydrogels can show reversible properties thanks to dynamic interactions.[43] However, they are mechanically weak and lack of homogeneity.[44] In contrast, chemical crosslinking is not dynamic that is preferred mechanically strong hydrogels .[45] In most real hydrogels, their polymer network structures deviate from ideality because of defection, unreacted polymer chains, loops, and local entanglements are observed.[1]

Conventional hydrogels created from randomly crosslinked homopolymers provide limited opportunities to develop their properties. Monomer or polymer concentration can only be varied to adjust the crosslink density. Further, slow crosslinking process with uncontrollable crosslink density makes hydrogels mechanically unfavorable. On the other hand, a decrease in the polymer fraction results in a weak polymer network with a lack of energy dissipation.[46–48]
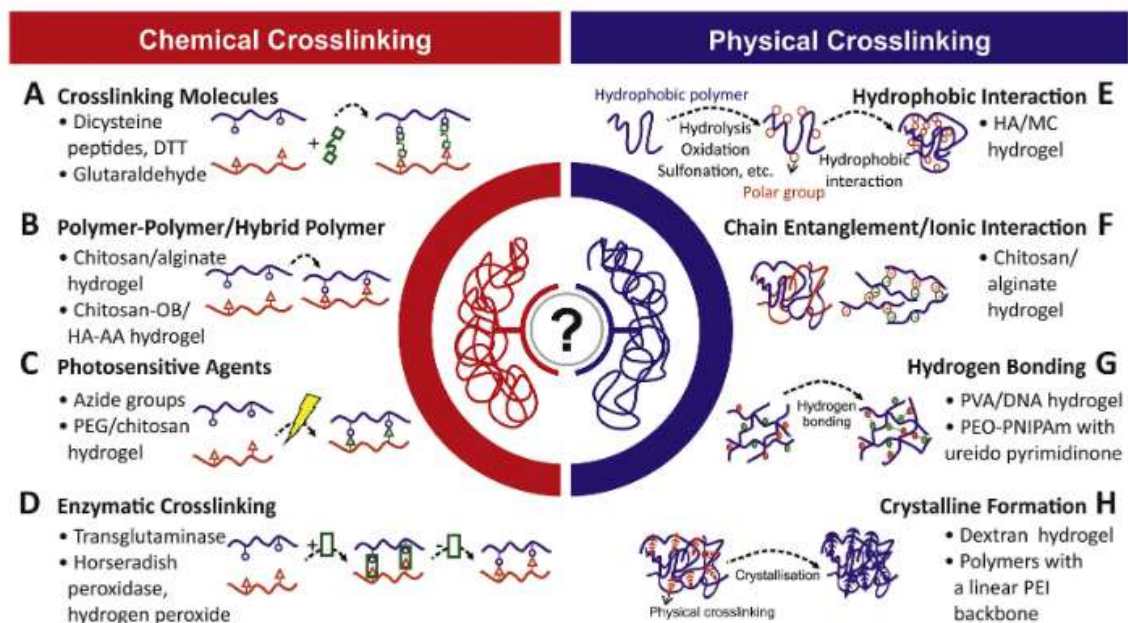

Figure 2.11. Crosslinking strategies in hydrogels. Reproduced from ref.[44] with permission.

One class of physically crosslinked hydrogels consists of block copolymers that can exhibit gelation from their sol state by triggering external conditions. Such a reversible transition from sol to gel in response to temperature or pH can be observed in aqueous solutions of PEG-based copolymers with polyesters[49], PAAm[50] and derivatives of Pluronic.[51] The resulting gel architecture can be formed depending on the micellar packing[52], hydrophobic association[53] and entanglement[54] of the diblock and triblock copolymers. Accordingly, polymers are classified into lower critical solution temperature (LCST) or upper critical solution temperature (UCST).[55] Considering the preparation methods, hydrogels can be categorized into several groups. If a polymer network is formed by one monomeric repeating unit or macromer, called as homopolymer hydrogel. When a network consists of different polymers defined as copolymer hydrogels.[56] On the he Interpenetrating network (IPN) hydrogels can be produced by the crosslinking of polymers separately In a different way, one component is chemically crosslinked, the other maintains the entanglements, defined as a semi-interpenetrating network (semi-IPN).[57] One origin for the superior strength of IPN and semi-IPN networks is micro-phase separation. The degree of the phase separation process depends on the density of entanglements and the viscosity of the precursors.[58,59] Concerning the properties, IPN and semi-IPN methods are preferred owing to improve the thermal and mechanical properties.[60] The decoration of hydrogel-forming polymers with functional groups is a powerful tool for tailoring hydrogel properties for specific needs. One of the techniques is the functionalization of synthetic or bio-polymers with (meth)acrylate groups.[61–63] The functional poly(ethylene glycol) diacrylates (PEGDA) or methacrylates (PEGDMA), gelatin methacrylate (GelMA), and methacrylated hyaluronic acid MeHA) can exhibit fast photo-crosslinking.[64] Their field of biomedical applications depending on their advantages are presented in Table 2.1.

Table 2.1. Properties of some photo-crosslinkable (meth)acrylated polymers in biomedical applications

Hydrogel	Property	Application
PEGDA	Long degradation, non-cell adhesive and tunable mechanical ability, high resistance to water absorption	Drug delivery[65–68] cancer model[69] Biosensing[70]
GelMA	Cell and tissue adhesive, tunable mechanical ability	Tooth[71], cartilage[72] nerve system[73], cardiac[74]
MeHA	High tumour targeting, mechanical ability, cell-adhesive	Drug delivery, cancer therapy[75–77], bone-tissue[78,79]

2.2.2 Network properties

Hydrogel properties, primarily mechanical properties and swelling, depend on several factors, such as network chemistry, type of solution and hydrogel structure (mesh or pore size), and drying conditions. Hydrogels with tunable properties can be obtained by regulating crosslinking ratio.[80] The crosslinking ratio, α is defined as:

$$\alpha = \frac{n_{\text{crosslinker}}}{n_{\text{monomer}} + n_{\text{crosslinker}}} \tag{2.33}$$

n_{monomer} and $n_{\text{crosslinker}}$ are the moles of monomer and crosslinker, respectively.

The crosslinking ratio regulates the statistical distance between two polymer nodes in a crosslinked network. The higher the crosslink ratio, the shorter the distance. In parallel, the crosslinker ratio establishes the swelling process of a hydrogel that is driven by the relaxation of the crosslinked chains. Hence, the higher the density of crosslinks, the less water is required to achieve equilibrium in chain flexibility.[80] Assuming isotopically change in the mass, volume, and dimension values of a hydrogel during swelling, the gel content G and the mass swelling ratio Q_{m} can be determined:

$$G\% = \frac{m_{\text{d}}}{m_{\text{monomer}}} \times 100 \tag{2.34}$$

$$Q_{\text{m}} = \frac{m_{\text{sw}} - m_{\text{d}}}{m_{\text{d}}} \tag{2.35}$$

Here m_{sw} and m_{d} represent the swollen mass and the dry mass of the hydrogel, respectively. m_{monomer} is the mass of monomers.

A critical parameter for hydrogels is mechanical property at a swollen equilibrium state. During swelling, crosslinks should provide mechanical stability to the hydrogel network. Hydrogels can store energy and also dissipate the applied force.
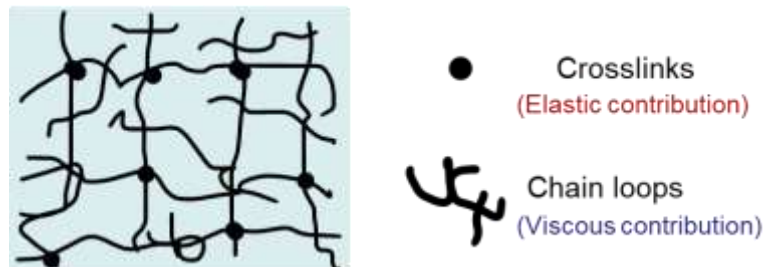

Figure 2.12. Polymer network of a real hydrogel.

However, as illustrated in Figure 2.12, crosslinking in a hydrogel can rarely be homogeneous.[80] Hydrogels with loop regions can exhibit limited mechanical performance in this case.[81] Hydrogels are complex materials for their viscoelasticity. The mechanical properties of hydrogels can be

quantitatively evaluated under deformation (see section 2.1). The structure–property relationships of hydrogels can be investigated by following the strain and frequency sweeps.

Figure 2.13 shows a typical curve obtained from strain-sweep. The strain-sweep test (amplitude-sweep) is a standard rheological test to characterize hydrogels using increasing oscillatory strain at constant frequency.
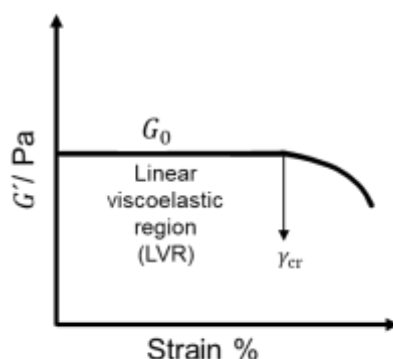

Figure 2.13. A typical strain-sweep curve of hydrogels.[44]

Strain-sweep describes linear viscoelastic region (LVR) in a strain range that demonstrates the ideality of a polymer network. Above the critical strain, $\gamma > \gamma_{cr}$, a hydrogel is deformable.[44]

With the determination of an appropriate strain, a frequency-sweep is performed to reflect the viscoelastic properties and crosslinking mechanism. Figure 2.14 shows typical curves obtained from frequency-sweep with an illustration of data interpretation.
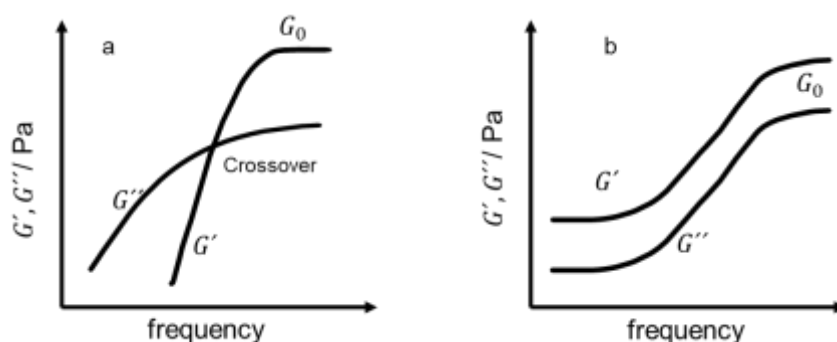
Figure 2.14. Typical frequency-sweep curves for A) physically crosslinked, and b) chemically crosslinked hydrogels.[44]

It is important that G' and G'' in a range of ω are incredibly dependent on the chain stiffness and dynamics of the hydrogels.[35] Physically crosslinked and hybrid hydrogels mostly show a crossover frequency ω_{cross} that indicates a reversible crosslinking mechanism $G' = G''$ (Figure 2.14a). In the case of $\omega < \omega_{cross}$, a liquid-like behavior is predominant, $G' < G''$. In contrast, in the case of $\omega > \omega_{cross}$, a solid-like behavior is observed, $G' > G''$., on the other hand, no crossover is observed in the

chemically crosslinked hydrogels[82], and the condition of $G' > G''$ is seen independent of the frequency (Figure 2.14b). The plateau modulus G_0 quantitively gives the mechanical properties of hydrogels. [44]

G_0 is proportional to α, described as:[83,84]

$$G_0 = \frac{\rho RT}{M_c} = \rho RT \frac{\alpha}{M_{monomer}} \tag{2.36}$$

where ρ is the polymer density, R is the universal gas constant, T is the absolute temperature, and M_c is the molar mass between crosslinks. An alternative can be form of independent from molar mass:

$$G_0 = \nu RT \tag{2.37}$$

where ν is the number of crosslink sites per unit volume.

2.3   Light-based 3D printing

Additive manufacturing is a powerful technology in tissue engineering, offering new possibilities for creating complex, and functional tissue constructs. To mimic natural tissues, 3D printing offers the design of the architectures of scaffolds at targeted geometry and pore sizes.[85] 3D printing can be integrated into cell seeding and encapsulation to fabricate biocompatible hydrogels with unique properties (see section 2.2) that maintain the requirements for living cells such as supplying oxygen and diffusion of nutrients.[48]

Hydrogels are materials as carriers for cells and bioactive substances in various bio-fabrication techniques, primarily in deposition-based methods. These techniques can be broadly classified into laser-induced forward transfer, inkjet printing, and robotic dispensing (Figure 2.15).[86] Each of these methods requires some qualifications in the hydrogel-based bioinks, particularly in terms of their rheological properties and photopolymerization kinetics.[48]

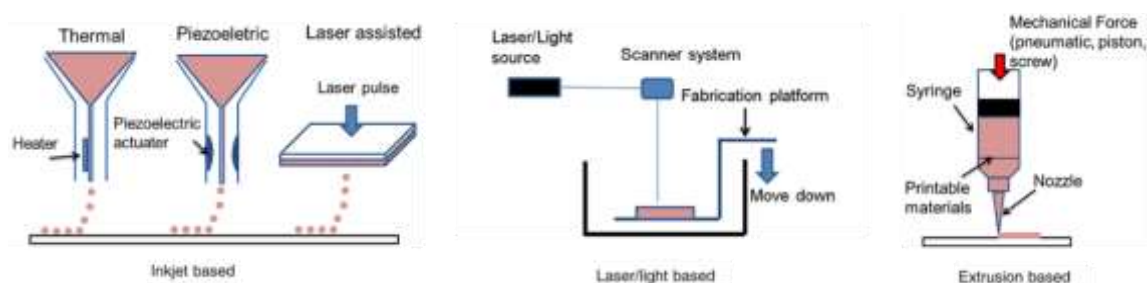Figure 2.15. Deposition-based 3D printing applications. Adapted from ref. [86] with permission.

However, manufacturing parameters such as nozzle geometry and pressure are important to keep the cell viability in extrusion-based 3D printing.[93–95] The principle of inkjet-based printing is to generate ink droplets onto a substrate, that can be carried out by different mechanisms such as thermal[87],

piezoelectric[88], and laser-assisted [89]. In laser/light-based printing, stereolithography, using laser or other light sources is used to pattern the surface of a photocurable material.[90] Extrusion-based printing depends on applying a mechanical force to extrude a ink or material.

Table 2.2 presents the advantages and drawbacks of these 3D printing techniques. Among them, for extrusion-based printers, one of the distinguishable properties is the ability of working conditions in a wide range viscosity, which gives the opportunity of the fabrication of various biocompatible materials including synthetic polymers.[91,92]

Table 2.2. The common 3D printing techniques

3D-Printing technique	Advantages	Disadvantages
Inject-based[96–98]	• Patterns with high resolution • Suitable for thin layers • Supportable with cells • 3D-structures with high resolution	• Long printing time • Limited to low viscous solutions • Poor mechanical properties
Laser/light-based[99]	• Photopolymerization with living cells possible • Easily-optimized printing parameters	• Small size Implementation • Complex printing operation
Extrusion-based[100–102]	• Controllable printing • High printing speed • Low damage to cells	• Low limited to resolution • High viscous inks • Effect of gelation and shear thinning on cell viability

For a biomaterial to serve as a suitable source of bioink, it must meet specific critical criteria. These criteria include biocompatibility, biodegradability, bioprintability, and the ability to maintain structural integrity after the printing process.[103,104] To fulfill these demanding requirements, researchers have

been actively formulating diverse bioinks. One key focus has been on achieving the desired mechanical properties necessary for successful 3D bioprinting.[105]

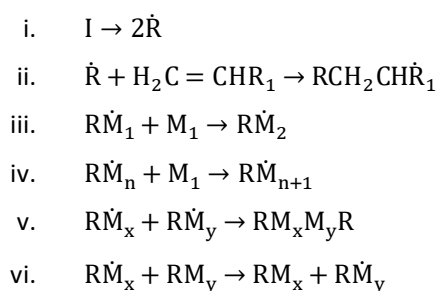Rheological properties play a pivotal role in determining the printability of hydrogels. In the context of 3D extrusion-based printing processes, several key rheological properties are crucial, including viscosity and viscoelastic shear moduli. Viscosity significantly influences both the precision of printing and the efficiency of cell encapsulation. In general, higher viscosities tend to result in better printing

fidelity.[106] However, it is essential to strike a balance because high viscosity also leads to increased shear stress, which can impact the viability of the cells suspended within the bioink. Thus, optimizing rheological properties is essential to achieving successful and biocompatible 3D bioprinting processes.[107]

2.3.1 Photopolymerization

Photopolymerization is a versatile and valuable technique for converting liquid monomers or macromers into hydrogels through free radical polymerization. This process allows for the rapid formation of hydrogels under ambient or physiological conditions, suitable for various biomedical and tissue engineering applications.[108] The process begins with selecting the appropriate monomers or macromers, like acrylamide or methacrylate derivatives, to form a hydrogel with tunable properties.[109,110] Photoinitiators are used in the precursors solution that are sensitive to specific wavelengths of light, such as ultraviolet (UV) or visible light. When exposed to the appropriate light source, photoinitiators create free radicals to initiate the polymerization process. Free radical photopolymerization is based on the chain growth shown in Scheme 2.1.[111]

Scheme 2.1. Mechanism of light-initiated free radical photopolymerization

$$i. \quad I \rightarrow 2\dot{R}$$
$$ii. \quad \dot{R} + H_2C = CHR_1 \rightarrow RCH_2CH\dot{R}_1$$
$$iii. \quad R\dot{M}_1 + M_1 \rightarrow R\dot{M}_2$$
$$iv. \quad R\dot{M}_n + M_1 \rightarrow R\dot{M}_{n+1}$$
$$v. \quad R\dot{M}_x + R\dot{M}_y \rightarrow RM_xM_yR$$
$$vi. \quad R\dot{M}_x + RM_y \rightarrow RM_x + R\dot{M}_y$$

In the representative mechanism, $H_2C = CHR_1$ presents the photopolymerizable monomer. I and R symbolize the photoinitiator and methyl or hydrogen group, respectively. (Scheme 2.1i) Upon irradiation, $C - C$, $C - Cl$, $C - O$ or $C - S$ bonds of the photoinitiator decompose to yield two free radicals. The available free radicals to trigger the chain growth reacting with a monomer (Scheme 2.1ii). It is followed by propagation in which the radical monomer grows with another existing monomer (Scheme 2.1iii) and (Scheme 2.1iv).[112]

For the termination step (Scheme 2.1v and Scheme 2.1vi), there are some possibilities:[111]

1. Two propagated chains can be combined or disproportionated.
2. A propagating chain can react with a radical of the photoinitiator.
3. Chain transfer might take play between free-radical molecules occurs.
4. Impurities, like oxygen or inhibitors, can interrupt the reaction mechanism.

Photoinitiators are generally split into two main groups: radical and cationic. The former is mainly used owing to their biocompatibility, while the latter is found toxic because of generating cations when exposed to the appropriate light.[108,113]

Radical photoinitiators are subdivided into two main groups. Type-I such as benzoin, and acetophenone derivatives, decompose into two primary radical molecules showing cleavage by absorbing photons. In contrast, type-II, such as benzophenone and thioxanthone, exhibit a hydrogen abstraction mechanism in the presence of a co-initiator yielding secondary radicals (Figure 2.16).[108,113]

Type-I photoinitiators generally exhibit superior photoinitiation efficiency compared to Type-II photoinitiators. The choice between Type-I and Type-II photoinitiators depends on the specific requirements of the application, including the desired wavelength range, photoinitiation efficiency, and safety considerations. Type-I initiators offer higher efficiency but are often used with shorter-wavelength light, while Type-II initiators are preferred when visible light or reduced toxicity is essential.[114]
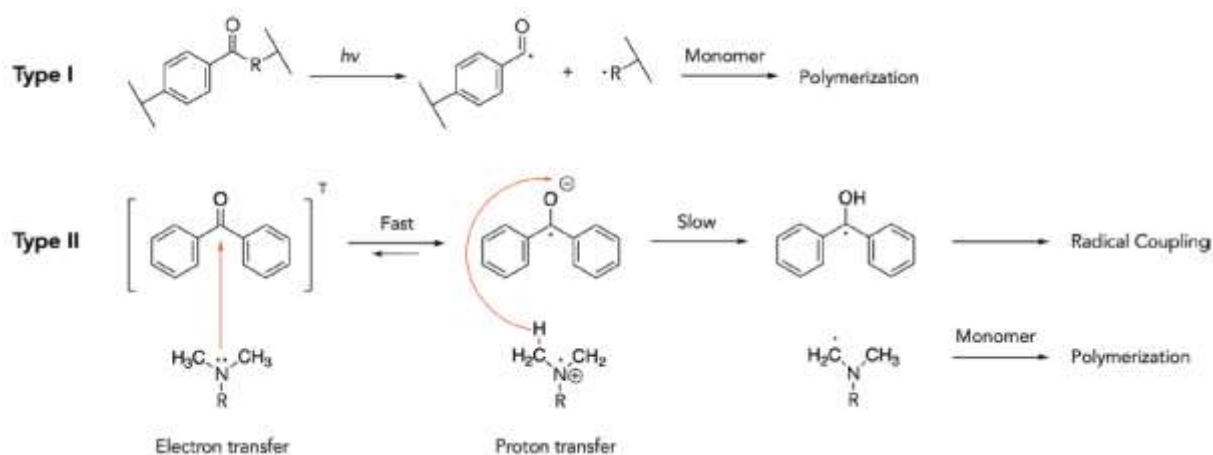

Figure 2.16. Type-I and Type-II mechanisms of photoinitiators. Reproduced from ref. [115] with permission.

Among the commonly used Type-I photoinitiators, I2959 and LAP are effective with nearly 365 nm UV light. However, due to its low molar absorptivity ($< 10 \, \text{L} \, \text{mol}^{-1} \, \text{cm}^{-1}$), I2959 requires a high concentration when it is used at 365 nm. In contrast, LAP has a relatively higher molar absorptivity ($\approx 200 \, \text{L} \, \text{mol}^{-1} \, \text{cm}^{-1}$), making it more efficient at lower concentrations. Additionally, LAP offers the advantage of being usable in the visible light range, specifically at 405 nm, with a lower molar absorptivity compared to its performance at 365 nm.[114]

Table 2.3. Typical photoinitiators with the wavelength of absorbance maximum

Photoinitiator	Type	λ_{max}
1-[4-(2-hydroxyethoxy)-phenyl]-2-hydroxy-2-methyl-1- propane-1-one (I2959) [116]	Type-I	274
Lithium phenyl-2,4,6-trimethyl benzoyl phosphinate (LAP)[117]	Type-I	375
2,2'-azobis [2-methyl-N-(2-hydroxyethyl) propionamide] (VA-086)[118]	Type-I	375
Eosin-Y[116]	Type-II	524
Tris (2,2- bipyridyl) dichlororuthenium (II) hexahydrate[119]	Type-II	453

Another commonly used photoinitiator is Eosin-Y, which can function as a Type-II photoinitiator when used in combination with a co-initiator and comonomer.[113] VA-086 photoinitiator has been reported to facilitate photopolymerization in the case of alginate methacrylate and gelatin methacrylamide through a free radical mechanism, particularly for cell post-encapsulation.[93,120] In the context of metal-based photoinitiators, tris(2,2-bipyridyl) dichlororuthenium(II) hexahydrate (Ru(II)(bpy)$_3^{2+}$ is employed as a photoinitiator with a co-initiator. An previous study describes the photopolymerization reaction involving silk fibroin, in which the photoinitiator serves as a catalyst, and ammonium persulphate (APS) functions as the electron acceptor to initiate free radical polymerization at 452 nm.[121]

Considering the reaction conditions, light source plays a crucial role in photopolymerization since it generates a reactive species after absorption.[112] To initiate a photopolymerization, such as halogen and household fluorescent lamps, laser diodes, LEDs, and black light UV lamps are used for photoinitiations. Some of the emission spectra of some exemplary light sources are represented in Figure 2.17.
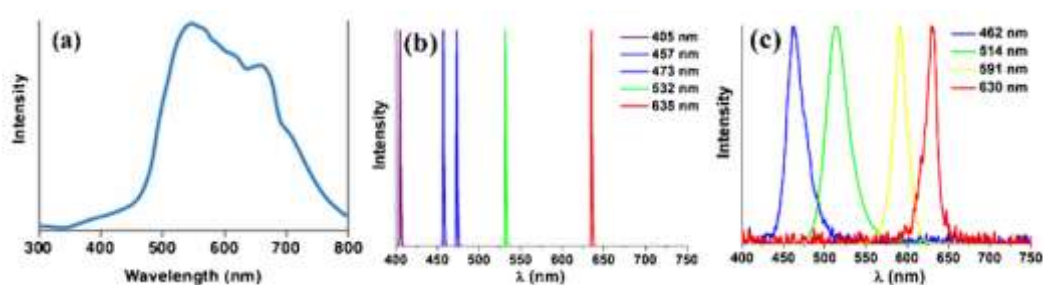

Figure 2.17. Typical emission spectra of (A) halogen lamps, (B) laser diodes, and (C) household lamps at different wavelengths. Reproduced from ref.[122] with permission.

Photopolymerization can be carried out in the wavelength range of 150 nm to 700 nm by selecting an appropriate light source. However, to diminish toxic effects risks, light-based systems for biomedical purposes typically operate within the range of 350 nm to 700 nm, ensuring the safety of biological tissues and organisms. Several preferred light sources are commonly used for these applications. Halogen and household lamps emit polychromatic light, covering a wide spectrum of wavelengths. The

control over the wavelength is the problem. Laser diodes provide monochromatic light, offering high precision and wavelength control. LEDs (Light-Emitting Diodes) offer quasi-monochromatic light. They are a flexible choice for various applications. Black-light UV lamps emit quasi-monochromatic ultraviolet light.[123]

2.3.2 Photodegradation and 3D photopatterning

Photochemistry has a profound impact on biological research, offering researchers the ability to both observe and precisely control cellular signaling processes. Recently, significant advancements have been made with the aim of utilizing light-mediated reactions to manipulate the chemical and physical properties of hydrogel-based cellular microenvironments with spatiotemporal precision. Moreover, it can be dynamically adjusted the stiffness of the matrix by employing light-induced secondary crosslinks, leading to the stiffening of the microenvironment. Conversely, photocleavage reactions can be employed to reduce the density of crosslinks, resulting in a decrease in microenvironmental stiffness. Collectively, these innovative approaches offer a versatile toolkit for investigating the impact of signals originating from the matrix, guiding the organization of cells, and influencing decisions related to cell fate.[124]

Consequently, manipulating the mechanical properties of the cellular microenvironment has become a central focus for researchers working on developing photo-responsive biomaterials. Achieving this objective involves modulating the crosslink density within the polymer network, which directly correlates with the material's modulus.

In a pivotal study, it is achieved that spatiotemporal control over reductions in the elastic modulus of PEG hydrogels by incorporating photocleavable units into the polymer network. It is also demonstrated that the modulus could be predictably reduced by precisely regulating the irradiation dose, provided the exposure time remained shorter than the critical time needed for complete degradation of the polymer network.[125] In a different study, a temporally controlled softening is revealed that exposing cells to stiffer substrates for extended durations during 2D culture predisposed them to undergo osteogenic differentiation.[126]

All referred study emphasizes that by providing the tunable mechanical properties by photocleavable hydrogels, the modulus of the polymer network is related to the cleaved crosslinks upon irradiation (Figure 2.18a). By investigating optimum crosslink density, critical light intensity, and exposure time, it is possible to regulate the stiffness of the degradable hydrogels.[125] The photocleavable polymer network can be fully degraded in light treatment above the critical irradiation time t_c and light intensity (Figure 2.18b).
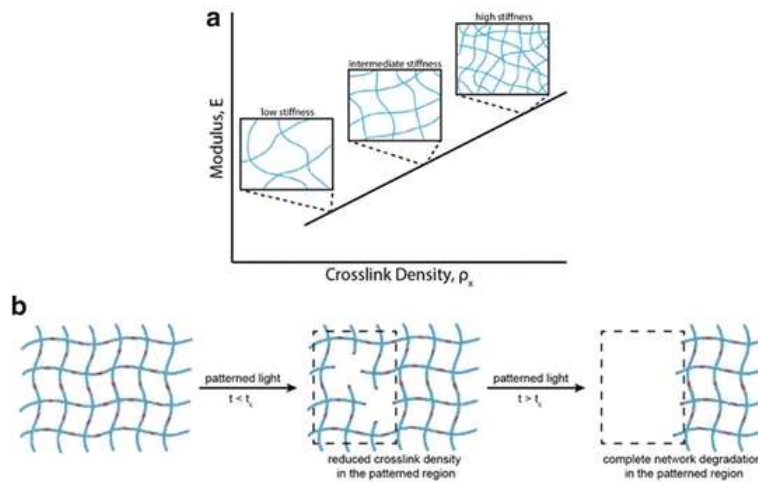
Figure 2.18. a) Relationship between crosslink density and modulus. B) Photodegradation of a polymer network. Adapted from ref.[124] with permission.

Considering the importance of photocleavage in chemistry and biology, photo linkers are the key component to controlling the response of biomaterials. Some parameters are considered for an ideal photolinker.[127,128] A photo linker should have an effective absorbance above the wavelength of 300 nm. Accordingly, the molar absorption coefficient ε $(\text{mol L}^{-1} \text{ cm}^{-1})$ is calculated by using the Lamber-Beer law.

$$A = \log\frac{I_0}{I} = \varepsilon c l \tag{2.38}$$

Here; A is absorbance, c (mol L^{-1}) is the molar concentration and l (cm) is the length of light beam through the sample. I_0 is the incident light intensity, and I is the exiting light intensity.

Quantum yield should be high that measures of the amount of the released cleaved group upon irradiation The quantum yield ϕ can be calculated using the following equation.

$$\phi = \frac{k N_A V h \upsilon}{I_0 \, 10^{-\varepsilon \cdot c \cdot d} A} \tag{2.39}$$

N_A is Avogadro's constant and V is volume of irradiated sample. h is the Planck's constant, υ is the frequency and I_0 the light intensity of light source. ε is the extinction coefficient at the irradiated wavelength. c is the concentration of irradiated sample. d is layer thickness, and A is the irradiated area. In addition, photo linker should be a selective compound and be stable in a photolytic system. The selected photo linker must be soluble in the targeted media.[128]

NB derivatives are one of the major photo linkers that can be removed in the UV and visible light wavelength range.
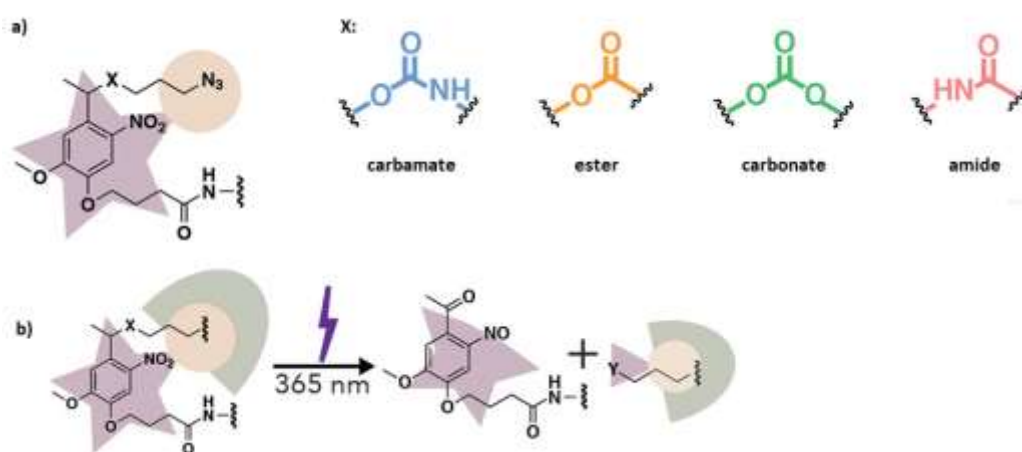
Figure 2.19. a) An example for NB-based photo linker with various labile bonds. B) Photohotocleavage of a NB-based photo linker at 365 nm. Adapted with permission from ref.[129]. Copyright 2020 American Chemical Society).

Figure 2.19a shows a modified NB-based photo linker with the different labile bonds at the benzylic position. The leaving group of NB-based photo linkers can consist of different photolabile linkers such as phosphates, carboxylates, carbamates, and alkoxides. The type of leaving group type directly affects the cleavage process related to reaction rate and quantum yield.[130] Concerning structural modification, firstly, aromatic ring formation of NB derivatives can be modified, and kinds of substitutions offer an increase in the molar absorption for a specific wavelength with an enhancement of quantum yields.[131,132] Secondly, the benzylic position can be altered to improve photochemical properties. A methyl group substitution at the benzylic position of NB is considered to trigger the cleavage kinetic and leads to more stable byproducts.[133] Similarly, a modification of the ring structure of NB with the methoxy group shifts the specific absorbance of the photo linkers to the higher wavelengths of light, although it decreases the quantum yield.[134] Considering the chemistry of the photodegradable groups with photocleavage properties at different states, NB-ester shows faster photolytic kinetic than NB-amide consisting of the same ring structures in the solutions state. However, the degradation rate of NB-amide decreases more in the case of an immobilization onto a solid-phase resin.[133,135] When these linkers act as crosslinks among PEG-based polymer network, the hydrogels, including NB-amide, shows slower degradation upon light irradiation than the hydrogels, including NB-ester.[136–139]

As seen in Figure 2.19b, the photodegradation is performed at a 365 nm light source, and their photolytic degradation is compared at the small molecule and hydrogel states. According to the photolabile moieties, the photodegradation rate of their hydrogels is calculated as (NB-carbamate > NB-ester > NB-carbonate > NB-amide). Interestingly, the quantum yield of NB-amide is the highest of the other photolabile small molecules in the solution state; it significantly decreases when used as a crosslinker for their PEG-*bis*-NB hydrogels.[129] It is understood that the chemical bonds of the polymer

network, in terms of hydrophilicity and hydrophobicity, impact the photodegradation performance of the related molecules.[131,132]

Photodegradable hydrogels have become valuable platforms for studying cell function, tissue engineering, and cell delivery due to their ability to control their physical and chemical properties using light dynamically. These hydrogel systems typically integrate photolabile o-nitrobenzyl (NB) derivatives into the hydrogel backbone. This choice is advantageous because these linkers can be cleaved through both one- and two-photon absorption processes.[140]

Photopatterning is a process which photosensitive materials respond to light, particularly based on photon absorption.[115] In photopatterning, the photosensitive material absorbs photons of specific wavelengths, leading to photochemical or photophysical changes within the material. These changes can include polymerization, crosslinking, or other chemical reactions that selectively occur in regions exposed to light. By controlling the intensity, wavelength, and duration of light exposure, it is possible to precisely pattern and manipulate photosensitive materials.[115] Apart from the chemical aspects, there are also crucial practical considerations to address the process of photopatterning. In the case of single-photon patterning, in photopatterning with traditional photolithography and masking techniques to facilitate the patterning process.[124]
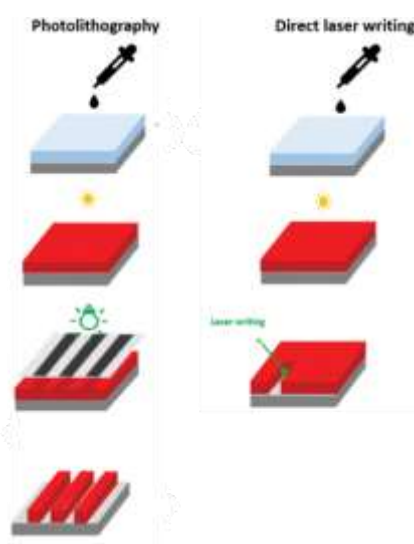

Figure 2.20. Comparison of photolithography and direct laser writing process for micropatterning of a network. Adapted from ref.[141] with permission.

While microscopy-based photopatterning can be accomplished using single-photon irradiation from visible light lasers, two-photon pulsed excitation offers significantly improved spatial resolution.[136] In contrast to single-photon excitation, two-photon excitation relies on lower-energy photons. The collective energy of two such photons become equivalent to the energy required for excitation.

In comparison to standard lithography, direct laser writing offers several advantages.[142] It streamlines the process by reducing the number of required steps and affords greater freedom in patterning through electronic control of the light source. Multi-photon lithography is a high-tech fabrication method to create 3D micro- and nanostructures based on multi-photon absorption initiated with a tightly focused pulsed laser. Ultrafast pulsed lasers with low duty-cycle can deliver femto-second, high-intensity bursts of photons to excite molecules locally and achieve a multi-photon absorption, without damaging the material.

3 CONCEPT OF THE WORK

The central concept of this thesis includes the synthesis of the characterization of novel synthetic polymers and the design of hydrogels based on different synthesis and crosslinking mechanisms for different manufacturing methods.

The first approach synthesizes PCL-PEG-PCL triblock copolymers at different lengths of PCL blocks initiated by macroinitiators PEG. It investigated the effect of synthetic conditions on the molar mass distribution, thermal properties, and aqueous behavior. Polymer characterization techniques, including SEC, ^{1}H-NMR, DSC, and DLS, are utilized to explain the structure-property relationships.

The second approach focuses on synthesizing highly functionalized $PEG_{8K}DMA$ for producing photo-crosslinked hydrogels, particularly for 3D printing applications. Polymer solutions are reinforced with a linear, high molar mass component of PEG_{100K} to adjust viscosity, making them suitable for use as inks. The rheological properties of binary solutions consisting of $PEG_{8K}DMA$ and PEG_{100K} are thoroughly investigated using rotational and capillary rheometry, with varying mass fractions of each component. Semi-IPN hydrogels are fabricated through photopolymerization in the presence of Type-I and Type-II photoinitiators at 365 nm and 405 nm, respectively. The properties of these hydrogels are explored through swelling measurements and rheological analysis. The printability of the formulated polymer solutions is assessed under different manufacturing parameters to facilitate the fabrication of hydrogels using extrusion-based 3D printing, followed by post-curing.

The third approach is to characterize the photocleavage properties of three photolabile linkers in solution and gel states. The photolytic activities of NB-based photo linkers are examined by UV-Vis spectrometry, focusing on labile bond chemistry. The molar extinction coefficient, photocleavage kinetics, and quantum yield of the photo linkers are determined by UV-Vis spectrometry. Copolymer hydrogels of P(AAm) are synthesized via redox-initiated free radical polymerization. The swelling behavior of the hydrogels are examined upon UV irradiation at 365 nm, enabling an assessment of gel-state photolytic activities. Finally, P(AAm) copolymer hydrogels incorporating carbamate labile bonds are patterned via multi-photon absorption. Process parameters are optimized during 3D photopatterning, considering the structural properties of the hydrogels.

4 RESULTS AND DISCUSSION

4.1 Structure-property relationships of triblock copolymers synthesized by ring-opening polymerization of ε-caprolactone using poly(ethylene glycol) macroinitiators

Amphiphilic block copolymers can spontaneously disperse in specific solvents that act as a good solvent for one block of the copolymer while serving as a poor solvent for the other.[143] When the segments consist of hydrophobic polyester blocks, such as PCL and hydrophilic PEG blocks, it is possible to modify the physical and chemical properties of their copolymers.[143] PEG possesses remarkable attributes, including hydrophilicity, water solubility, and non-toxicity, while PCL takes the attention with exceptional biocompatibility and biodegradability.[144,145]

The design of their block copolymers by ring-opening polymerization of ε-CL depends on various factors, such as monomer concentration, catalyst selection, and initiators. According to previous works, the role of monomer concentration in minimizing the cyclic oligomers is critical. [146] A broad molar mass distribution is observed when the ROP of lactones is initiated by alkali metal alkoxides or alkyls. [147] In contrast, alkoxyl derivatives of aluminum, zinc, and tin demonstrate a very efficient performance as a catalyst in controlling polydispersity.[148,149]

In this chapter, various PCL-PEG-PCL triblock copolymers are synthesized in presence of high molar mass PEG macroinitiators (>8000 g mol^{-1}), and Bu$_2$SO$_4$ as a catalyst. The thermal properties and aqueous behaviors of the triblock copolymers are explained according to synthetic conditions.

### 4.1.1 Effect of synthetic conditions on molar mass distribution

The PCL-PEG-PCL triblock copolymers are synthesized by coordination-inserted ROP of ε-CL initiated by PEG diols using Bu$_2$SnO as a catalyst. The synthesis of triblock copolymers is started with an azeotropic distillation of hygroscopic PEG$_{8K}$, PEG$_{35K}$, and PEG$_{100K}$ macroinitiators in toluene to remove water and moisture residues from the solvent at 65 °C. The corresponding amounts of ε-CL and PEG are reacted under an inert atmosphere at 130 °C for five hours. It is observed that the viscosity of the reaction solutions increases as the polymerization occurs, drastically so in the presence of PEG$_{100K}$ macroinitiators. The reaction is completed by cooling the synthesis solutions to room temperature. Adding enough chloroform dilutes the viscous reaction solutions, and the resulting solutions are

precipitated slowly in excess ice-cold petroleum ether 40/60. The filtered white powder raw products are obtained by drying at 35 °C under a vacuum.

Table 4.1. Synthetic conditions for preparing triblock copolymers and the experimental results for purified triblock copolymers by ¹H-NMR and SEC

POLYMER	n_{CL}/n_{MI}	n_{MI}/n_{cat}	$\bar{X}_n$	$\bar{M}_{n_{theo}}$ g mol^{-1}	$\bar{M}_{n_{NMR}}$ g mol^{-1}	$\bar{M}_{w_{SEC}}$ g mol^{-1}	$\bar{M}_{n_{SEC}}$ g mol^{-1}	$\bar{M}_w/\bar{M}_n$
PEG$_{8K}$	-	-	202	-	-	8940	8889	1.01
PEG$_{35K}$	-	-	723	-	-	33100	31870	1.04
PEG$_{100K}$	-	-	1320	-	-	107400	58150	1.85
C$_1$E$_8$C$_1$	17.70/1.01	3.4	17.5	10890	10531	n.d.	n.d.	n.d.
C$_1$E$_{35}$C$_1$	4.75/0.27	0.9	17.6	33878	33636	46250	44420	1.04
C$_1$E$_{100}$C$_1$	1.72/0.10	0.3	17.2	60113	58358	86060	50080	1.69
C$_3$E$_8$C$_3$	38.82/0.74	2.5	52.5	14878	16657	n.d.	n.d.	n.d.
C$_3$E$_{35}$C$_3$	12.99/0.25	0.9	52.0	37801	34725	44850	43850	1.01
C$_3$E$_{100}$C$_3$	4.99/0.09	0.3	55.4	64479	59079	101700	58840	1.73
C$_5$E$_8$C$_5$	49.84/0.57	1.9	87.4	18871	24239	n.d.	n.d.	n.d.
C$_5$E$_{35}$C$_5$	19.63/0.22	0.8	89.2	42055	36647	31560	28560	1.11
C$_5$E$_{100}$C$_5$	7.98/0.09	0.3	88.7	68271	59723	74900	41010	1.83

Scheme 4.1. Ring-opening polymerization of ε-CL initiated by PEG diols in presence of Bu₂SnO
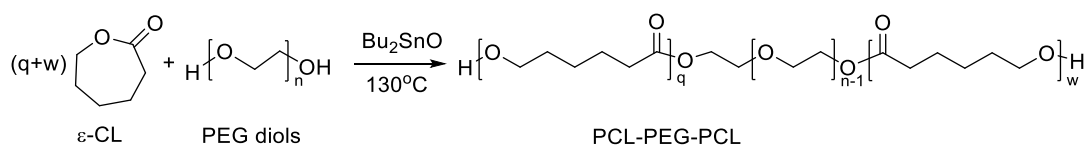
The synthetic conditions of triblock copolymers are designed by the molar mass of macroinitiator, $\bar{M}_{MI}$ and the polymerization degree of ε-CL, $\bar{X}_n$. The total mass of triblock copolymers $\bar{M}_n$ is calculated by:

$$\bar{M}_n = (2\bar{X}_n M_{CL}) + \bar{M}_{MI} = (\frac{n_{CL}}{2n_{MI}}M_{CL}) + \bar{M}_{MI} \tag{4.1}$$

Here, M_{CL} is the molar mass of the monomer, n_{CL} and n_{MI} are the moles of ε-CL and PEG macroinitiators, respectively. According to the desired molar masses of each block, all experimental conditions are presented with synthesis results in Table 4.1.

According to the described synthetical procedure, nine PCL-PEG-PCL triblock copolymers with three different polymerization degrees and compositions initiated by the PEG diols at three molar masses are synthesized. The nomenclature of the triblock copolymers is organized by the theoretical PCL molar mass of one PCL block and the molar mass of PEG. For instance, $C_1E_8C_1$ represents a molar mass of the PEG macroinitiator of 8000 g mol^{-1} and the expected molar mass of each PCL block of 1000 g mol^{-1}, respectively. Since PEGs act as macroinitiators in the performed reactions with the diol functional group, the polydispersity of the macroinitiators must be considered in the synthesis. SEC results of triblock copolymers and macroinitiators shown in Figure 4.1.
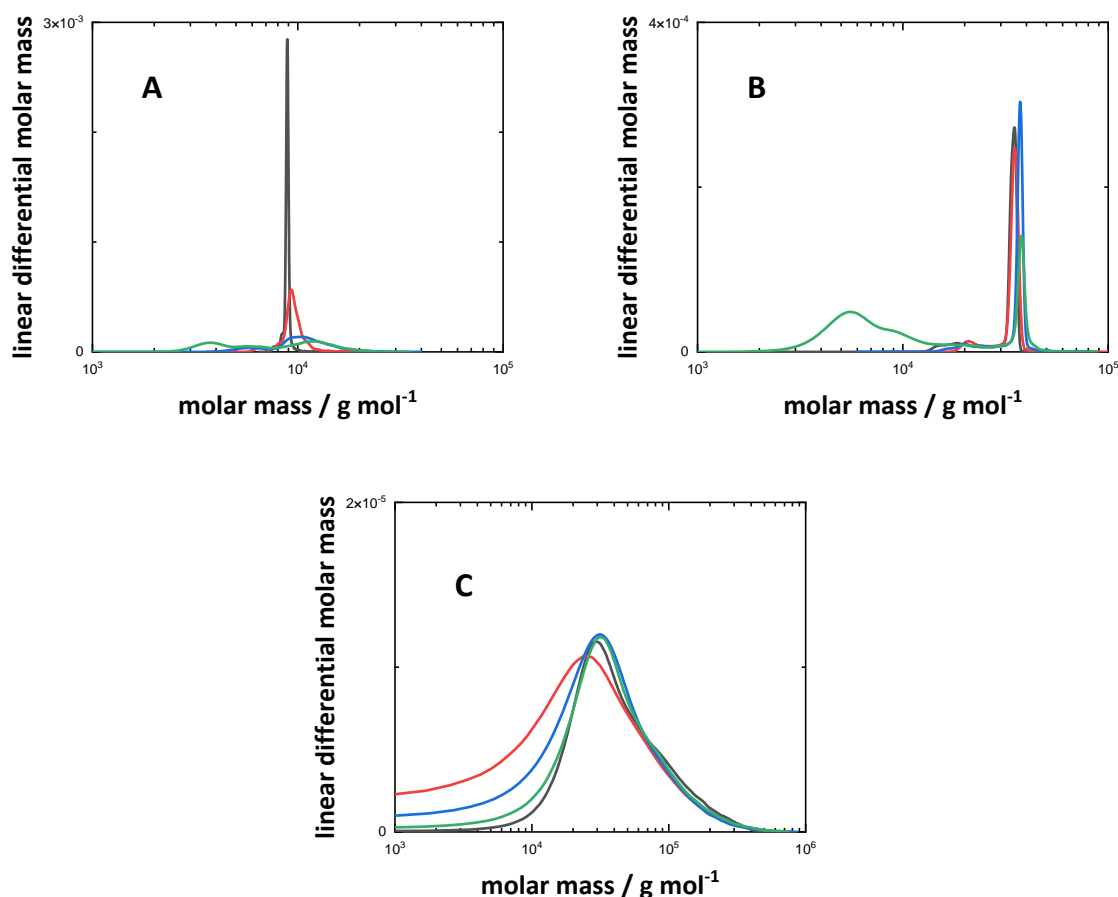
Figure 4.1. SEC results of raw triblock copolymers and macroinitiators. A) PEG$_{8K}$ (black), $C_1E_8C_1$(red), $C_3E_8C_3$ (blue), $C_5E_8C_5$ (green) B) PEG$_{35K}$ (black), $C_1E_{35}C_1$(red), $C_3E_8C_3$ (blue), $C_5E_{35}C_5$ (green) C) PEG$_{100K}$ (black), $C_1E_{100}C_1$(red), $C_3E_{100}C_3$ (blue), $C_5E_{100}C_5$ (green).

The molar mass distribution of PEG$_{8K}$ is very narrow, but it is moderate and broader for PEG$_{35K}$ and PEG$_{100K}$, respectively. The low molar mass of commercial PEG is synthesized by the reaction of ethylene

oxide with water, anionic polymerization,[150] thus a narrow molar mass distribution. In contrast, the high molar mass PEGs are produced by polycondensation, yielding higher polydispersity.

Although the PEG$_{8K}$ macroinitiator has a narrow molar mass distribution, its triblock copolymers are broad and multimodal. In the triblock copolymers initiated by PEG$_{35K}$, the new peaks are seen at lower molar masses than the molar mass of the PEG$_{35K}$ macroinitiator. PEG$_{100K}$-initiated PCL-PEG-PCL triblock copolymers demonstrate a broad molar distribution proportionally to PCL polymerization degrees. We consider the growing peaks at lower molar masses to be PCL-rich macromolecules as byproducts. The following findings literature[151], the reasons are emphasized: Bu$_2$SnO is a transesterification catalyst. The protic PEG macroinitiators are chain transfer agents. Some uncontrollable experimental reasons exist, such as water residues and moisture traces.

The hypothesis of the low molar mass side products being rich in PCL can thus be separated by fractionation is investigated. Initially, a suitable solvent that behaves as a good solvent for PCL-rich chains is selected. The Huggins constants for PCL and solvent $\chi_{solvent-PCL}$ with Hildebrand solubility parameters δ are considered to determine a fractionation solvent.

Table 4.2. Some of solubility parameters for PCL in various organic solvents

Solvent	Huggins	Hildebrand (MPa)$^{1/2}$	
	$\chi_{solvent-PCL}$	δ	H-bonding tendency
Toluene	0.08	18.2	poor
Cyclohexane	0.88	16.8	poor
n-butane	1.22	13.9	poor
THF	0.13	18.6	intermediate
Ethanol	1.01	26.8	strong

Considering this parameter, toluene is chosen as the suitable solvent for PCL fractionation at room temperature. Toluene has a good Huggins value and poor H-bonding tendency, as seen in Table 4.2.[152,153] According to the Huggins parameters and poor H-bonding tendency, toluene is decided as a suitable solvent for purification. The fractionation of the raw PCL-PEG-PCL triblock copolymers is performed at the concentration of 10 w/v % to follow solvent power impacts. The supernatant contains the PCL-rich, soluble fraction. The triblock copolymers are precipitated as insoluble fractions. The

fractionation of the raw PCL-PEG-PCL triblock copolymers is performed at the concentration of 10 w/v % to follow solvent power impacts, as illustrated in Figure 4.2 . Using toluene as solvent it is known that:

- The supernatant contains the PCL-rich, as soluble fraction.
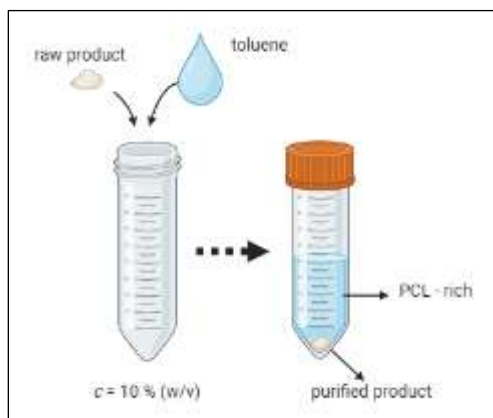- The triblock copolymers are precipitated, as insoluble fraction.

Figure 4.2 Schematic illustration of fractionation.

As a result of fractionation, the soluble mass fractions increase with the number of PCL repeating units, while the insoluble fraction increases proportional to the number of PEG repeating units.

Table 4.3. The insoluble μ_{ins} and soluble μ_{sol} mass fractions calculated from the purification in toluene

Triblock copolymers	μ_{ins}	μ_{sol}
$C_1E_8C_1$	0.68	0.32
$C_3E_8C_3$	0.09	0.91
$C_5E_8C_5$	0.08	0.92
$C_1E_{35}C_1$	0.88	0.12
$C_3E_{35}C_3$	0.80	0.20
$C_5E_{35}C_5$	0.62	0.38
$C_1E_{100}C_1$	0.95	0.05
$C_3E_{100}C_3$	0.95	0.05
$C_5E_{100}C_5$	0.92	0.08

In addition, we observe that the soluble fractions vary from viscous liquid to jelly-like depending on the amount of PCL side product in agreement with the selection of good solvent for PCL.

To better compare the SEC elugrams before and after the fractionation process, we perform a multiple peaks fit analysis to the elugram using Gaussian equation.[154]

$$y = y_0 + \left[\frac{A}{w\sqrt{\frac{\pi}{2}}}\right]\left[e^{\left[\frac{-2(x-x_C)}{w}\right]^2}\right] \tag{4.2}$$

The base of curves y_0, the area $A > 0$, the full width of the half maximum w, and the center of the peak x_0 are the parameters of the Gaussian function.

Accordingly, Figure 4.3 shows deconvoluted SEC measurements of the raw and the purified $C_5E_{35}C_5$ triblock copolymers. The SEC results of the raw $C_5E_{35}C_5$ show multimodal distribution before purification. There are four prominent deconvoluted peaks detected as sub-fractions. Firstly, the smaller fractions are obtained at the molar mass of 5415 g mol^{-1} and 8550 g mol^{-1}. Secondly, there is a broad fraction but a very high molar mass at 29359 g mol^{-1}. Finally, the sharpest peak is convoluted at 37774 g mol^{-1}. The relative area of the peaks at the highest degree of polymerization is calculated as 0.770, and the fractionated insoluble mass fraction is calculated as 0.623 by gravimetric analysis. It is observed that toluene allowed the purification of the triblock copolymer in good agreement with the theoretical considerations mentioned above.
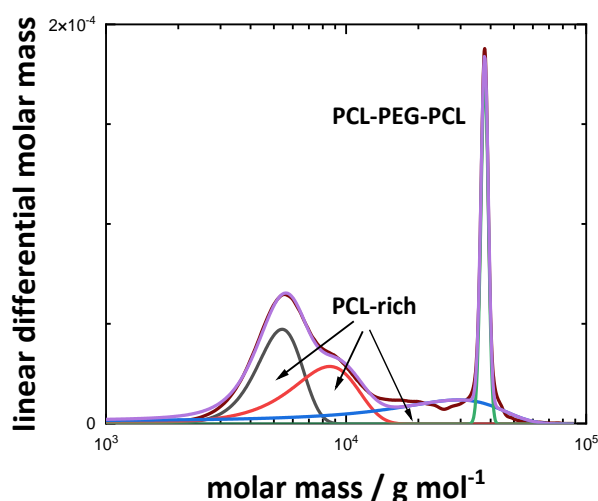
Figure 4.3. The deconvoluted SEC curve of raw $C_5E_{35}C_5$ with the peaks fitted by Gaussian function.

Figure 4.3 displays that the molar mass distribution of PCL-PEG-PCL triblock copolymers is significantly narrowed to their macroinitiators after purification. The challenge in fractionation is observed in the PCL-PEG-PCL triblock copolymers initiated by PEG$_{8K}$. Due to the presence of comparatively higher hydrophobic PCL blocks, $C_1E_8C_1$, $C_3E_8C_3$, and $C_5E_8C_5$ are almost dissolvable in toluene, making fractionation inefficient.
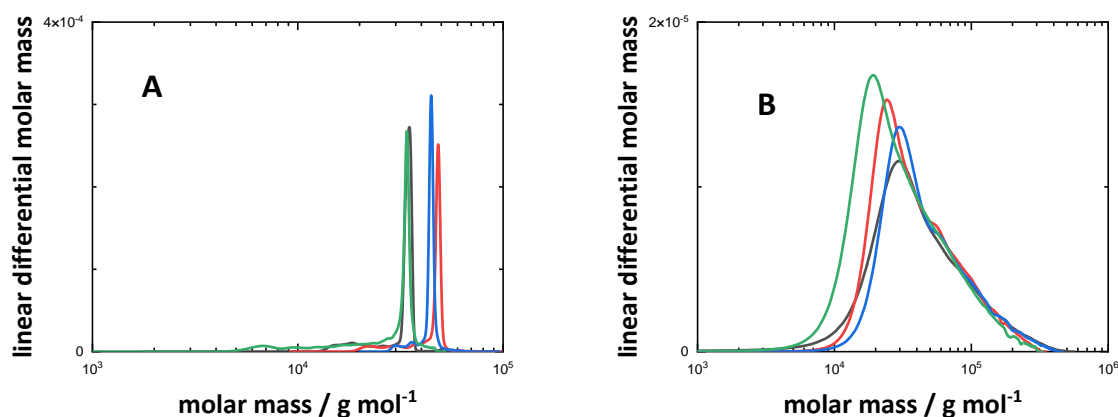
Figure 4.4. SEC of THE purified triblock copolymers comparison with macroinitiators. A) PEG_{35K} (black), $C_1E_{35}C_1$(red), $C_3E_8C_3$ (blue), $C_5E_{35}C_5$ (green) B) PEG_{100K} (black), $C_1E_{100}C_1$(red), $C_3E_{100}C_3$ (blue), $C_5E_{100}C_5$ (green).

The SEC results of the purified triblock copolymers initiated by PEG_{35K} and PEG_{100K} demonstrate quite a narrower molar mass distribution than their raw states. The peaks indicating the low molar mass formations disappear with purification in toluene. Thus, a significant improvement of the polydispersity of PCL-PEG-PCL triblock occurs with PCL-rich separation. It is found that the average-number molar mass of triblock copolymers shifts to a lower molar mass after purification of PCL-rich molecules. It might also be due to modifying the diol end groups with PCL.

In addition to the SEC measurements, end-group analysis of the synthesized PCL-PEG-PCL triblock copolymers is supported by ^{1}H-NMR.
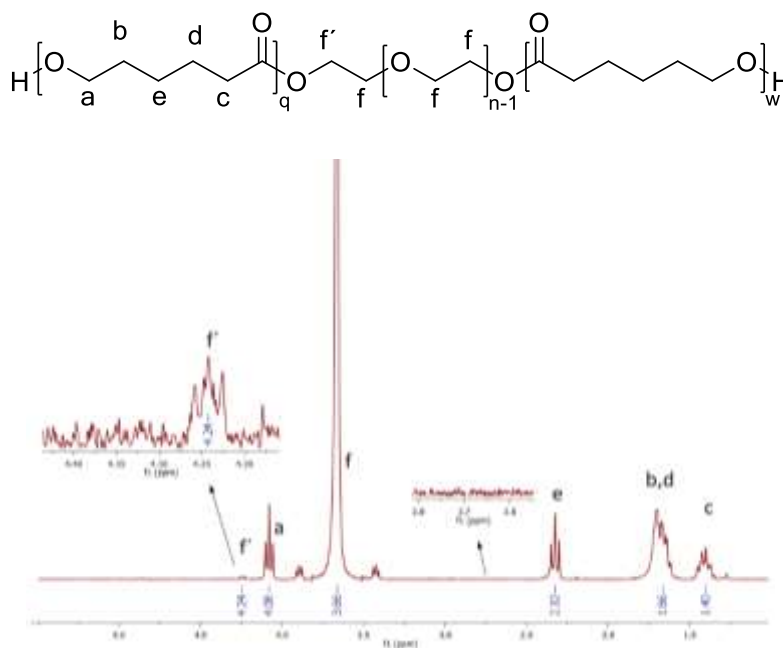
Figure 4.5. Proton groups of PCL-PEG-PCL triblock copolymers, and ^{1}H-NMR spectrum of the purified $C_5E_{35}C_5$ triblock copolymer.

33

As seen in Figure 4.5, the methylene protons of ε-CL repeating units are characterized at 4.24, 4.08, 2.32, 1.66, and 1.40 ppm assigned to *f′, a, e, b-d,* and *c*, respectively. The methylene protons of the ethylene glycol repeating units appeared at 3.66 ppm, symbolized as *f.*

The typical spectrum of the triblock copolymers presents the typical end-group analysis of a PCL-PEG-PCL triblock copolymer by ^{1}H-NMR with characteristic peaks. The ethylene glycol repeating units are proved with a peak at 3.66 ppm. The signal at 4.24 ppm indicates the junction to PCL terminated blocks. No signal is observed at 2.64 ppm, indicating an absence of unreacted ε-CL monomer.

Using the corresponding peaks, the total number-average molar mass of each triblock copolymer $\bar{M}_{n_{NMR}}$ is calculated according to the total number-average degree of polymerization $\bar{X}_{n_{PCL,NMR}}$.

$$\bar{X}_{n_{PCL,NMR}} = \frac{2I_e}{I_f} \bar{X}_{n_{PEG}} \tag{4.3}$$

$$\bar{M}_{n_{NMR}} = \frac{2I_e}{I_f} \bar{X}_{n_{PEG}} + \bar{M}_{n_{PEG}} \tag{4.4}$$

I_e and I_f are the integrals of the corresponding peaks at 2.30 and 3.60 ppm, respectively. Here, $\frac{2I_e}{I_f}$ is the ratio of the total repeating unit of ε-CL to ethylene glycol units. Using the integrals of the specific peaks to the PCL and PEG blocks, $\bar{M}_{n_{NMR}}$ of the triblock copolymers is calculated to reinforce $\bar{M}_{n_{SEC}}$ as seen in Table 4.1.

Based on the fractionation, the soluble and the insoluble fractions are evaluated to estimate the ratio of the number of growing PCL-rich chains to the purified PCL-PEG-PCL triblock copolymers. Accordingly, the ratio of hydrophobic repeating units of PCL, $\bar{n}_C$ to the hydrophilic repeating units of PEG, $\bar{n}_E$ is defined as:

$$\frac{2I_e}{I_f} = \frac{\bar{n}_C}{\bar{n}_E} \tag{4.5}$$

The ratio is also helpful for estimating the kinetics and mechanism of the ROP, as well as for understanding the structure-property relationships of the synthesized triblock copolymers. It shows the repeating unit ratios of PCL to PEG before and after fractionation to explain the distribution of the PCL-rich byproducts and the purified PCL-PEG-PCL triblock copolymers according to the raw state (^{1}H-NMR) and theoretical calculations.

To predict the influence of the synthetic conditions, in Figure 4.6, it is plotted the theoretical values of $\left(\bar{n}_C/\bar{n}_E\right)_{theo}$ versus experimental results of $\left(\bar{n}_C/\bar{n}_E\right)_{NMR}$ obtained by ^{1}H-NMR.
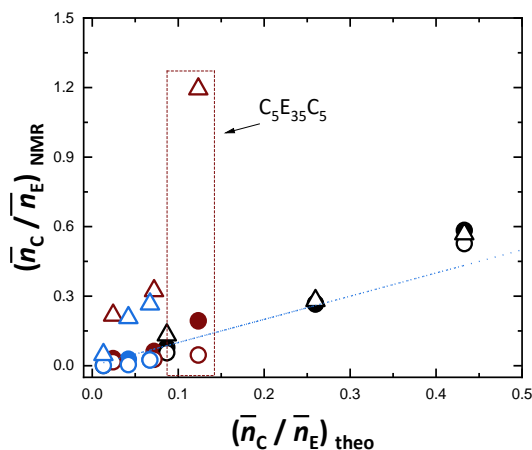
Figure 4.6. Comparison of repeating unit ratios of PCL to PEG before and after fractionation by ^{1}H-NMR. Triblock copolymers initiated by PEG$_{8K}$ (black), PEG$_{35K}$ (red), and PEG$_{100K}$ (blue). Theoretical ratios of repeating units (solid line). The raw product (filled circles). The purified fractions (open circles) and the soluble fractions (triangles).

In general, the variations between the soluble and the insoluble fractions indicate the presence of the side product. Importantly, the trend in the soluble fractions indicates that an increase in the polymerization of PCL-rich fraction is proportional to the theoretical degree of polymerization in each PEG-initiated series. This proportionality is additionally seen with the number-average molar mass of the macroinitiators. The difference between the two fractions is lower in triblock copolymers initiated by the PEG$_{8K}$ macroinitiator and higher in the triblock initiated by PEG$_{35K}$ and PEG$_{100K}$ macroinitiators. Owing to the ^{1}H-NMR evaluation, the most significant deviation between the soluble and insoluble fractions is obtained for $C_5E_{35}C_5$. PCL-rich byproduct is formed with the highest number of repeating units of ε-CL among the synthesized triblock copolymers. This proves the situation of these samples in SEC measurements that similarly show the most significant deviation in their molar mass.

The molar mass distribution analysis from SEC and ^{1}H-NMR explains the immortal polymerization of ε-CL in the presence of Bu$_2$SnO and a high molar mass linear PEG macroinitiator. We assume the chain transfer ability of the macroinitiators is significantly triggered by the transesterification catalyst of Bu$_2$SnO, as already explained by Inoue.[155] Hence, although nine series of triblock copolymers are synthesized at reasonable polydispersity, the raw polymer contains different constituents of PCL-rich byproduct and PCL-PEG-PCL at different degrees of polymerization. Bu$_2$SnO is prone to activate many more molecules, resulting in a PCL-rich byproduct at a high degree of polymerization.[156] Water residues in PCL used as macroinitiators might also have taken a role. As seen in $C_5E_{35}C_5$ results, the triblock copolymers synthesized at several sub-fractions present lower molar masses than the central molar mass of triblock copolymers.

4.1.2 Analysis of thermal properties

The crystallization of PEG occurs as extended chains below the molar mass of 4000 g mol^{-1} and as folded chains above the molar mass of 4000 g mol^{-1}.[157] Moreover, imperfect crystallization of PEG-PCL diblock copolymers is also found for a PEG molar mass of 5000 g mol^{-1}, depending on the relative block lengths.[158] It has also been reported that the melting behavior of PCL-PEG-PCL triblock copolymer for various block lengths, but only at low polymerization degree of PCL and below the molar mass of 8000 g mol^{-1} of PEG.[143,158–161] In this work, the thermal properties of the synthesized PCL-PEG-PCL triblock copolymers are evaluated with two parameters: the block length of PEG and the block length ratio of PCL to PEG obtained by ^{1}H-NMR. The related values are presented in Table 4.4.

Table 4.4. Melting temperatures enthalpies, crystallinity of the macroinitiators and triblock copolymers with the block lengths ratio from ^{1}H-NMR

Sample	$\left(\overline{n}_P / \overline{n}_E\right)_{NMR}$	T_m °C	ΔH_m j g^{-1}	X_c %
PEG$_{8K}$	-	62.5	178	99
PEG$_{35K}$	-	66	171	96
PEG$_{100K}$	-	63	138	77
C$_1$E$_8$C$_1$	0.056	58	108	59
C$_3$E$_8$C$_3$	0.266	n.d.	n.d.	n.d
C$_5$E$_8$C$_5$	0.527	53/57	74	55
C$_1$E$_{35}$C$_1$	0.017	61	137	71
C$_3$E$_{35}$C$_3$	0.028	58	133	70
C$_5$E$_{35}$C$_5$	0.046	62	121	66
C$_1$E$_{100}$C$_1$	0.001	63	93	47
C$_3$E$_{100}$C$_3$	0.005	61.5	85	43
C$_5$E$_{100}$C$_5$	0.025	61	127	65

The heating thermograms of the macroinitiators and triblock copolymers are shown in Figure 4.7. The shortest macroinitiators of PEG$_{8K}$ display melting temperatures of 62.5 °C.[162,163] The moderate and long macroinitiators of PEG$_{35K}$ and PEG$_{100K}$ display melting temperatures of 66 °C and 63 °C, respectively. However, the melting enthalpy of PEG macroinitiators decreases from 178 j g^{-1} to 131 j g^{-1} with a considerable increase in the molar mass from 8000 g mol^{-1} to 100000 g mol^{-1}.

The purified PCL-PEG-PCL triblock copolymers are seen as semicrystalline polymers. In general, the melting temperatures are very narrow between 58 °C and 63 °C with a unimodal thermogram except for C$_5$E$_8$C$_5$. Only C$_5$E$_8$C$_5$ displays multiple melting temperatures due to the high block length of PCL. On

the other hand, triblock copolymers initiated by longer macroinitiators display melting temperatures above 60 °C except for $C_3E_{35}C_3$. When the block length of PEG is noticeably high, the melting temperature of the triblock copolymers approaches the value of their macroinitiators.[164] A similar relation is considered for melting enthalpy in the PCL-PEG-PCL triblock copolymers. It is pointed out that the melting enthalpies of the synthesized triblock copolymers initiated by the same macroinitiators decrease with an increase in PCL ratios.
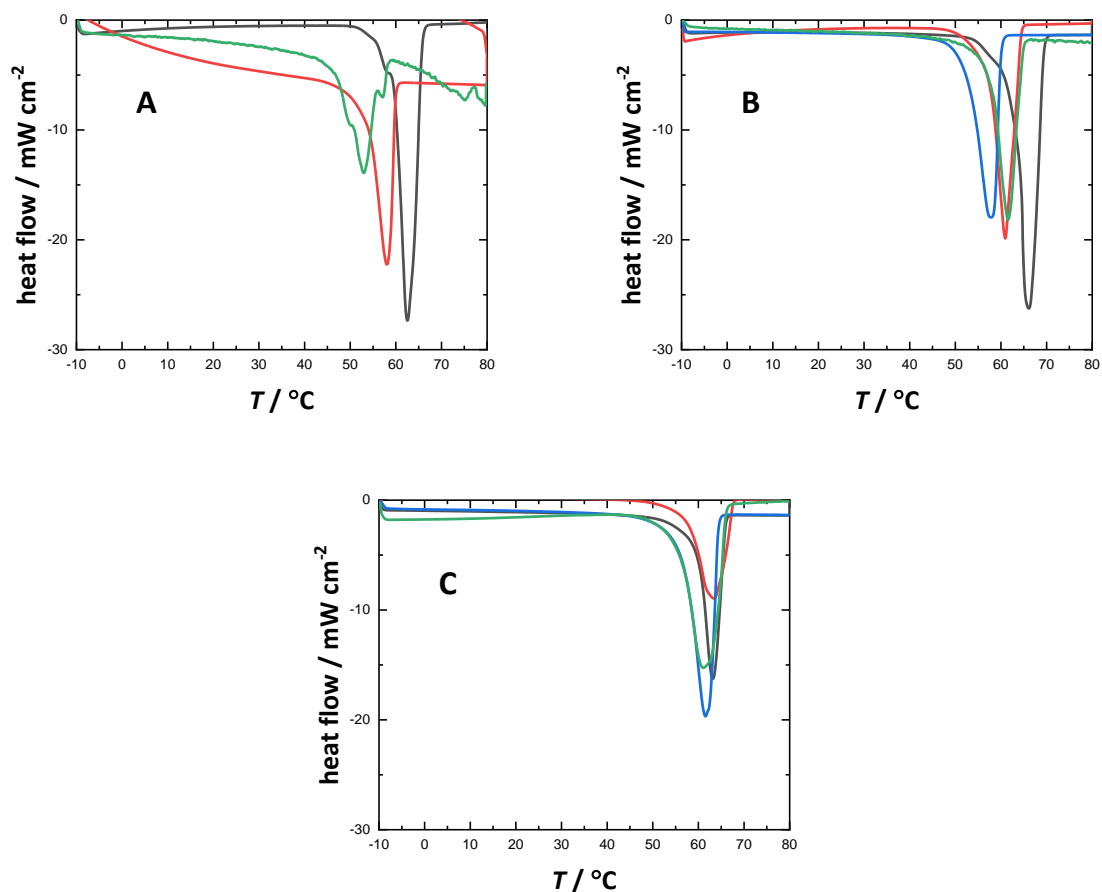
Figure 4.7. Melting thermograms of purified triblock copolymers and macroinitiators. A) PEG_{8K} (black), $C_1E_8C_1$(red), $C_5E_8C_5$ (green) B) PEG_{35K} (black), $C_1E_{35}C_1$(red), $C_3E_8C_3$ (blue), $C_5E_{35}C_5$ (green) C) PEG_{100K} (black), $C_1E_{100}C_1$(red), $C_3E_{100}C_3$ (blue), $C_5E_{100}C_5$ (green).

To investigate the effect of end-group functionalization on the PEG backbones, the crystallinity of the triblock copolymers X_C is calculated by:[165]

$$\% \, X_C = \frac{\Delta H_m}{(1-\mu_{PCL_{NMR}}) \times 197 \, \text{j g}^{-1}} \tag{4.6}$$

$\mu_{PCL_{NMR}}$ is the mass fraction of PCL calculated from ^{1}H-NMR, and 197 j g^{-1} is the value of melting enthalpy for 100 % crystallized PEG.[166]

The crystallinity of PEG above 8000 g mol^{-1} decreases as the molar mass increases. A drastic decrease in crystallinity for PEG is seen when it has a molar mass of 100000 g mol^{-1}. For the amphiphilic triblock copolymer, the crystallinity of PEG at all molar mass decreases with PCL end-groups. When the block length ratio of the PCL blocks at the same molar mass of PEG increases, the crystallinity of the copolymers tends to decrease. In addition, PCL is relatively high in the series triblock of PEG$_{8K}$ a drastic decrease occurs in crystallinity compared to non-functional PEG$_{8K}$. Similarly, when the PEG is relatively too long as seen in the series triblock of PEG$_{100K}$ the lowest crystallinity takes place. Interestingly, the crystallinity drastically increases with a higher PCL ratio $C_5E_{100}C_5$ than $C_1E_{100}C_1$ and $C_3E_{100}C_3$. Considering the triblock copolymers initiated by PEG$_{35K}$, the effect of PCL functionalization is less effective when PEG is relatively at moderate molar mass.

4.1.3 Characterization of aqueous solution behavior

To investigate the behavior of the synthesized PCL-PEG-PCL triblock copolymers in water, dilute solutions are prepared at 0.05 w/v %. Since the hydrophilicity of the triblock copolymer changes depending on each block length, their distributions in water show diversity. The diluted purified triblock copolymers in water display block hydrophobic PCL length-dependent behavior observed during sample preparation. The most hydrophobic triblock copolymers $C_3C_8C_3$ and $C_5E_8C_5$ are not dissolved even at dilute conditions. The triblock copolymer initiated by the macroinitiators over 8000 g mol^{-1} molar mass shows that the nature of hydrophilic PEG is more powerful at aqueous media behavior. Accordingly, the series of triblock consisting of PEG$_{35K}$ and PEG$_{100K}$ macroinitiators shows transparency in dilute solution. The presence of triblock copolymer dispersion at different sizes affects the solution behavior. Significantly, the presence of a more hydrophobic byproduct determines the optical properties of the prepared solution. As seen in Figure 4.8, he solution appearance changes from translucent to transparent in the case of PCL-rich byproduct separation by both fractionation and filtration.

The $C_5E_{35}C_5$ diluted solutions used for DLS measurements become transparent like purified polymers when a syringe filter is used at 0.45 μm pore size. This demonstrates that the polar syringe filter filtrates the hydrophobic PCL-rich oligomers. Considering the two essential factors, we only filter the water during sample preparation. The actual length of amphiphilic triblock copolymers can be affected by the pore size of filters in aqueous medium. It is also impossible to use the same size of syringe filter since the filtration might be a problem for higher molar mass and more hydrophobic triblock copolymers.
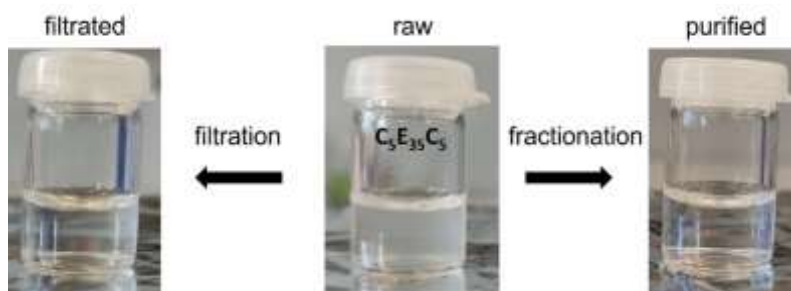
Figure 4.8. The dilute solutions of raw, filtered, and purified $C_5E_{35}C_5$, $c = 0.05$ w/v %.

Figure 4.9 shows the number distribution of $C_5E_{35}C_5$ and $C_5E_{100}C_5$ diluted solutions before and after purification. In comparison, DLS analysis shows unstable results that indicate inhomogeneities for unpurified samples; stable DLS histograms can be obtained for purified samples. DLS investigates the hydrodynamic size D_h of the purified triblock copolymers and some comparison with their raw product in aqueous media.
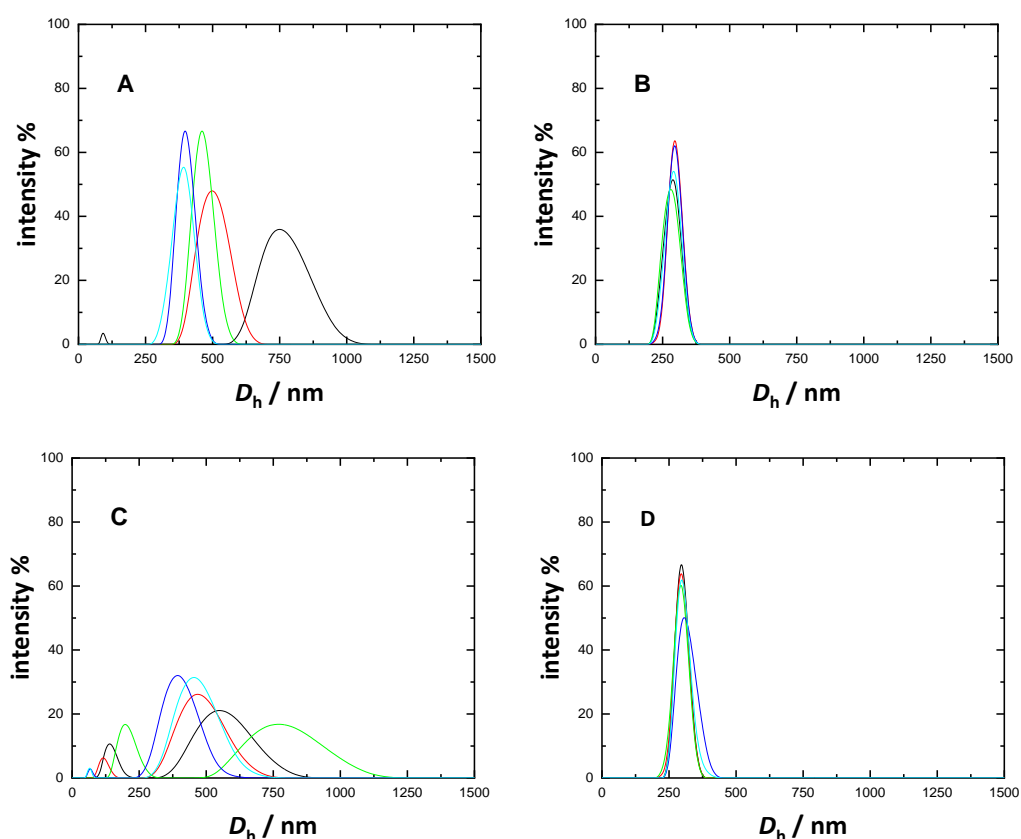
Figure 4.9. The intensity distribution of the aqueous raw (A) and purified (B) $C_5E_{35}C_5$, and the raw (C) and purified (D) $C_5E_{100}C_5$ at 0.05 w/v %. The curves show five independent measurements.

Table 4.5 exhibits data sets obtained by DLS. DLS results based on number distribution represent structure-property relationships of the PCL-PEG-PCL triblock copolymers. The hydrodynamic diameter of the dispersed polymers is found in the range of 250 nm – 450 nm, almost homogenously regarding the number of repeating unit ratios. As expected, $C_1E_8C_1$, with the shortest PEG and the highest PCL

ratio, shows the smallest hydrodynamic diameter in water. In the series of PEG$_{35K}$- and PEG$_{100K}$- initiated triblock copolymers, the hydrodynamic diameter decreases with increasing PCL block length ratio to PEG block lengths. In this case, the association between hydrophobic PCL end groups increases with the number of repeating units, making the triblock copolymer sizes smaller in water. Surprisingly, PEG$_{100K}$-initiated triblock copolymers demonstrate shorter hydrodynamic sizes than PEG$_{35K}$ initiated triblock copolymers. It is supposed that the heavier hydrophilic PEG blocks might be surrounded faster by water molecules.

Table 4.5. The hydrodynamic diameter of the purified triblock polymers in water, measured from DLS. The comparison of triblock copolymers is according to the block lengths ratios obtained ^{1}H-NMR.

Triblock copolymers	$\left(\overline{n}_P / \overline{n}_E\right)_{NMR}$	D_h nm	Main Peak Area %
C$_1$E$_8$C$_1$	0.056	274 ± 23.4	92.8
C$_1$E$_{35}$C$_1$	0.017	467 ± 44.4	92.3
C$_1$E$_{100}$C$_1$	0.001	249 ± 9.04	100
C$_3$E$_{35}$C$_3$	0.028	352 ± 5.38	99.6
C$_3$E$_{100}$C$_3$	0.005	342 ± 1.30	100
C$_5$E$_{35}$C$_5$	0.046	286 ± 6.53	100
C$_5$E$_{100}$C$_5$	0.025	298 ± 8.91	100

4.1.4 Conclusion

Due to the nature of ROP, PCL-PEG-PCL triblock copolymers are synthesized, showing broad molar mass distribution depending on the synthetic conditions. PCL-rich side products are characterized by SEC and ^{1}H-NMR. By fractionating the raw polymers in toluene, the polydispersity of the block copolymers can be enhanced, and the deconvolution of SEC curves demonstrates the extraction of the low molar mass byproducts. The characterization of thermal behaviors also indicates a successful purification since their thermograms are unimodal. The crystallinity of the triblock copolymers drastically changes when the molar mass PEG is relatively low and high with PCL functionalization. The aqueous behaviors of the triblock copolymers show controllable hydrodynamic diameter depending on the block length ratio of PCL to PEG.

4.2 Investigation of poly(ethylene glycol)-based precursors for 3D printing

3D printing as a manufacturing strategy experiences increased attraction in many applications, including tissue engineering. A potential bioink comprises a hydrogel precursor providing a biocompatible, 3D tissue-like microenvironment for potentially living cells. A printable bio-ink should fulfill optimized rheological requirements before and after printing for successful tissue reconstruction.

The employment of bimodal functional polymer solutions as precursors based on poly(ethylene glycol)s and their photoset into semi-IPNs is our strategy to independently tailor the flow viscosity of the ink, as well as the mechanic properties, including modulus, toughness, and viscoelasticity, and swelling behavior of the resulting hydrogels. Thereby, photopolymerization bridges the bioink solution and the 3D-printed hydrogel object. Using photopolymerized hydrogels instead of physical gels also allows the material properties to be more easily tuned. PEGDMA chains can be photopolymerized to form hydrogels in a controlled way. While the mechanical properties of the gels can be tailored by variation of the concentration of a functional PEG, a high molar mass polymer provides the viscosity and homogenous flow of the bioink. Thus, semi-IPN can overcome the difficulties of conventional hydrogel precursor solutions and investigate the context of appropriate polymer concentration and crosslink density.[46]

In this chapter, PEG-based binary solutions are investigated for their suitability as an ink. The flow and the viscoelastic behavior are investigated according to the rheological requirements. The binary polymer solutions are photo-crosslinked, and swelling measurements and mechanical properties of the hydrogels are characterized by varying the polymer concentration. The formulated polymer solutions are tested based on the manufacturing parameters in extrusion-based 3D printing.

4.2.1 Synthesis of poly(ethylene glycol) dimethacrylate

PEGDMA is a water-soluble and cross-linkable polymer composed of ethylene glycol repeating units and methacrylate functional groups at both ends. The presence of methacrylate groups allows PEGDMA to be photopolymerizable, forming crosslinked polymer networks. For this purpose, $PEG_{8K}DMA$ (8000 g mol^{-1}) is synthesized as described in the literature.[167]

Scheme 4.2. Synthesis of $PEG_{8K}DMA$
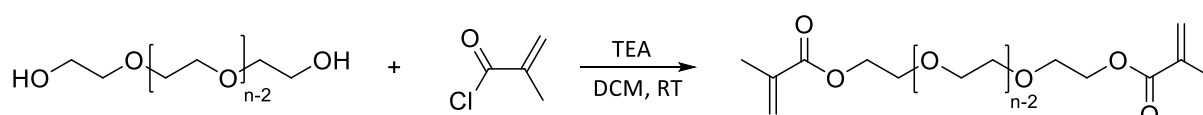
As a result of the functionalization of PEG diols with methacrylate terminated end groups, PEG$_{8K}$DMA is synthesized at a high functional degree, $f > 90$ %. ^{1}HNMR spectrum of the synthesized PEG$_{8K}$DMA is displayed in Figure 4.10.
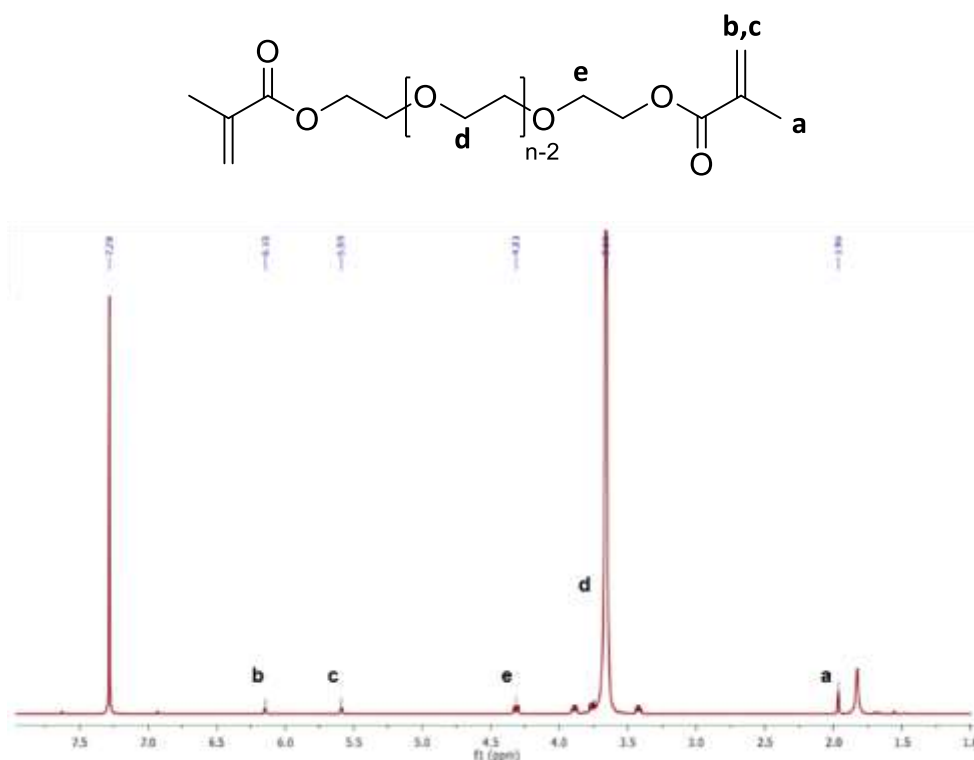
Figure 4.10. Proton groups of PEG$_{8K}$DMA and ^{1}H-NMR spectrum.

The methylene protons of the ethylene glycol repeating units appear at 3.66 ppm, with the junction proton of ethylene glycol at 4.31 ppm. The protons of the vinyl group signal are seen at 5.59 ppm and 6.15 ppm, indicating the occurrence of methacrylation by the proton of methyl substitute at 1.96 ppm.

4.2.2 Flow behavior and linear viscoelasticity of binary solutions

Rheological properties are one of the main requirements to print an ideal ink. Oscillatory time-sweep is also essential when testing a polymer that may undergo macro- or micro-structural rearrangement with time. These rearrangements directly influence rheological behavior. PEG$_{8K}$DMA is a hydrophilic polymer with a methacrylate end group, and aqueous PEG$_{8K}$DMA solution at the mass fraction of 20 m% is analyzed by time-sweep measurement.

Figure 4.11 illustrates a typical example of shear-induced gelation. Under a small strain, the elastic modulus G' linearly increases, a crossover point appeared, $G' = G''$. The crossover time shifts from 9 s to 450 s when the degree of functionality decreases from 90 % to 75 %.
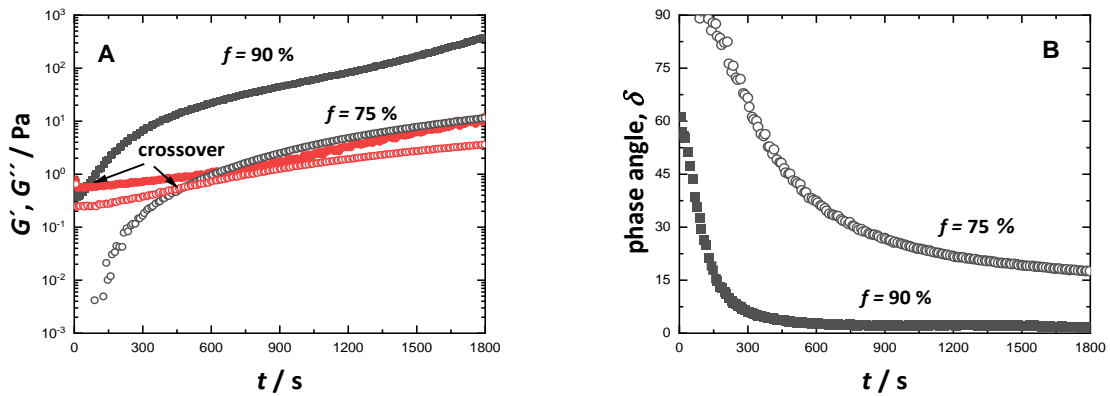
Figure 4.11. A) Time-sweep measurements of $PEG_{8K}DMA$ solution at two degree of functionality B) The phase angle $f = 90\%$ (filled), $f = 75\%$ (open). G' (black), G'' (red). $\gamma_0 = 0.5\%$ and $\mu_{DMA} = 20$ m%

In parallel to moduli behavior, the phase angle curve of $f = 90\%$ reaches plateau at $\delta = 0$ that explains the solid-like behavior of $PEG_{8K}DMA$ chains in water. On the other hand, when the functionality decreases to 75%, the phase angle reaches a plateau at 18 °C. A rapid association at high functional $PEG_{8K}DMA$ chains express the end-group associations. After approaching approximately onset value around 400 s, G' increases with time for $f = 90\%$ indicating sticky chains in water. In contrast, G' displays almost reaching a plateau value for $f = 75\%$, stating the relaxation of the polymer chains.

In addition to time-dependent behavior, understanding the flow behaviors helps to deal with the challenges of the printing process. A poor ink, like low viscous, can reduce the extrusion quality and affect the mechanical properties of the deposited solution in during extrusion proces. These drawbacks are related to the rheology of fluids. As explained in section 2.1.3, concentration and molar mass mainly control the viscosity of a polymer.

A binary system is considered to develop an ink in which $PEG_{8K}DMA$ and PEG_{100K} ($PEG_{8K}DMA/PEG_{100K}$) are formulated by adjusting the mass fraction of the individual components. High molar mass linear PEG_{100K} is a viscosity enhancer for the functional $PEG_{8K}DMA$ solutions.

The composition of the solutions is presented in Table 4.6. The formulations can be categorized into two groups. The first group consists of homopolymer solutions adjusted by $PEG_{8K}DMA$ mass fraction, μ_{DMA}. The second group of solutions consists of two polymers, forming binary solutions named $PEG_{8K}DMA/PEG_{100K}$. Within this group, BS_{10} denotes binary solutions with $PEG_{8K}DMA$ mass fraction of 10 m% while BS_{20} denotes those with a $PEG_{8K}DMA$ mass fraction of 20 m% at various PEG_{100K} mass fractions, μ_{100K}.

Table 4.6. The composition of polymer solutions (inks).

Solution (ink)	$\mu_{\text{PEG}_{8K}\text{DMA}} / \mu_{\text{PEG}_{100K}}$	μ_{DMA} m%	μ_{100K} m%
PEG$_{8K}$DMA	5/0	5	0
	10/0	10	0
	20/0	20	0
BS$_{10}$	10/1	10	1
	10/3.5	10	3.5
	10/5	10	5
BS$_{20}$	20/1	20	1
	20/3.5	20	3.5
	20/5	20	5
	20/10	20	10
	20/20	20	20

The rheology of the formulated solutions is evaluated by the following two methods: steady-state and dynamic measurements. First, the steady-state is performed for PEG$_{100K}$ solutions to determine the concentration regimes, as mentioned in section 2.1.3.
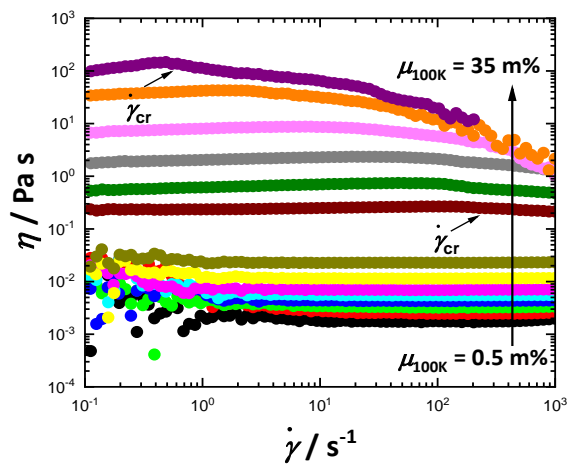
Figure 4.12. A) The flow curves of PEG$_{100K}$ solutions at various mass fractions. 0/0.5 (black), 0/1 (red), 0/1.5 (green), 0/2 (blue), 0/2.5 (cyan), 0/3 (pink), 0/4 (yellow), 0/5 (dark yellow), 0/10 (wine), 0/15 (olive), 0/20 (grey), 0/25 (pink), 0/30 (orange), 0/35 (purple).

Figure 4.12 displays viscosity curves of PEG$_{100K}$ solutions in a wide range mass fraction. The viscosity curves are Newtonian below the mass fraction of 5 m%. The viscosity of the solutions decreases at the high shear rate, and the critical sear rate $\dot{\gamma}_{\text{cr}}$ is found in the range of 0.4 s^{-1} – 110 s^{-1} when μ_{100K} increases from 10 m% to 35 m%. A shear deformation of PEG$_{100K}$ solutions is put in evidence, and they appear to be weak polymer networks contrary to lower mass fractions.

These solutions show extreme shear-rate dependency above the mass fraction of 25 m%; thus, shear degradation is considered.
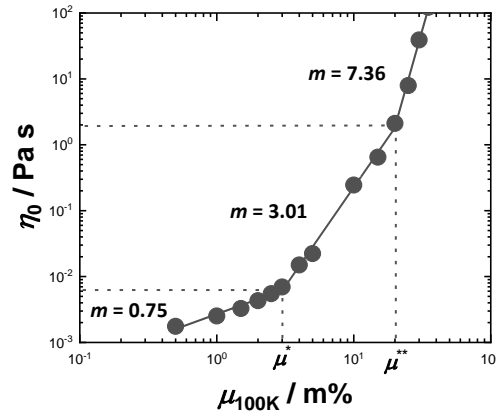
Figure 4.13. Zero-shear viscosity of PEG$_{100K}$ solution as the function of the mass fraction, and the concentration regimes of PEG$_{100K}$ solutions.

Figure 4.13 shows the zero-shear viscosity depending on the mass fraction of PEG$_{100K}$. The three distinct regimes with different slopes indicate the dilute, semi-dilute, and concentrated regimes of PEG$_{100K}$ solutions. The transition points between two regimes determine the critical mass fractions of PEG$_{100K}$ that is calculated $\mu^* = 3$ m%, representing the dilute ($m = 0.75$) and semi-dilute regimes, ($m = 3.01$). The other is seen at $\mu^{**} \approx 20$ m%, that defines the concentrated regime ($m = 7.36$). Hence, entanglement mass fractions of PEG$_{100K}$ are determined to lead to a drastic increase in viscosity.[168]
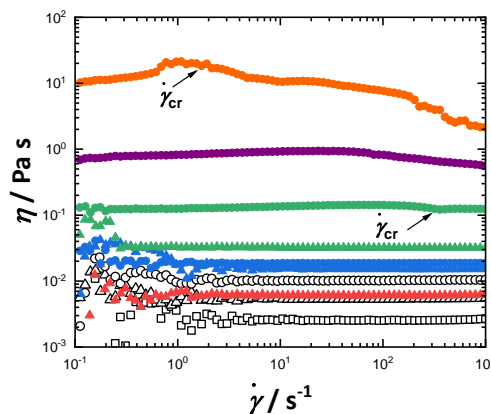
Figure 4.14. The flow curves of PEG$_{8K}$DMA and binary solutions at various mass fractions. 5/0 (open square), 10/0 (open triangle), and 20/0 (open circle), 10/1 (black triangle), 10/3.5 (blue triangle), 10/5 (green triangle), 20/3.5 (blue circle), 20/5 (green circle), 20/10 (purple) and 20/20 (orange).

Similarly, the flow behavior of PEG$_{8K}$DMA and binary solutions of PEG$_{8K}$DMA/PEG$_{100K}$ are investigated by varying mass fractions. The obtained flow curves in Figure 4.14 demonstrate Newtonian flow behavior PEG$_{8K}$DMA solutions, although μ_{DMA} increases from 5 m% to 10 m%. Similarly, the series of

BS$_{10}$ is also Newtonian since no power-law region is observed. On the contrary, the effect of linear PEG$_{100K}$ is seen on the solutions of BS$_{20}$ above the entanglement mass fraction of PEG$_{100K}$; shear-thinning is observed in the range of $1 \, s^{-1} - 140 \, s^{-1}$, thus PEG$_{8K}$DMA can be used as non-Newtonian.
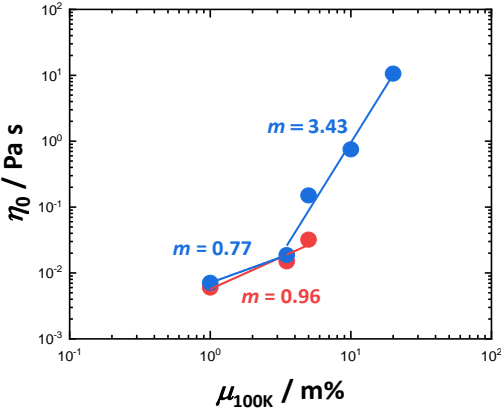
Figure 4.15. Zero-shear viscosity of BS$_{10}$ (red) and BS$_{20}$ (blue) versus the mass fraction of PEG$_{100K}$.

As seen in Figure 4.15, from the zero-shear viscosity of the binary solutions, BS$_{10}$ is dominated by PEG$_{100K}$ since there is no significant increase in η_0 with increasing in μ_{100K}. On the contrary, the viscosity in BS$_{20}$ significantly increases with μ^*. η_0 of the BS$_{20}$ is between 0.02 Pa s and 11 Pa s. In the case of $\mu_{100K} > \mu^*$ in BS$_{20}$, a complex flow behavior is assumed due to the high associations in the concentrated binary solutions. The entangled polymer chains in water refers to the viscous and elastic behavior of the binary solutions. Dynamic measurements can describe viscoelastic fluid behavior by complex viscosity, another flow parameter in rheology that measures the viscosity under deformation.
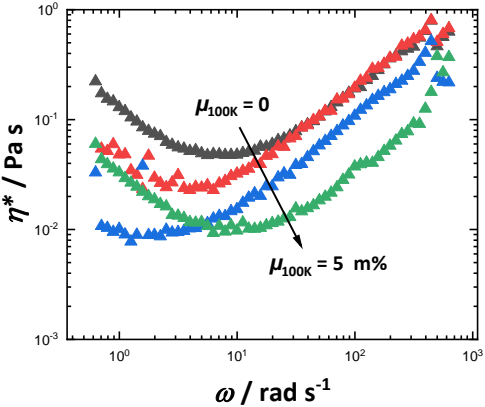
Figure 4.16. The complex viscosity curves of 10/0 (black) and BS$_{10}$, 10/1 (red), 10/3.5 (blue), 10/5 (green).

Figure 4.16 introduces complex viscosity curves η^* curves of BS$_{10}$. It is visible that the curves consist of three distinctive regimes: a reduction, a plateau, and an increment.[169] The reduction is seen in the low-frequency range. In this regime, an entanglement occurs between aqueous PEG$_{8K}$DMA and PEG$_{100K}$

chains. A short plateau regime follows it; however, the range of plateau increases when μ_{100K} increases to 5 m%, in which solid interactions dominate the binary solutions. On the other hand, the upturn behavior in the curves in the last regime indicates the resists of an entangled network against deformation. η^* of BS$_{10}$ increases with an increase μ_{100K} at lower shear rates but not at higher shear rates.
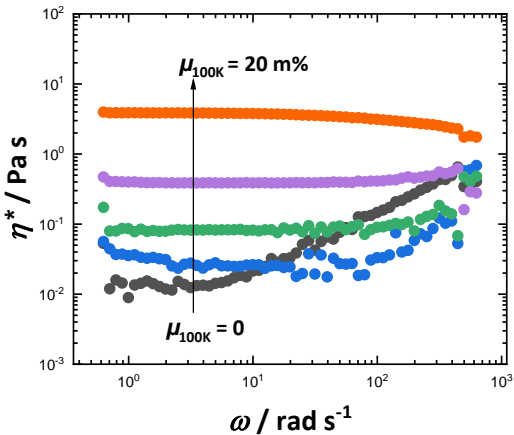
Figure 4.17. The complex viscosity curves of 20/0 (black) and BS$_{20}$, 20/3.5 (blue), 20/5 (green), 20/10 (purple), and 20/20 (orange).

In contrast, Figure 4.17 shows significantly longer plateaus at all μ_{100K}. The stable viscous behavior is owing to concentrated polymer chains, still 20/0 is highly dynamic in this range of frequency. A gel-like network is expected in higher frequency range for BS$_{20}$.

The phase angle curves of the solutions explain the expected solution behaviors BS$_{10}$ is poorly entangled and easily deformable since there is no plateau (Figure 4.18).
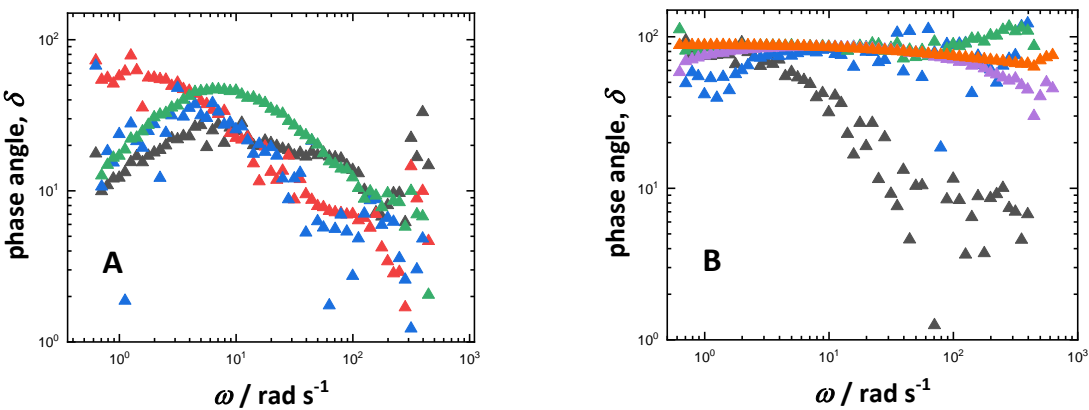
Figure 4.18. Phase angle of A) BS$_{10}$: 10/1 (red), 10/3.5 (blue), 10/5 (green), and B) BS$_{20}$: 20/3.5 (blue), 20/5 (green), 20/10 (purple), and 20/20 (orange).

It is assumed that the linear polymer of PEG$_{100K}$ primary dominates with the polymer associations, as seen in the phase angle curve of 10/3.5. With the entanglement mass fraction, a solid -like behavior is considered above the angular frequency of 10 rad s^{-1}. In contrast, BS$_{20}$ seems highly concentrated, two water soluble polymers are associated, $\delta > 45$, it is considered a deformable and binary linear polymer solutions.

In addition to rotational rheometry, the flow behavior of the binary solutions is investigated by capillary extrusion rheometry with a home-developed plunger-based syringe-needle system. The essential features of capillary rheometers are explained in section 2.1.2. Capillary extrusion is performed for 15 s, and a uniaxial force is applied to a syringe at a constant velocity at room temperature. The capillary set-up consists of the needle length of L_N = 44 ± 0.2 mm, the needle inner radius R_N = 0.475 mm, and the inner radius of R_S = 7.950 mm in 10 mL syringe. A uniaxial force is applied to a syringe at a constant extrusion rate ν, 8.3 x 10^{-4} m s^{-1}, 16.7 x 10^{-4} m s^{-1}, 33.3 x 10^{-4} m s^{-1}, 66.7 x 10^{-4} m s^{-1}, and 100 x 10^{-4} m s^{-1}. The experiments are performed at room temperature. The experimental data sets are interpreted according to the mass fractions of components and the extrusion rate.
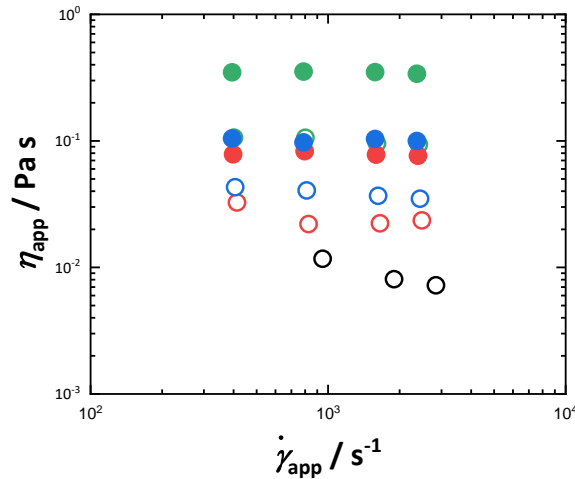
Figure 4.19. True-wall viscosity of BS$_{20}$ and PEG$_{100K}$ solutions. 20/3.5 (filled red), 20/5 (filled blue), 20/10 (filled green), 0/3.5 (open red), 0/5 (open blue), and 0/10 (open green).

Figure 4.19 shows true-wall viscosity η_w data sets of PEG$_{100K}$ and BS$_{20}$ calculated according to the Rabinowitsch correction (section 2.1.2). A slight shear-thinning is seen in PEG$_{100K}$ solutions of 0/3.5 and 0/5 in the capillary system. In contrast, no power-law region is observed for 0/10. Similarly, BS$_{20}$ is not shear-dependent. Considering the solutions at constant μ_{100K}, η_w is greatly enhanced in the binary system. For instance, η_w are 0.10 Pa s for 0/10 and 0.34 Pa s for 20/10. Consequently, it is considered that the applied viscous force increases with polymer concentration.

As a summary of the rheology of the solutions, viscous properties are significantly affected by the dynamics of entangled networks of long and short chain lengths of PEG_{100K} and $PEG_{8K}DMA$, respectively. Considering the non-ideality of polymers in water, separated polymer chains provide network-like behavior.

4.2.3 Phase behavior in binary solutions

DSC measurements investigate the phase behavior of aqueous PEG_{100K} solutions and BS_{20}. The influence of the mass fraction between 1 m% and 10 m% in dilute and semi-dilute aqueous polymer solutions for PEG_{100K}, and BS_{20} are investigated by DSC thermograms. The melting temperatures of the water-rich $T_{m,w}$ and the polymer-rich phase $T_{m,p}$ change with polymer concentration. Figure 4.20 shows the heating thermograms for aqueous PEG_{100K} and BS_{20}. These thermograms exhibit two distinct melting peaks, which signify the existence of phase separations in a miscible polymer solution.
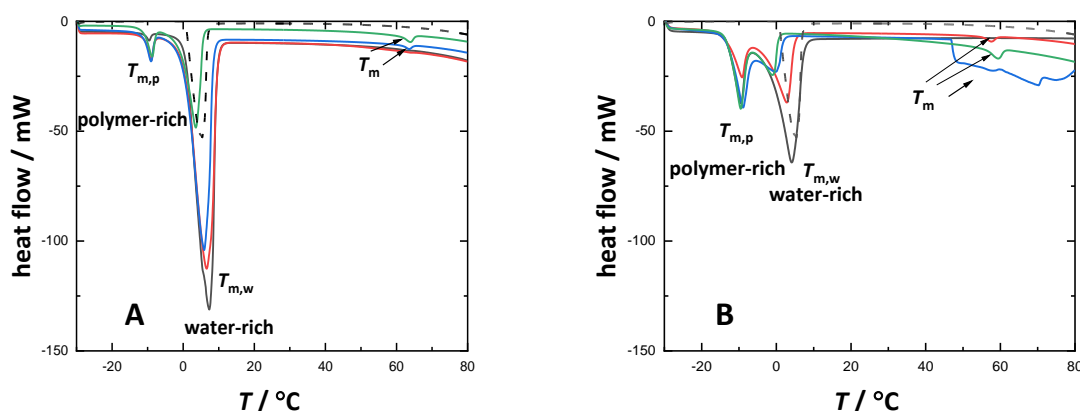
Figure 4.20. A) DSC thermograms of water (dashed) and PEG_{100K} solutions. 0/1 (black), 0/3.5 (red), 0/0.5 (green), and 0/10 (blue). B) DSC thermograms of BS_{20} solutions. 20/0 (dashed) 20/1 (black), 20/3.5 (red) and, 20/5 (green).

According to the values in Table 4.7 obtained from DSC measurements, $T_{m,w}$ slightly decreases with an increase in μ_{100K} in PEG_{100K} solutions, and $T_{m,p}$ is almost constant. Then, T_m appears around 60 °C when μ_{100K} is 5 m% and 10 m%. Figure 4.20B reveals thermograms of the binary solutions. In comparison, there is no significant difference in $T_{m,p}$, but $T_{m,w}$ is lower in BS_{20} than in PEG_{100K}. A similar trend is also seen in melting enthalpies of both phases, $\Delta H_{m,p}$ and $\Delta H_{m,p}$. Multiple T_m appears above 40 °C in BS_{20} with the entanglement mass fractions PEG_{100K} representing a transient network in the binary system.[170]

Considering the binary viscosity, as the total polymer concentration increases, the nucleation of water molecules proceeds slower because of the strong associations between polymers and polymer-water molecules. All these findings demonstrates the formation of weak gel networks in semi-dilute and concentrated binary solutions, where polymer chains are no longer isolated from each other.[171–173]

Table 4.7. The melting temperatures and the melting enthalpies of PEG-based solutions.

	Water	PEG$_{100K}$				BS$_{20}$			
μ_{100K}	ΔH_{water}	$T_{m,p}$	$T_{m,w}$	$\Delta H_{m,p}$	$\Delta H_{m,w}$	$T_{m,p}$	$T_{m,w}$	$\Delta H_{m,p}$	$\Delta H_{m,w}$
m%	j g^{-1}	K	K	j g^{-1}	j g^{-1}	K	K	j g^{-1}	j g^{-1}
0	278.48	-	-	-	-	263.82	268.9	263.82	268.9
1	-	263.65	280.4	263.65	280.4	264.07	270.32	264.07	270.32
3.5	-	264.24	279.82	264.24	279.82	264.23	273.15	264.23	273.15
5	-	264.15	279.15	264.15	279.15	263.73	272.15	263.73	272.15
10	-	264.48	276.73	264.48	276.73	-	-	-	-

4.2.4 Synthesis and characterization of photo-crosslinked hydrogels

The formulated binary solutions are hydrogel precursors in photopolymerization (Figure 4.21). Their photo-crosslinking is initiated by Type-I and Type-II photoinitiators of LAP and Ru, respectively. The network properties of photopolymerized hydrogels are characterized by swelling measurement and rheology.
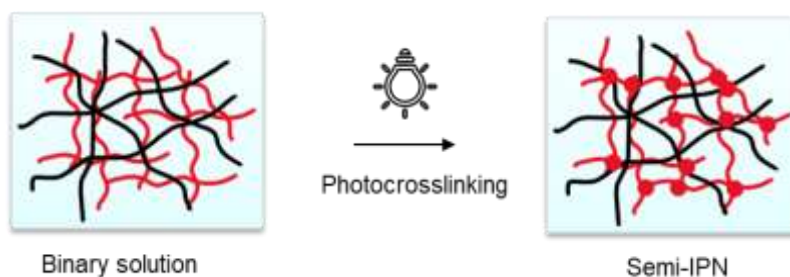
Figure 4.21. Illustration of photopolymerization from polymer precursor solutions to semi-IPN hydrogels.

4.2.4.1 LAP-initiated photopolymerization

LAP is a water-soluble and biocompatible photoinitiator commonly used for methacrylated polymers to obtain their hydrogels via photopolymerization (section 2.3.1).

Scheme 4.3. The cleavage of LAP
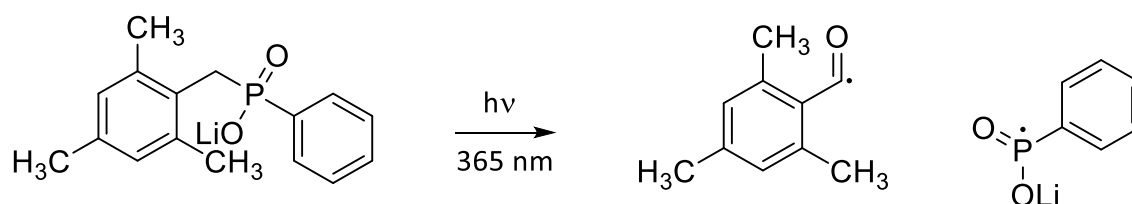
Photo-initiated radical polymerization is performed by irradiation at 365 nm, and LAP absorbs light and then composes into two radicals that trigger photo-polymerization.[114] Figure 4.22 presents the

spectrum of LAP, where the absorbance maximum is 369 nm as a UV photoinitiator. The molar extinction coefficient is calculated $\varepsilon = 333$ mol L^{-1} cm^{-2} at 365 nm in the aqueous solution of c = 1.87 x 10^{-4} mol L^{-1}.
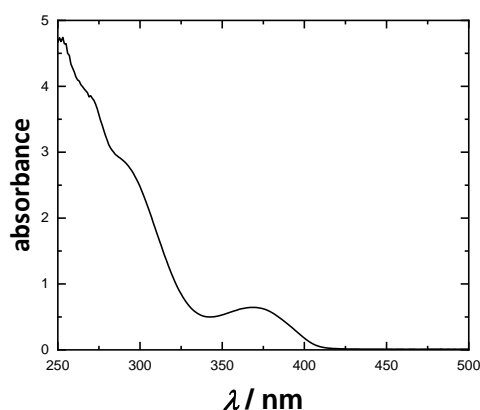
Figure 4.22. The absorption spectrum of LAP solution, c = 1.87 x 10^{-3} mol L^{-1}.

The investigated PEG-based binary solutions are used as precursors for photopolymerizable hydrogels. The composition of LAP-initiated hydrogels is presented in Table 4.8.

Table 4.8. The composition of LAP-initiated hydrogels

Network	Hydrogel	μ_{DMA} m%	μ_{100K} m%
SN$_5$	5/0	5	0
SN$_{7.5}$	7.5/0	7.5	0
SN$_{10}$	10/0	10	0
SN$_{20}$	20/0	20	0
semi-IPN$_5$	5/1	0	1
	5/3.5	0	3.5
	5/5	0	5
semi-IPN$_{10}$	10/1	10	1
	10/3.5	10	3.5
	10/5	10	5
	10/10	10	10
semi-IPN$_{20}$	20/1	20	1
	20/3.5	20	3.5
	20/5	20	5
	20/10	20	10

The precursors are prepared for two different polymer networks. The first is for the single network (SN) of PEG$_{8K}$DMA hydrogels, denoted as 5/0, 7.5/0, 10/0, and 20/0. The second category consists of semi-IPN hydrogels, PEG$_{8K}$DMA/PEG$_{100K}$ hydrogels, in which μ_{DMA} is held constant while varying μ_{100K}. Examples of these semi-IPN hydrogels include 20/0, 20/1, 20/3.5, 20/5, and 20/10, at the mass fraction of 20 m%.

A hand-held lamp irradiates the hydrogel precursors at the light intensity of $I_0 \approx 1.5 \text{ mW cm}^{-2}$ for 480 s in circle-shaped molds. The spectrum of the light source is presented in Figure 4.23.
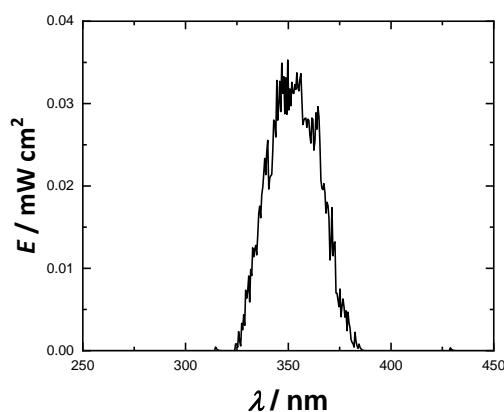
Figure 4.23. The emission spectrum of the hand-held lamp used for LAP-initiated photopolymerization.

The hydrogels are synthesized via photo-initiated radical polymerization in the presence of LAP. After photo-crosslinking, tough hydrogels are put into water to calculate the gel content G and the mass swelling ratio Q_{m} to reach the swelling equilibrium.
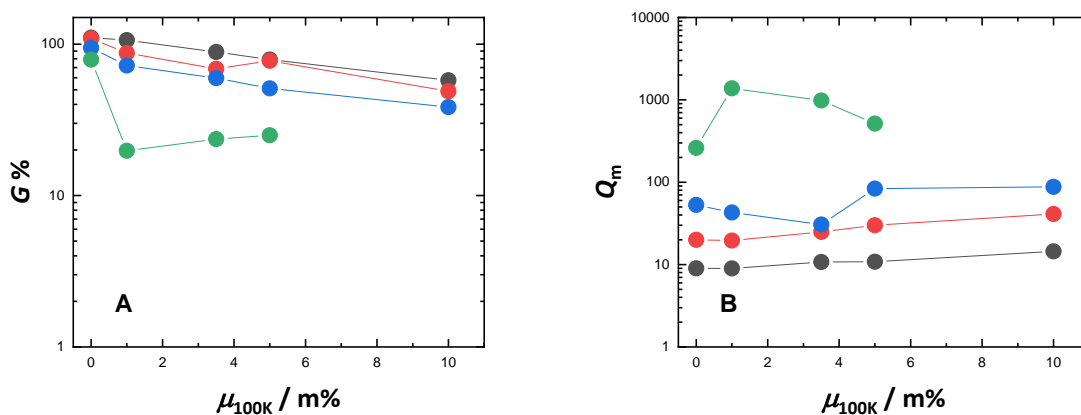
Figure 4.24 A) The gel content and B) the mass swelling ratio of LAP-initiated SN and semi-IPN hydrogels, semi-IPN$_5$ (green), semi-IPN$_{7.5}$ (blue), semi-IPN$_{10}$ (red), and semi-IPN$_{20}$ (black).

In Figure 4.24A, it is seen the relationship between G and μ_{100K}. The plots of SN hydrogel, ($\mu_{100K} = 0$) reveals nearly complete monomer conversion by UV. As μ_{100K} increases, G progressively decreases in the represented semi-IPN hydrogels. Figure 4.24B shows that it is observed for SN hydrogels ($\mu_{100K} = 0$) as μ_{DMA} increases from 5 m% to 20 m%, Q_m significantly decreases from 260 to 9. On the other hand, the semi-IPN$_{20}$ hydrogels do not swell much in water $Q_m \approx 10$ at all μ_{100K}. The semi-IPN$_{7.5}$ and semi-IPN$_{10}$ hydrogels show moderate swelling that μ_{100K} is more effective. When their semi-IPN hydrogels are produced at $\mu_{100K} > \mu^*$, Q_m. Interestingly, semi-IPN$_5$ hydrogels exhibit the most significant swelling among all hydrogels with $Q_m > 510$ due to the low photo-crosslinked PEG$_{8K}$DMA content.

Rheological properties of LAP-initiated hydrogels are investigated after synthesis and in the swollen state. It presents oscillation measurements of the LAP-initiated hydrogels after synthesis.
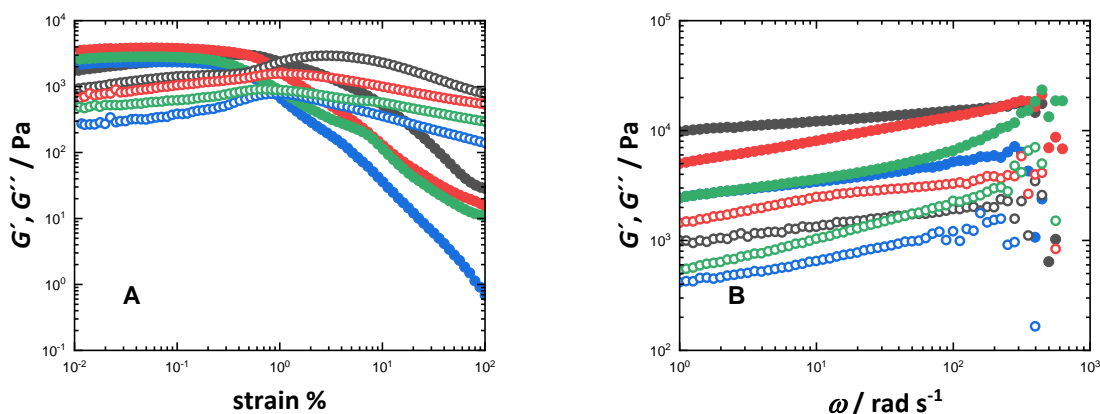
Figure 4.25. Oscillation measurements of LAP-initiated hydrogels after-synthesis. A) Strain-sweep at 6.283 rad s-1 and B) frequency-sweep at strain 0.1 %, G′ (filled) and G′′ (open). 20/0 (black), 20/1 (red), 20/3.5 (blue), and 20/5 (green).

Figure 4.25A shows all hydrogels show LVR according to the strain-sweep measurements that slightly decrease with μ_{100K} from 0.9 % to 0.7 % strain. Figure 4.25B, the frequency-sweeps of $G′$, with $G_0 \approx$ 11000 Pa is for SN$_{20}$ hydrogels. In contrast, the elastic moduli of semi-IPN$_{20}$ hydrogels decrease approximately from 7500 Pa to 3250 Pa, as μ_{100K} increases from 1 m% to 5 m%. It can be noted that $G′$ and $G′′$ highly close to each other after-synthesis state.

The rheological properties of the swollen-equilibrium LAP-initiated hydrogels are followed in Figure 4.26.
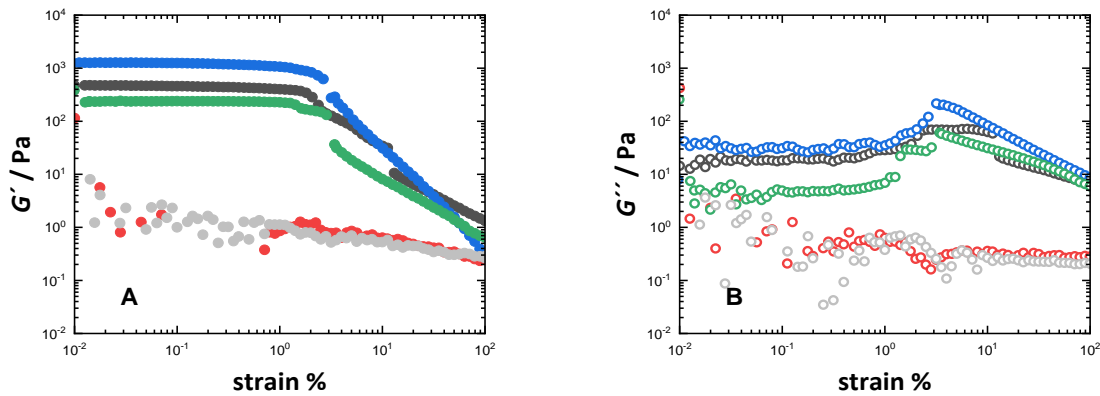
Figure 4.26. Strain-sweep measurements of LAP-initiated swollen equilibrium hydrogels at 6.283 rad s^{-1}, A) G' and B) G'', 20/0 (black), 20/0.5 (grey), 20/1 (red), 20/3.5 (blue), and 20/5 (green).

According to strain-sweep in Figure 4.26, 20/0, 20/3.5 and 20/5 display LVR of G', up to 1 % strain. However, the same behavior for semi-IPN$_{20}$ hydrogels of 20/0.5 and 20/1 cannot be observed. Since the hydrogels are prepared as a mixture of low and high molar-mass precursor chains, the possibility of an ideal bimodal polymer network is limited. Two polymer chains are chemically crosslinked and trapped in the semi-IPN, in which it is impossible to crosslink homogenously in local volumes of the semi-IPN hydrogels using water as a solvent. Here, in the case of $\mu < \mu^*$ the weaker crosslinked strands between the PEG$_{8K}$DMA network and PEG$_{100K}$, the disparities in the crosslinks of the semi-IPN fail the mechanical properties. On the other hand, in the case of $\mu > \mu^*$, the chains of the PEG$_{100K}$ are more trapped in the photo-crosslinked PEG$_{8K}$DMA network, making the semi-IPN hydrogels stiffer; thus, the polymer network responds to better elasticity during deformation.

The frequency-sweeps of the swollen equilibrium LAP-initiated hydrogels are displayed in Figure 4.27.
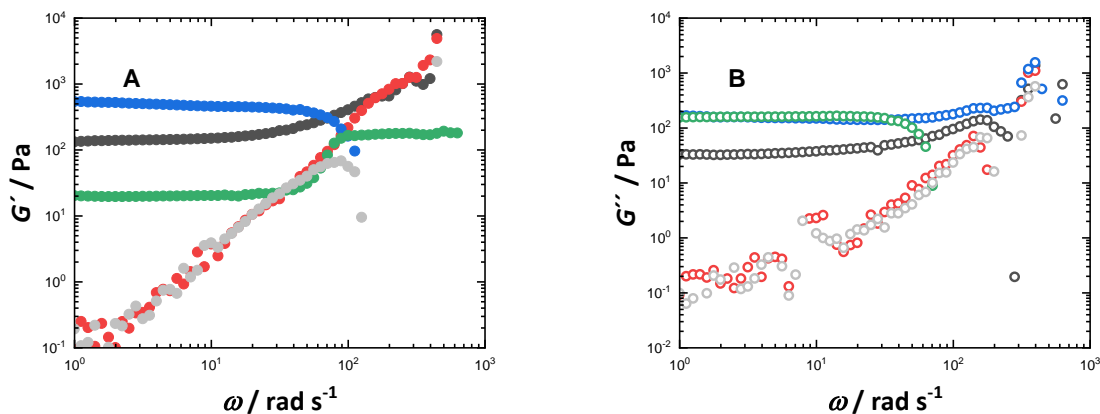
Figure 4.27. Frequency-sweep of LAP-initiated swollen equilibrium hydrogels at strain 1 %, A) G' and B) G'', 20/0 (black), 20/0.5 (grey), 20/1 (red), 20/3.5 (blue), and 20/5 (green).

According to elastic moduli, G_0 is calculated at 140 Pa for 20/0. For 20/3.5 and 20/5, it is 500 Pa and 20 Pa, respectively. 20/0.5 and 20/1 lack plateau regimes due to the considerations above. In addition, considering the gel content, when the mass fraction of PEG_{100K} is 5 m%, G'' is slighty higher than G' for swollen state. This indicates the dominance of linear and hydrophilic PEG_{100K} chains as a viscous component considering gel content calculations. Although longer PEG chains are not fully entangled into the chemically crosslinked $PEG_{8K}DMA$ networks at swollen equilibrium, the moduli curves 20/5 represent a viscoelastic soft material.

4.2.4.2 Ruthenium-initiated photopolymerization

As explained in section 2.3.1, Ru is a Type-II photoinitiator and a poor water-soluble compound. Since it requires a co-initiator to initiate a photopolymerization, PEG-based hydrogels use non-cytotoxic APS at various concentrations.[174] The photo-crosslinking is carried out by irradiation using a UV LED point light source with emission spectrum at 405 nm, as shown in Figure 4.28.
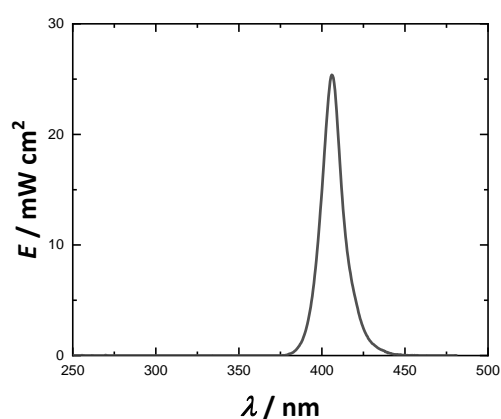
Figure 4.28. The emission spectrum of UV-led light source.

Several preliminary experiments by irradiating hydrogel precursors are performed to optimize the photopolymerization of Ru-initiated hydrogels. The effect of the initial mole of Ru (n_{Ru}), the mole ratio Of Ru to APS (n_{Ru}/n_{APS}), the light intensity (I_{405}), and the irradiation time (t_{irr}) on the gelation process and optical appearance are investigated as reported in Table 4.9.

Table 4.9. The preliminary composition of the precursor solutions for Ru-initiated photopolymerization

$PEG_{8K}DMA$ m%	n_{Ru} mmol	n_{Ru}/n_{APS}	I_{405} mW cm^{-2}	t_{irr} s	Observation
16	10	1/20	439	600	no gelation
16	2	1/50	439	300	viscous
14	4	1/50	439	240	gel, opaque
14	2	1/100	439	180	gel, nearly transparent

Accordingly, a gelation observed at 439 mW cm^{-2}, when (n_{Ru}) increases from 2 mmol to 4 mmol at constant ($^{n_{\mathrm{Ru}}}/_{n_{\mathrm{APS}}}$). However, the obtained gel is not transparent. A transparent hydrogel can be produced in a shorter time, if ($^{n_{\mathrm{Ru}}}/_{n_{\mathrm{APS}}}$) = 1/100. Although n_{Ru} increases to 10 mmol, there is no photo-crosslinking in 600 s. Consequently, it is considered the photopolymerization rate dependent on n_{APS} rather than n_{Ru}.

A diluted aqueous Ru solution of $c = 6.84 \times 10^{-4}$ mol L^{-1} and Ru/APS solution (1/200) are analyzed without irradiation by UV-Vis spectrometry.
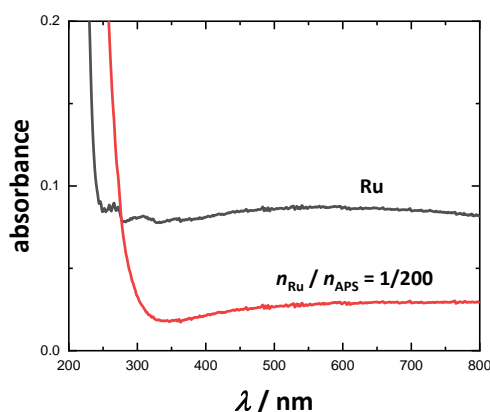
Figure 4.29. UV-Vis spectra of Ru solution (black), c = 6.84 x 10^{-4} mol L^{-1} and Ru/APS solution (red) at the mole ratio of 1/200.

Figure 4.29 shows their spectra, in which the absorbance is decreased, with APS showing a bathochromic effect and a minor absorbance maximum above 400 nm. It is considered that a hydrogen abstraction takes place according to the Type-II mechanism (see Figure 2.16).

As a result of the slow crosslinking mechanism, less concentrated polymer solutions are considered than LAP-initiated polymer solutions. PEG$_{100K}$ varies up to entanglement mass fraction, μ^*. Ru-initiated hydrogels are systemically followed according to the composition of the precursors listed in Table 4.10. The mole ratio of the (co)initiators varies by adjusting the amount of Ru while keeping the amount of APS constant. Additionally, the mass fraction of PEG$_{100K}$ is varied. Similarly explained in the previous section, SN and semi-IPN denote single network and semi-IPN hydrogels, respectively. All Ru-initiated hydrogels are only produced at PEG$_{8K}$DMA mass fraction of 14 m%. Thus, the numeric values correspond to μ_{100K} in semi-IPN. In addition, the index indicates the mole ratio of Ru to APS. For instance, semi-0.7$_{1/10}$ symbolizes the semi-IPN hydrogel with the mole ratio of Ru to APS, 1/100, in which PEG$_{8K}$DMA and PEG$_{100K}$ mass fractions are 14 m% and 0.7 m%, respectively.

Table 4.10. The composition of photo-crosslinked hydrogels initiated by Ru/APS at 405 nm

Network	Hydrogel	μ_{DMA} $m\%$	μ_{100K} $m\%$	n_{Ru} mmol	n_{Ru}/n_{APS}
SN14$_{1/100}$	SN-14$_{1/100}$	14	0	2	1/100
semi-IPN14$_{1/100}$	semi-0.7$_{1/100}$	14	0.7	2	1/100
	semi-2.4$_{1/100}$	14	2.4	2	1/100
	semi-3.5$_{1/100}$	14	3.5	2	1/100
SN14$_{1/2000}$	SN-14$_{1/2000}$	14	0	0.1	1/2000
semi-IPN14$_{1/2000}$	semi-0.7$_{1/2000}$	14	0.7	0.1	1/2000
	semi-2.4$_{1/2000}$	14	2.4	0.1	1/2000
	semi-3.5$_{1/2000}$	14	3.5	0.1	1/2000

Ru-initiated hydrogels are photo-crosslinked at 439 mW cm^{-2}, the hydrogels are cured for 300 s. After synthesis, the hydrogels are put in water to follow swelling measurements. As seen in Figure 4.30A, there is no full conversion in both Ru-initiated SN and semi-IPN hydrogels. G are calculated 56 % and 64 % for SN14$_{1/100}$ and SN14$_{1/2000}$, respectively. In general, semi-IPN hydrogels have lower gel content than their SN hydrogels. The gel content of the semi-IPN14$_{1/2000}$ decreases from 61 % to 50 % when μ_{100K} from 0.7 m% to 3.5 m%. The gel content for semi-IPN14$_{1/100}$ no significant change with PEG$_{100K}$.
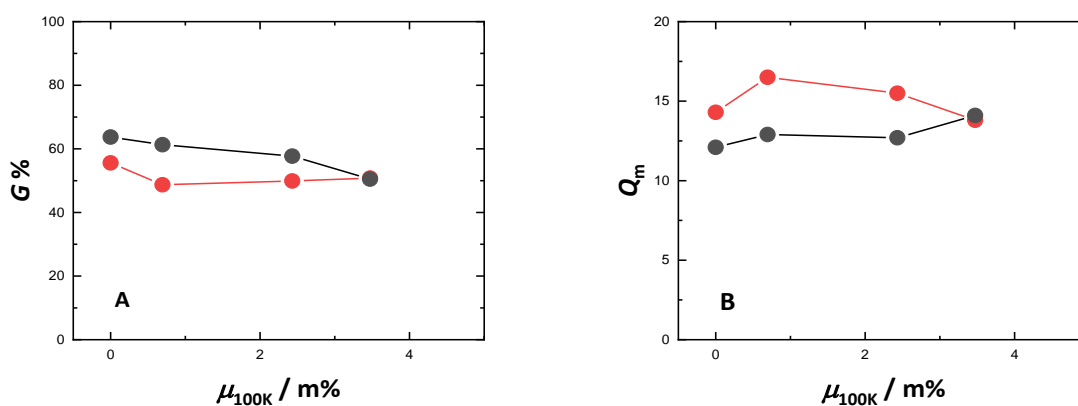
Figure 4.30. A) The gel content, and B) the mass swelling ratio of Ru-initiated SN and semi-IPN hydrogels, semi-IPN14$_{1/2000}$ (black), semi-IPN14$_{1/100}$ (red).

Figure 4.30B shows that Ru-initiated hydrogels do not swell much in water. The expected swelling behavior of each series is observed, and $Q_m \approx 16$ is for semi-IPN14$_{1/2000}$ and $Q_m \approx 13$ for semi-IPN14$_{1/100}$.
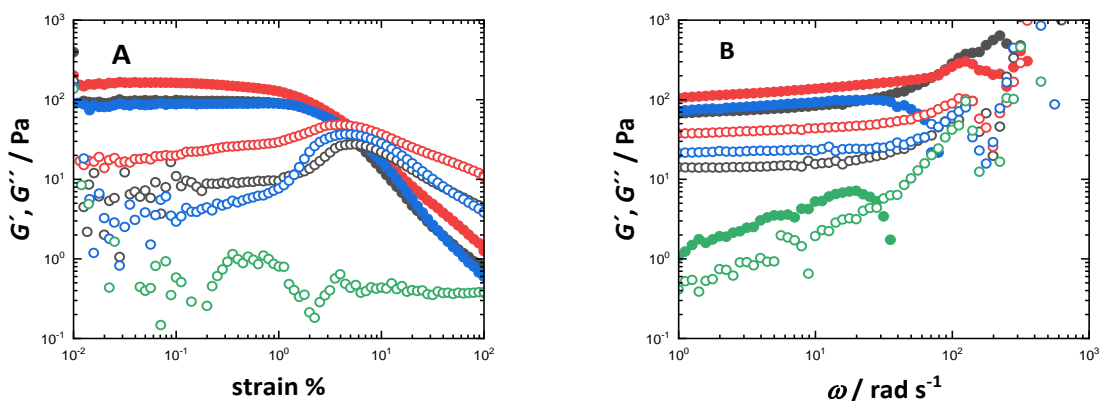
Figure 4.31. Oscillation measurements of LAP-initiated hydrogels after-synthesis. A) Strain sweep at 6.283 rad s^{-1} and B) frequency sweep at strain 1 %, SN14$_{1/2000}$ (black), semi-IPN0.7$_{1/2000}$ (red), semi-IPN2.4$_{1/2000}$ (blue), and semi-IPN3.5$_{1/2000}$ (green).

Ru-initiated hydrogels do not exhibit a straightforward quantitative comparison, unlike LAP-initiated hydrogels. In Figure 4.31A, SN14$_{1/2000}$, semi-IPN0.7$_{1/2000}$ and semi-IPN2.4$_{1/2000}$ hydrogels display a linear viscoelastic region in G' up to 1 % strain. However, the linear behavior is not observed for semi-IPN3.5$_{1/2000}$, indicating a highly dynamic network behavior. Regarding the frequency-sweep shown in Figure 4.31B, G_0 is measured 120 Pa for SN14$_{1/200}$, while it is 90 Pa and 80 Pa for semi-IPN0.7$_{1/2000}$ and IPN2.4$_{1/2000}$, respectively.

To summarize, the rheological characterization of all photo-initiated semi-IPN hydrogels, PEG$_{8K}$DMA contributes to mechanical property, while PEG$_{100K}$ enhances the viscous characteristics. However, this combination results in an irregular trend due to the nature of the semi-IPN system. The existence of linear and relatively longer chains of PEG$_{100K}$ causes the formation of looped regions within the hydrogels. It must be emphasized that photo-initiated radical polymerization might cause inhomogeneity.

4.2.5 Investigation of the manufacturing parameters in 3D printing

PEG-based polymer solutions serve as inks for creating 3D engineered hydrogels by extrusion-based printing. The study explores various manufacturing parameters specific to the developed ink formulations. A critical aspect involves the evaluation of print quality to identify the optimal extrusion parameters. It is accomplished using Ru/APS (1:2000) at 405 nm, and LAP photoinitiator at 365 nm for post-curing. In the final step, circle-shaped printed hydrogels are characterized by focusing on swelling and rheological properties.

The print tests are done by extruding a 2 cm x 2 cm grid structure. For this, a binary solution with a ratio of 20/3.5 is selected due to its moderate viscosity for μ^* (section 4.2.2). The extrusion process for

these structures is examined with the needle diameter (D_N) of 0.25 mm. The specific print parameters are detailed in Table 4.11.

Table 4.11. The printing parameters to test print fidelity

Ink	Parameter	
	Flow rate	Compensation
PEG$_{8K}$DMA/PEG$_{100K}$	mm s^{-1}	mm s^{-1}
20/3.5	2/2	-
20/3.5	2/1.5	1

The applied pressure during extrusion monitors the flow rate v. The flow rate of 2 mm s^{-1} is employed for printing the outer lines, while a slightly reduced flow rate of 1.5 mm s^{-1} is utilized for the inner lines. A compensation mechanism is employed by regulating the upward movement rate of the plunger to reduce over-extrusion after each line is printed. Following these criteria, Figure 4.32 shows the printed grid structures using the 20/3.5 ink formulation.
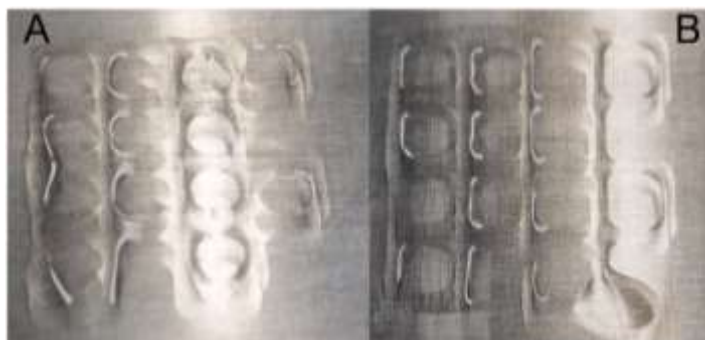
Figure 4.32. The extruded 2 x 2 cm grid structures of 20/3.5 at A) constant flow rate, and B) adjusted flow rate with compensation.

As seen in the printed grid structures, the pores appear in a strongly rounded shape round when the flow rate is 2 mm s^{-1}. With the compensation rate at 1 mm s^{-1}, the pores inside the grids show sharper edges.

A post-curing process is employed to evaluate print quality further to solidify the grid line structures. This post-curing is done at 405 nm for Ru-initiated photopolymerization with a light intensity of 175 mW cm^{-1}. The ink formulation of 20/3.5 is extruded to create 2 cm x 2 cm grid structures. The specific manufacturing parameters are outlined in Table 4.12.

Table 4.12. Printing parameters of Ru-initiated 2 cm x 2 cm grid structures

PEG$_{8K}$DMA/PEG$_{100K}$	Flow rate mm s^{-1}	Compensation mm s^{-1}	Curing speed mm s^{-1}
20/3.5	2/1.5	1	2.5
20/3.5	2/1.5	1	4

The curing speed significantly impacts the printed structures' stability, as seen in Figure 4.33.

Figure 4.33. Ru-initiated 2 cm x2 cm grid structures of 20/3.5. irradiated with of A) The curing speed is 2.5 mm s^{-1} and B) the curing speed is 4 mm s^{-1}. Flow and compensation rate are 2/1.5 mm s^{-1}, respectively.

The grid structure rapidly loses its aqueous state and dries when the curing speed is 2.5 mm s^{-1}. Although the grid structure exhibits a jelly-like property, it seems mechanically weak. Thus, the fabrication of hydrogels initiated by Ru/APS may have manufacturing challenges, as mentioned in section 4.2.2.2. The printing process is examined using LAP as the photoinitiator at 15 mW cm^{-2} (Figure 4.34).
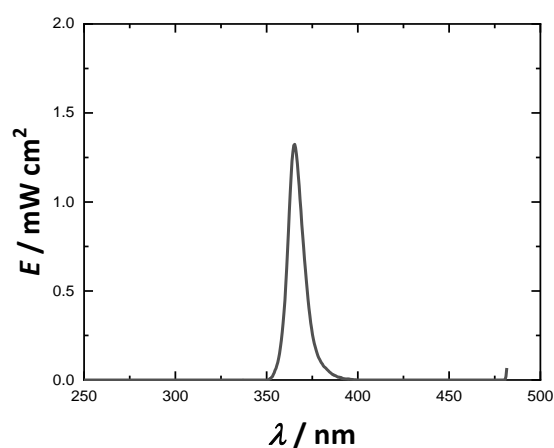
Figure 4.34. Emission spectrum of the light source in 3D printer used for LAP-initiated photopolymerization.

The manufacturing parameters are systemically investigated by the variations the needle diameters, flow rates, and mass fractions of PEG_{100K}.

To explore the impact of flow rates on print quality, extrusion is carried out with a perimeter speed of 25 mm s^{-1} and a compensation rate of 1 mm s^{-1}. The curing speed is set at 3.5 mm s^{-1} to solidify the inks with varying ratios of 20/0, 20/1, 20/3.5, 20/5, 20/7.5, and 20/10. The resulting images of the printed structures are displayed in Figure 4.35.

In Figure 4.35, a clear correlation is observed between v and μ_{100K} for achieving high-quality print fidelity in the ink series of BS_{20}. For 20/0 ($\mu_{100K} = 0$), grid structures cannot be generated at any measured flow rates. The visibility of grid lines is partly improved by 20/1 with an increase in v. In case of $\mu_{100K} > \mu^*$, well-designed grid structures can be successfully produced at all flow rates. For 20/3.5 and 20/5, moderate print quality is achieved, which slightly improves with higher flow rates. When μ_{100K} increases to 7.5 m% and 10 m%, the grid structures can be shaped with well-defined, sharp edges. Generally, v of 4/2 mm s^{-1} provides the sharpest pore edges at all μ_{100K}.

To assess the impact of D_N on print quality, extrusion is carried out with a perimeter speed of 25 mm s^{-1} and a compensation rate of 1 mm s^{-1}. From our previous printing experiments, $v = 4/2$ mm s^{-1} is chosen as the optimal flow rate. The curing speed remains constant at 3.5 mm s^{-1} for solidifying the inks with varying ratios of 20/0, 20/1, 20/3.5, 20/5, 20/7.5, and 20/10. The resulting images of the printed structures are displayed in Figure 4.36.

According to the grid structures in Figure 4.36, it is observed that print fidelity is also dependent on D_N. The grid structures cannot be entirely created at all measured flow rates for 20/0 ($\mu_{100K} = 0$), and 20/1. In the case of $\mu_{100K} > \mu^*$, the print quality can be enhanced at all investigated D_N. 20/3.5 and 20/5 have a moderate print quality at the operated manufacturing conditions. The shape fidelity is comparably developed with an increase in D_N and μ_{100K}, as seen in the image of 20/7.5. When μ_{100K} increased to 10 m%, the grid structures can be shaped with better sharp edges. According to pore wall evaluations, as D_N decreases, the sharpness of the pore edges can be improved a decrease in μ_{100K}. For instance, $D_N = 0.33$ mm is the ideal for 20/7.5, while $D_N = 0.41$ mm is the optimum for 20/10.
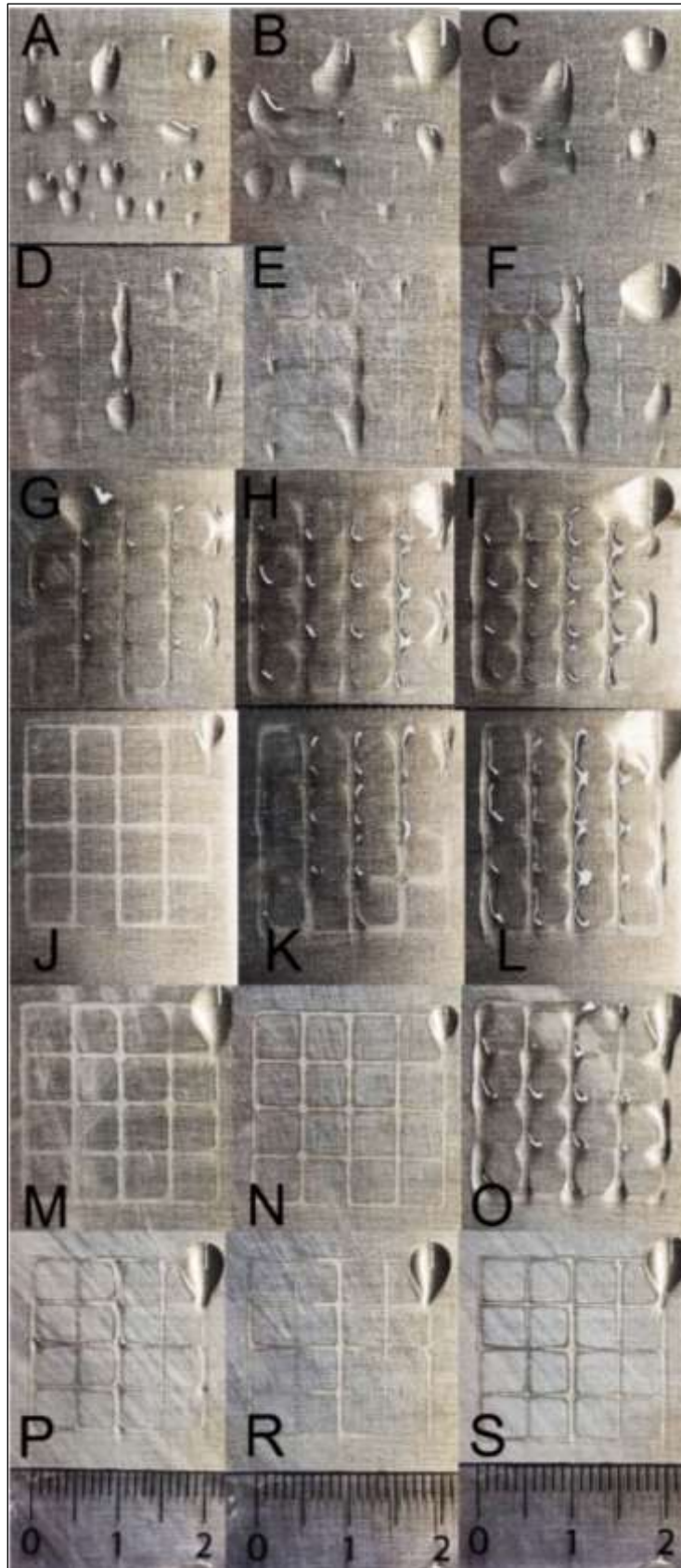
Figure 4.35. The LAP-initiated 2 cm x2 cm grid structures at three different flow rates: A) 3/1.5, B) 4/2, C) 5/2.5 for 20/0; D) 3/1.5 E) 4/2, C) F) 5/2.5 for 20/1; G) 3/1.5, H) 4/2, I) 5/2.5 for 20/3.5; J) 3/1.5, K) 4/2, L) 5/2.5 for 20/5; M) 3/1.5, N) 4/2, O) 5/2.5 for 20/7.5; p) 3/1.5, R) 4/2, S) 5/2.5 for 20/10. D_N = 0.25 mm.

Figure 4.36. The LAP-initiated 2 x 2 cm grid structures at three different needle diameters: A) 0.25 mm, B) 0.33, C) 0.41 for 20/0; D) 0.25 mm, E) 0.33, F) 0.41 for 20/1; G) 0.25 mm, H) 0.33, I) 0.41 for 20/3.5; J) 0.25 mm, K) 0.33, L) 0.41 for 20/5; M) 0.25 mm, N) 0.33, O) 0.41 for 20/7.5; P) 0.25 mm, R) 0.33, S) 0.41 for 20/10. $v = 4/2$ mm s^{-1}.
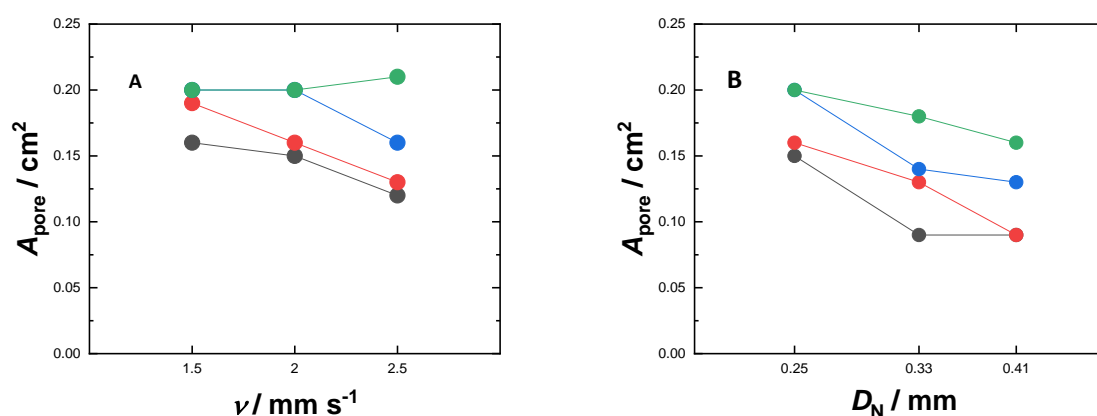
Figure 4.37. A) The calculated pore area of the LAP-initiated grid structures as the function of flow rate of inner line, $D_N = 0.25$ mm. B) The pore area of the grid structures as the function of the needle diameter, $v = 4/2$ mm s^{-1}. 20/3.5 (black), 20/5 (red), 20/7.5 (blue), and 20/10 (green).

As a result of all testing parameters, the pore area A_{pore} of the grid structures is plotted in Figure 4.37 as the functions of v and D_N. The assessment of A_{pore} is the most important criteria evaluating of the print quality in the 2 mm x 2 mm grid structure. Theoretically, one is to expect each pore to be 0.25 cm^2. However, in practice, A_{pore} is influenced by the sharpness of the pore walls. Consequently, extrusion with larger pore wall dimensions leads to a reduction in the square area A_{pore}. Figure 4.37A illustrates that A_{pore} for the 20/10 composition approaches the theoretical value across all investigated v values. For the other grid structures, A_{pore} decreases as v increases. As shown in Figure 4.37B, A_{pore} decreases with an increase in D_N, independent from μ_{100K} value. A_{pore} for the 20/10 composition is less affected by changes in D_N.

To summarize all characterization, some inks show an advanced formulation in manufacturing test parameters. Significantly, the ink of 20/10 shows an excellent performance considering rheological requirements (see section 4.2.1) and printability. The formulated inks are considered for 3D printable hydrogels are summarized in Table 4.13.

Table 4.13. Comparison of the developed inks according to the composition, viscosity, and printability

Ink	μ_{DMA} $m\%$	μ_{100K} $m\%$	η_0 Pa s	η^* Pa s	η_w Pa s	Flow behavior	Printability
20/10	20	10	0.750	0.390	0.340	Shear thinning	very good
20/5	20	5	0.150	0.125	0.100	Shear thinning	good
20/3.5	20	3.5	0.019	0.026	0.080	Newtonian	moderate

The advanced ink of 20/10 is extruded to obtain its printed hydrogel. The extrusion steps of the ink are illustrated in Figure 4.38.

Figure 4.38. Schematic illustration of 3D printing of hydrogels.

Fabricating these gels depends on the filling process, meaning printing takes longer than printing grid structures. Maintaining a high flow volume is necessary to ensure achieving hydrogels with sufficient mass and diameter. To achieve this goal, we keep the flow rate, perimeter, and curing speed fixed at 5 mm s^{-1} and use a needle with a slightly larger diameter of 0.51 mm. The LAP-initiated hydrogels are then fabricated using a post-curing method with a light intensity of 15 mW cm^{-2} at 365 nm. Figure 4.39 displays the images of the hydrogels.
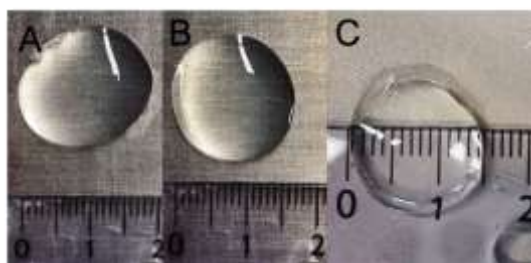
Figure 4.39. The LAP-initiated printed hydrogels with a post-curing method irradiance of 15 mW cm^{-2} at 365 nm. A) 20/5, B) 20/7.5, and C) 20/10.

Transparent semi-IPN hydrogels with $\mu_{100K} > \mu^*$ are printed in an extrusion-based system, and their diameter is measured immediately after manufacturing. As μ_{100K} increases, there is an observable decrease in the size of the hydrogels. This suggests that the extruded inks become more stable with higher viscosity. Additionally, there is a significant increase in the hydrogel thickness when μ_{100K} is 10 m%.

The gel content G, and the mass swelling ratio Q_m of the printed gels are calculated and plotted in Figure 4.40.

Figure 4.40A shows that the manufactured PEG$_{8K}$DMA/PEG$_{100K}$ gel content does not fully convert hydrogels. A slight decrease is seen with the increase of μ_{100K}. One possible reason for the lower conversion in printed hydrogels could be attributed to the oriented structure of the linear polymers during extrusion. In Figure 4.40A, $Q_m \approx 20$ is calculated at all μ_{100K}. The measured values for LAP-initiated printed hydrogels appear to be lower than those of their conventional hydrogels.
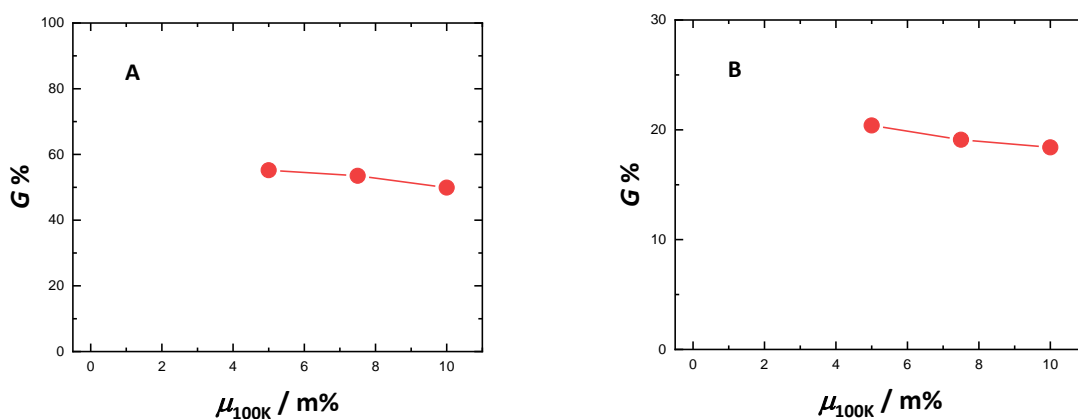
Figure 4.40. A) The gel content, and B) the mass swelling ratio of LAP-initiated printed hydrogels.

The rheological properties of swollen equilibrium LAP-initiated printed hydrogels are investigated by rheometry. Figure 4.41 shows the rheological measurements.
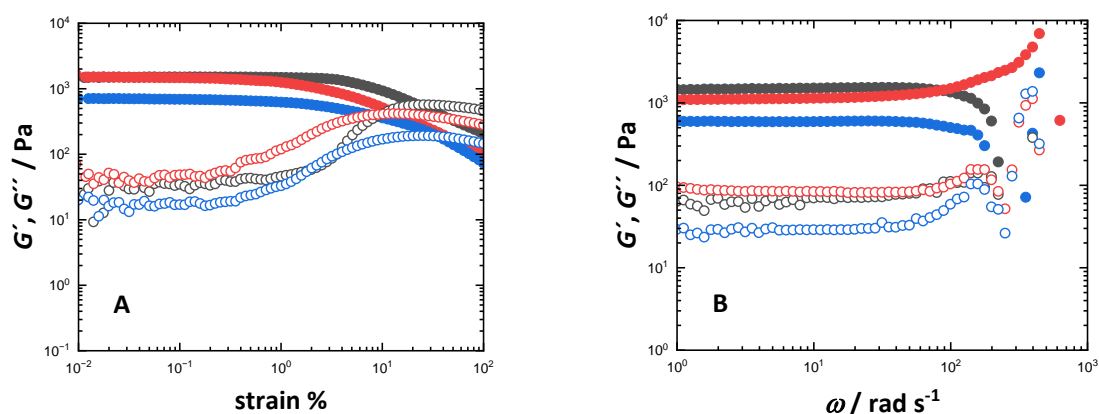
Figure 4.41. A) Strain-sweep measurement of the LAP-initiated printed hydrogel at 6.626 rad s^{-1}. B) Frequency-sweep of the LAP-initiated printed hydrogel at strain 1 %: 20/5 (green), 20/7.5 (cyan) and 20/10 (purple).

As seen in Figure 4.41A, the elastic response of swollen LAP-initiated printed semi-IPN$_{20}$ hydrogels shows LVR in G' up to 1 % strain. This linear behavior decreases as μ_{100K} increases. Notably, the printed semi-IPN$_{20}$ hydrogels prepared at $\mu_{100K} > \mu^*$ that indicates an ideal hydrogel formation. The frequency-sweeps in Figure 4.41B, their curves indicate a high stiffness. In addition, G_0 value for 20/10 is calculated at 1500 Pa. As μ_{100K} increases, G_0 decreases and 1120 Pa and 60 Pa are calculated for 20/7.5 and 20/5, respectively.

The printed hydrogels exhibit better mechanical properties, although their gel content is lower than the hand-made hydrogels. The ideal network formation of the printed hydrogels can be the result of the orientation of the linear polymer during the extrusion.

4.2.6   Conclusion

PEG-based solutions are being explored by adjusting the mass fractions. The mass fraction of PEG100K significantly developed the flow properties with entanglement in the binary solutions. On the other hand, the functional polymer $PEG_{8K}DMA$ contributes to viscoelasticity due to the methacrylate pendant groups. The binary precursors of $PEG_{8K}DMA/PEG_{100K}$, including the LAP photoinitiator, can be converted into a photo-crosslinked network by UV irradiation at 365 nm. The flow stability shape fidelity of the ink points out the importance of viscosity. The binary solution of 20/10 prepared above the entanglement mass fraction of PEG_{100K} is the most favorable formulation, leading to optimal print fidelity. Specifically, the printed hydrogels in the IPN_{20} class exhibit elastic moduli ranging from 1500 Pa to 650 Pa.

4.3 Characterization of photolabile linkers and photodegradable poly(acrylamide) hydrogels

Photocleavable compounds based on o-nitrobenzyl (NB) are widely favored in hydrogels due to their biocompatibility and effective responsiveness to light. These compounds possess photolytic properties that can be employed by incorporating various labile bonds, such as ester, amide, carbonate, and carbamates at specific cleavage sites.[129] When exposed to light, PEG-based photodegradable hydrogels containing NB photolabile linkers have outstanding photodegradation capabilities.[125]

A category of photodegradable materials provides the ability to control and adjust properties within a targeted system. These materials are used in diverse applications such as drug delivery,[175] polymer design,[176] and tissue engineering[177] primarily driven by the influence of photodegradable components. The specific class of these materials can be determined by photolabile linker, which plays a pivotal role in operating the material performance. Absorption maxima and quantum yields of the compound influence the structural properties of matrices.

In this chapter, UV-Vis spectrometry investigates photolytic activities of NB-based photo linkers in solution state. P(AAm)-based copolymer hydrogels are synthesized to analyze the gel-state photodegradability of the photolabile linkers. At the end, 3D photopatterning is employed for the hydrogels at various crosslinking ratios based on multi-photon absorption.

4.3.1 Synthesis of poly(ethylene glycol)-based photolabile linker

A photodegradable PEG-based compound, specifically a nitrobenzyl ether-derived unit, is chosen due to its high photolytic efficiency and susceptibility to light-induced degradation. Comparable light-sensitive functionalities are employed by multi-step modification in a synthetic approach.[35] To create a foundational photodegradable monomer, the process involves methacrylation of this photolabile moiety using a hydroxyl group attached to a photodegradable methacrylate, as shown in Scheme 4.4.

Scheme 4.4. Synthesize of the methacrylated o-nitrobenzylether moiety
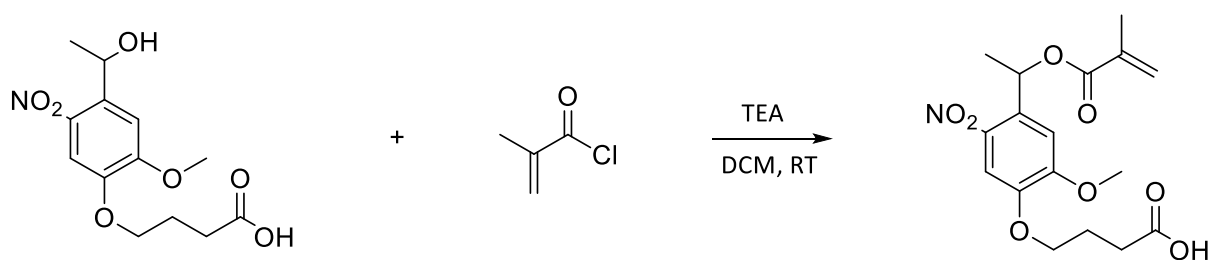
The methacrylate photolabile moiety is synthesized by using a pendant hydroxyl group, yielding photodegradable methacrylate (Scheme 4.5) In this step, we attach methacrylated o-nitrobenzylether to PEG–*bis*-amine (2000 g mol^{-1}), leading to a photocleavable dimethacrylate macromer called PL$_{PEG}$. As a result of multi-step synthesis, the photodegradable methacrylated PEG-based macro photo linker (PL$_{PEG}$) is obtained at the functional degree of $f \approx 76$ %. ^{1}HNMR spectrum is presented in Figure 4.42

Scheme 4.5. Synthesize of the photodegradable methacrylated PEG-based macro photo linker (PL$_{PEG}$).
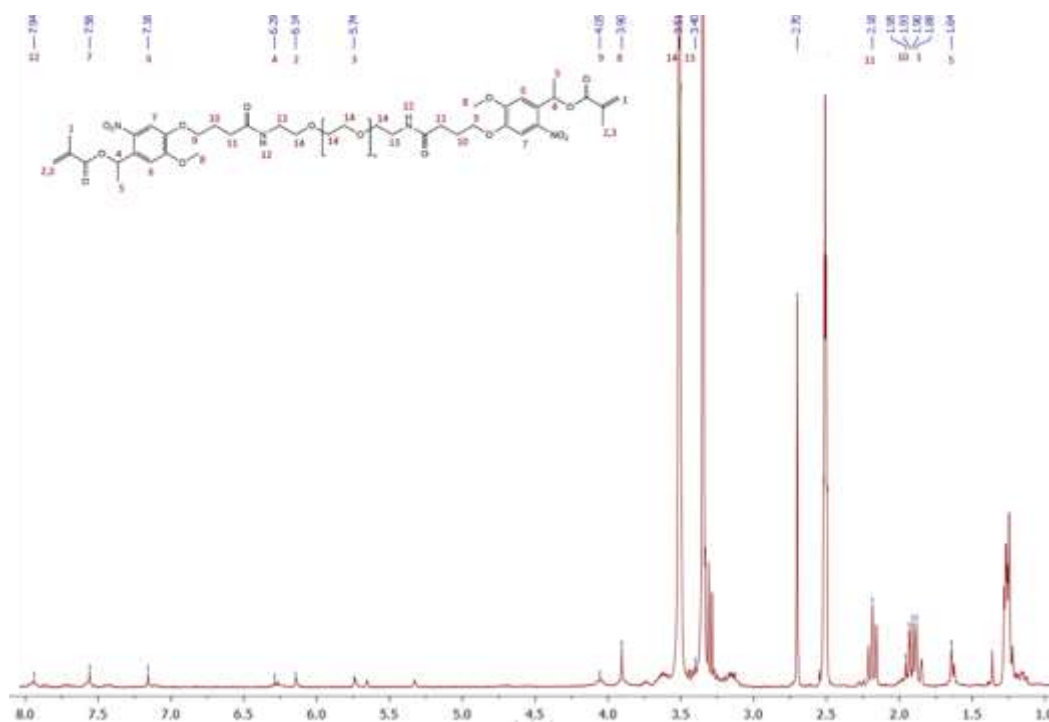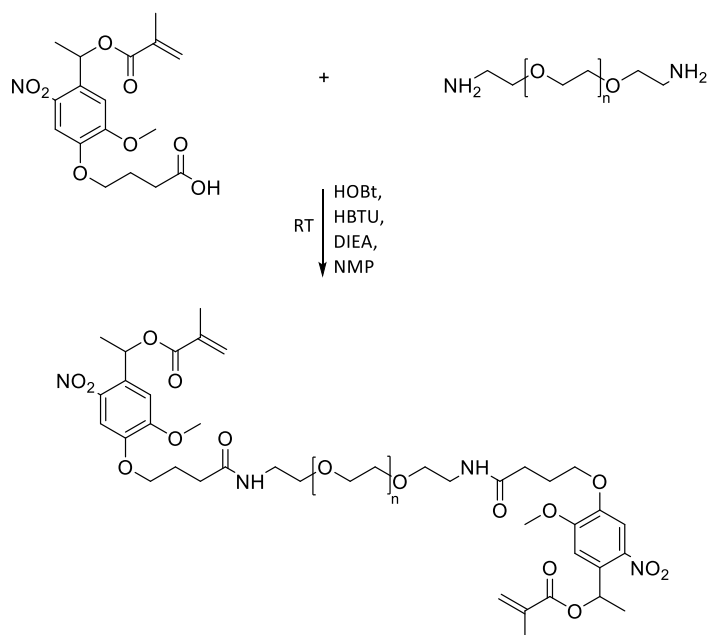
Figure 4.42. 1H-NMR spectrum of the photodegradable methacrylated PEG-based macro photo linker (PL$_{PEG}$).

The methylene protons of the ethylene glycol repeating units appear at 3.51 ppm, and the junction proton of ethylene glycol belongs to the peak at 4.31 ppm. The protons of the vinyl group are seen at 5.74 ppm and 6.14 ppm, indicating the occurrence of methacrylation.

4.3.2 Characterization of o-nitrobenzyl photolabile linkers by UV-Vis spectrometry

UV-Vis spectrometry measurements are systemically followed by preparing their diluted solutions; $c = 5.37 \; 10^{-4}$ mol L^{-1}, $c = 2.68 \; 10^{-4}$ mol L^{-1}, $c = 1.34 \; 10^{-4}$ mol L^{-1}, $c = 0.67 \; 10^{-4}$ mol L^{-1}, and $c = 0.34 \; 10^{-4}$ mol L^{-1} for all photo linkers. The prepared solutions are placed in quartz cuvettes with a path length of 1 x 10^{-2} m^2.

For the degradation kinetics, $2.68 \; 10^{-4}$ mol L^{-1} solutions are irradiated with the light intensity of 0.83 mW cm^{-2} in a UV chamber. The quartz cuvettes are irradiated in the UV chamber at 365 nm. The absorbance spectra of the irradiated samples are analyzed to determine the quantum yields.

The synthesized macro crosslinker of PL$_{PEG}$ is a water-soluble compound. UV-Vis spectrometry analyzes its aqueous solutions and absorbance curves in Figure 4.43.
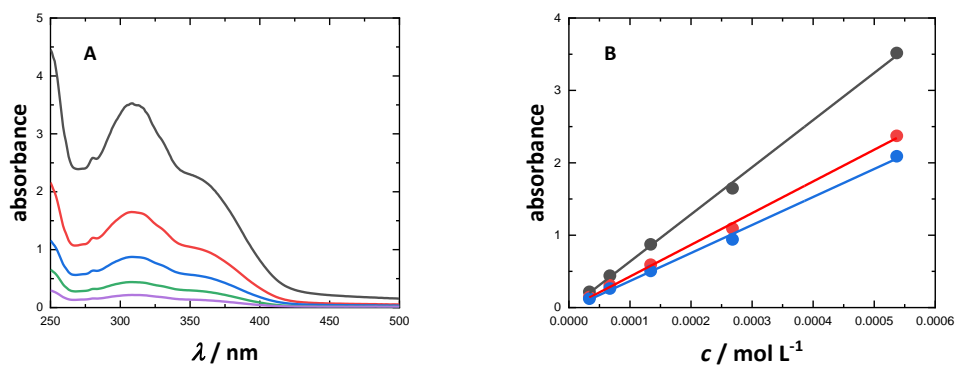
Figure 4.43. A) Absorption spectra of the aqueous PL$_{PEG}$ solutions. $c = 5.37 \; 10^{-4}$ mol L^{-1} (black), $c = 2.68 \; 10^{-4}$ mol L^{-1} (red), $c = 1.34 \; 10^{-4}$ mol L^{-1} (blue), $c = 0.67 \; 10^{-4}$ mol L^{-1} (green), and $c = 0.34 \; 10^{-4}$ mol L^{-1} (purple). B) The calibration curves for 307 nm (black), 345 nm (red), and 365 nm (blue).

In Figure 4.43A, UV-Vis spectra of PL$_{PEG}$ represents a typical UV photo linker with two absorption maxima at 307 nm and 343 nm. The molar absorption coefficients of the photo linker are calculated using equation 2.38. From the calibration curves seen Figure 4.43B, the highest molar absorption coefficient is calculated at 6494 mol L^{-1} cm^{-1} at 307 nm. The molar absorption coefficients are lower at 365 nm and 345 nm calculated 4380 mol L^{-1} cm^{-1} and 3870 mol L^{-1} cm^{-1}, respectively.

The solution-state photodegradation kinetics is analyzed by following the absorbance maximum of each curve after irradiation.
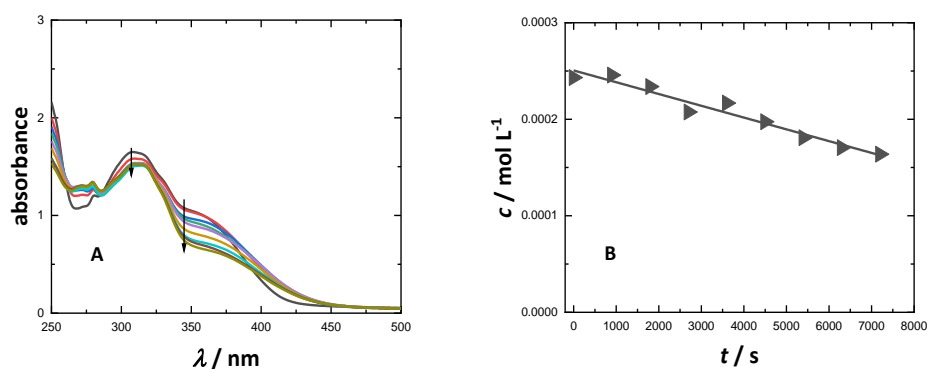
Figure 4.44. A) Absorbance-wavelength spectra of the irradiated aqueous PL$_{PEG}$ solution irradiated at 0.83 mW cm^{-2}, c = 2.68 10^{-4} mol L^{-1}. The curves correspond to the following irradiation times: t_{irr} = 0 (prior to irradiation) (black), t_{irr} = 900 s (red), t_{irr} = 1800 s (blue), t_{irr} = 2700 s (green), t_{irr} = 3600 s (purple), t_{irr} = 4500 s (brown), t_{irr} = 5400 s (cyan), t_{irr} = 6300 s (dark brown), t_{irr} = 7200 s (dark yellow). B) Plot of concentration-irradiation time with curve fitting using linear regression fit.

Figure 4.44A displays a decrease in the absorbance maxima with irradiation time. The decrease in the absorbance in the range of 300 nm - 365 nm indicates the occurrence of a photocleavage of PL$_{PEG}$ in the solution state.[178] Figure 4.44B shows the change in the concentration during photodegradation. The rate constant k (mol L^{-1} s^{-1}) can be described assuming a zero-order rate.

$$\frac{-d[\text{PL}]}{dt} = k \tag{4.7}$$

$k_{\text{PL}_{\text{PEG}}} = 1.22 \times 10^{-8}$ mol L^{-1} s^{-1}, and the quantum yield of PL$_{PEG}$, $\phi_{\text{PL}_{\text{PEG}}} = 0.0454$ calculated according to equation 2.39.

In contrast to PL$_{PEG}$, the other NB-based photo linkers have no repeating units, they are functional with acrylate end groups. The photo linker with the ester labile group is described as PL$_{est}$. The other has carbamate labile group at methyl substituted benzylic position, named PL$_{carb}$.

Scheme 4.6. Chemical structure of the photo linkers. A) PL$_{est}$ and B) PL$_{carb}$
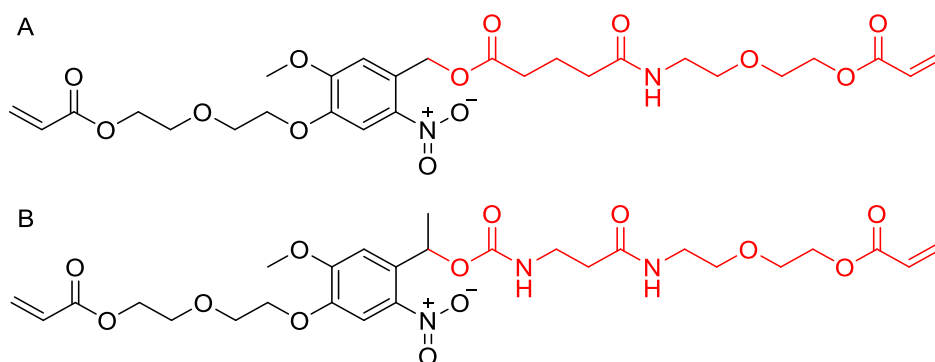
The photo linkers are poorly water-soluble compounds. They are dissolved in water/ethanol (1:1 v/v) to analyze by UV-Vis spectrometry. The outcomes are demonstrated in Figure 4.45.
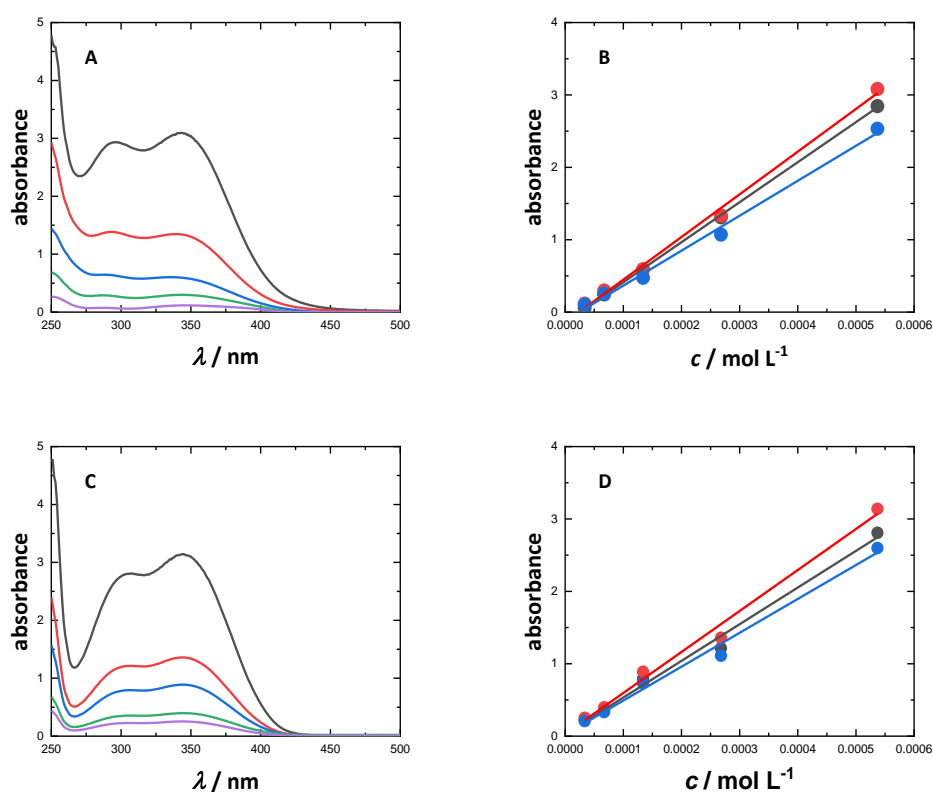
Figure 4.45. Absorption spectra of the A) PL_{est} and C) PL_{carb} in water/ethanol (1/1 v/v %) solutions. c = 5.37 10^{-4} mol L^{-1} (black), c = 2.68 10^{-4} mol L^{-1} (red), c = 1.34 10^{-4} mol L^{-1} (blue), c = 0.67 10^{-4} mol L^{-1} (green), and c = 0.34 10^{-4} mol L^{-1} (purple). The calibration curves of B) PL_{est} and D) PL_{carb} for 307 nm (black), 345 nm (red), and 365 nm (blue).

The presence of two distinct absorption maxima is observed in the UV-Vis spectra. Specifically, for PL_{est}, absorbance maxima are located at 295 nm and 343 nm. A slight bathochromic effect is observed when the labile bond changes to carbamate; PL_{carb} shows absorbance maxima at 307 nm and 345 nm. According to the literature,[129] it is expected that both photo linker exhibit moderate molar absorption coefficients in the UV range as seen Table 4.14.

Table 4.14. The molar extinction coefficients of PL_{est} and PL_{carb}

Photo linker	Molar absorption coefficient, ε		
	mol L^{-1} cm^{-1}		
	λ_{307}	λ_{345}	λ_{365}
PL_{est}	5529	5897	4828
PL_{carb}	5066	5563	4681

For the solution-state photodegradation kinetics, the photolytic behaviors of the PL_{est} and PL_{carb} in water/ethanol (1:1, v/v) are analyzed by UV-Vis spectrometer. Their absorbance curves are displayed in Figure 4.46.
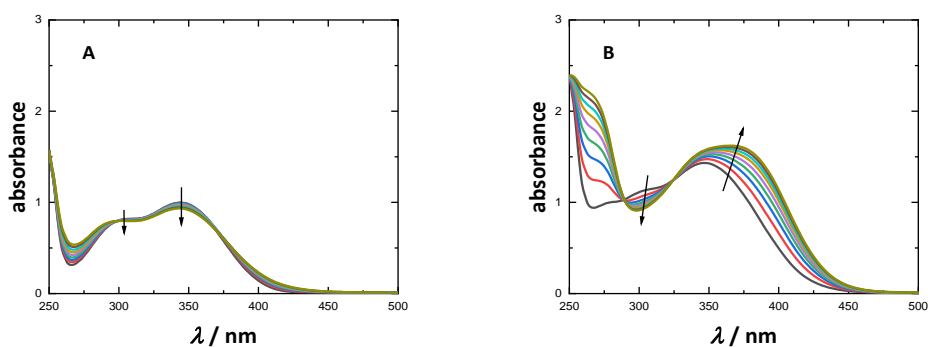
Figure 4.46. Absorbance-wavelength spectra of the irradiated A) PL$_{est}$ and B) PL$_{carb}$ in water/ethanol (1:1 v/v) irradiated at 0.83 mW cm^{-2} in UV chamber, c = 2.68 10-4 mol L^{-1}. The curves correspond to the following irradiation times: t = 0 (prior to irradiation) (black), t_{irr} = 900 s (red), t_{irr} = 1800 s (blue), t_{irr} = 2700 s (green), t_{irr} = 3600 s (purple), t_{irr} = 4500 s (brown), t_{irr} = 5400 s (cyan), t_{irr} = 6300 s (dark brown), t_{irr} = 7200 s (dark yellow).

Figure 4.46A shows the absorption spectra of PL$_{est}$ that there is almost no change with irradiation. Thus, we assume its photodegradation is poor. On the contrary, Figure 4.46B displays the absorbance spectra of PL$_{carb}$. There is a typical absorption behavior indication of a class of α-carbamates compound.[179] The absorption maxima decrease at 307 nm and increases at 345 nm with irradiation.
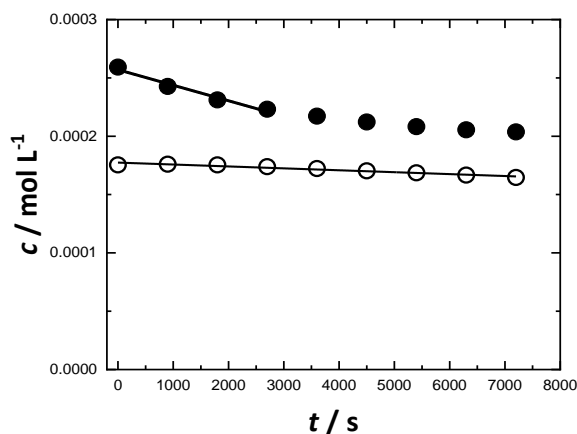
Figure 4.47. Plot of concentration-irradiation time with curve fitting using linear regression fit. PL$_{est}$ (open) and PL$_{carb}$ (filled)

Figure 4.47 shows the photodegradation kinetics of PL$_{carb}$ and PL$_{est,}$ assuming a zero-order photodegradation rate. According to equation 4.7, the reaction rate constants are $k_{carb} = 1.33 \times 10^{-8}$ mol L^{-1} s^{-1} and $k_{est} = 1.74 \times 10^{-9}$ mol L^{-1} s^{-1}. Using the equation 2.39, the quantum yield of PL$_{carb}$, $\phi_{carb} = 0.1450$ is calculated higher than PL$_{est}$, $\phi_{est} = 0.0419$.

Due to the investigation of NB-based photo linkers, the proposed photodegradation mechanism is considered according to the well-known photodegradation mechanism of the 2-nitrobenzyl.[130] The mechanism is displayed based on PL$_{carb}$ in Scheme 4.7. Upon UV irradiation, photo linkers transition from the ground to an excited state. A hydrogen abstraction within the molecule triggers the formation

of an *aci*-nitro form. A cyclization process follows a ring-opening, results in cleavage, and leaving grop (LG) releases as a byproduct.

Scheme 4.7. Photolytic mechanism of PL$_{carb}$
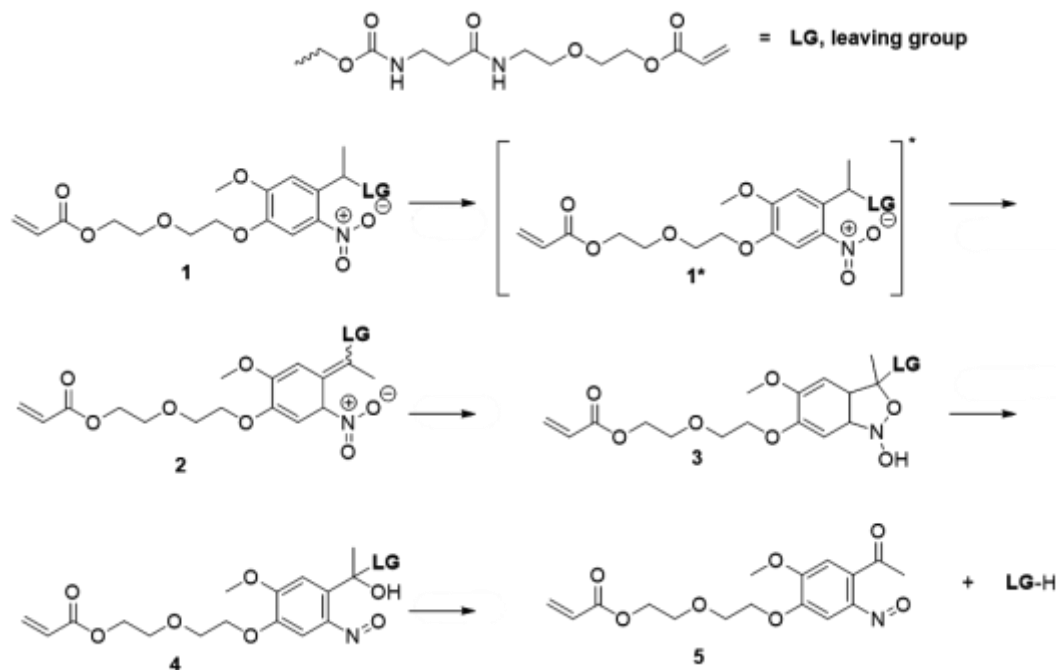
Considering the spectra PL$_{carb}$ obtained by UV-Vis spectrometry (Figure 4.46), the decrease in absorption maxima at 307 nm is attributed to $\pi - \pi^*$ aryl transitions causing photocyclization (compound 3 in Scheme 4.7). Simultaneously, there is an increase in absorption at around 345 nm, indicative of $n - \pi^*$ transitions, associated with the formation of the keto-structure (compound 5 in Scheme 4.7), the photocleaved structure.[180]

Among the other NB-based photo linkers, although PL$_{est}$ shows a higher molar absorption coefficient, its quantum yield needs to be higher. It is assumed that the reaction rate is too slow to cleave the ester labile bond at the benzylic position (compound 3 in Scheme 4.7) which is the rate-determining step.[130] Interestingly, a noticeable change in absorption maxima is observed for PL$_{PEG}$ despite consisting of ester photolabile bonds. The substitution of a methyl group at the benzylic position enhances photocleavage kinetics. In addition, PL$_{PEG}$ is a bifunctional photo linker regarding the number of cleaved labile bonds in a molecule, its photodegradability is assumed to be better than PL$_{est}$.

The photolytic activity of PL$_{est}$ is also tested in the solution state to investigate the effect of a light source on the photolytic activity. In a similar way, the solution of 2.68 x 10^{-4} mol L^{-1} in water/ethanol (1:1 v/v) is irradiated by hand-held lamp ($I_0 = 1.5$ mW cm^{-2}), the absorption spectra are presented in Figure 4.48.
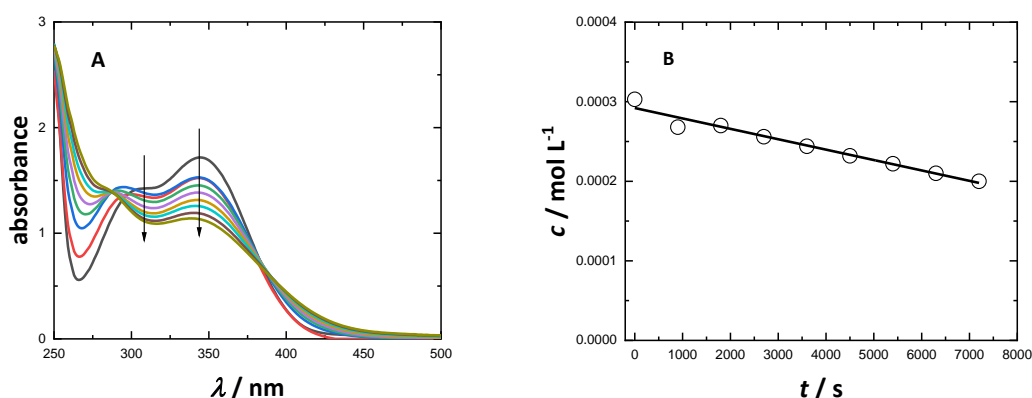
Figure 4.48. Absorbance-wavelength spectra of the irradiated PL$_{est}$ in water/ethanol (1:1 v/v) irradiated by hand-held lamp, I_0 = 1.5 mW cm^{-2}, c = 2.68 10^{-4} mol L^{-1}. The curves correspond to the following irradiation times: t = 0 (prior to irradiation) (black), t_{irr} = 900 s (red), t_{irr} = 1800 s (blue), t_{irr} = 2700 s (green), t_{irr} = 3600 s (purple), t_{irr} = 4500 s (brown), t_{irr} = 5400 s (cyan), t_{irr} = 6300 s (dark brown), t_{irr} = 7200 s (dark yellow). B) Plot of concentration-irradiation time with curve fitting using linear regression fit.

With an increase in the light intensity by using different light sources with a broader light spectrum (see Figure 4.22B), the photolytic activity of PL$_{est}$ is enhanced. Its absorbance maxima decrease with irradiation, and the quantum yield is calculated $\phi'_{est} = 0.3157$ at these conditions.

4.3.3 Photodegradation of polyacrylamide hydrogels

Photolytic behaviors of the NB-based photo linkers are investigated with an in-depth UV-Vis characterization. Specifically, we explore the crosslinking of P(AAm)-based hydrogels using the photo linker. We aim to investigate their suitability for creating 3D patterns by multi-photon lithography. Modifying a polymer network, including a photolabile linker, can significantly influence the stiffness of a hydrogel network upon light irradiation. This can be achieved by increasing crosslinking, resulting in greater stiffness or inducing degradation or cleavage to create softer regions.

Scheme 4.8. Crosslinking of P(AAm) with NB-based photo linkers via redox-initiated free radical polymerizations
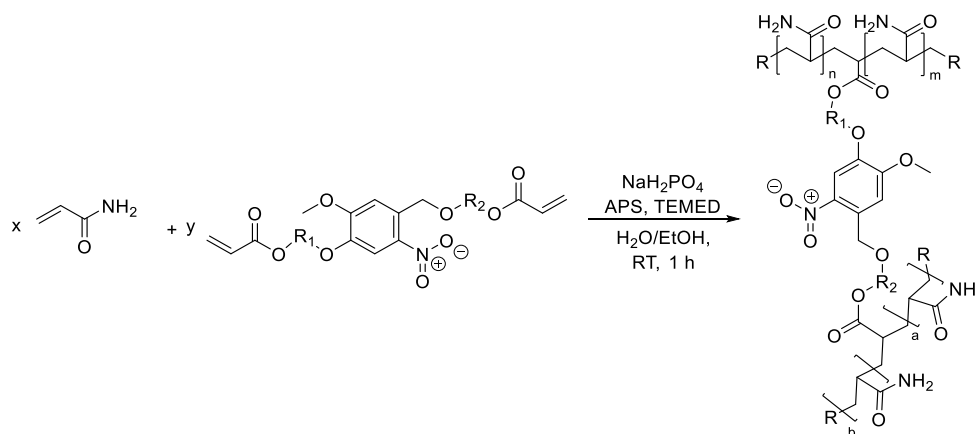
To evaluate the gel-state photocleavage characteristics of PL$_{est}$ and PL$_{carb}$, a redox-initiated free radical polymerization is employed to synthesize P(AAm) copolymer hydrogels. These photo linkers served as crosslinkers in the presence of APS and TEMED. Furthermore, plain hydrogels without photo linker are produced using *N,N'*-methylene-bis(acrylamide) (MBAA) as the crosslinker.

The precursors are used to proceed with the copolymerization for one hour. The synthesized copolymer hydrogels of P(AAm-co-MBAA), P(AAm-co-PL$_{est}$), and P(AAm-co-PL$_{carb}$) put into water, the equilibrium mass swelling ratio, q_m is calculated:

$$q_m = \frac{m_{sw}}{m_d} \qquad (4.8)$$

The obtained results from swelling measurements are shown in Figure 4.49.
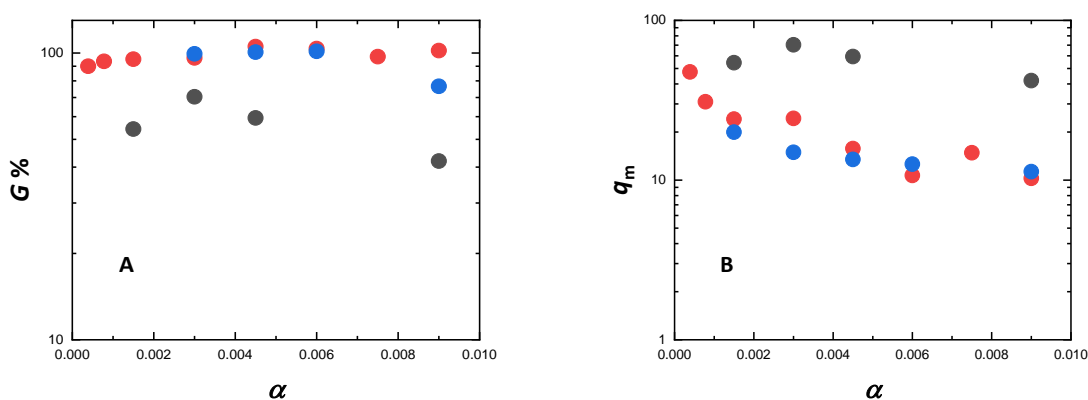
Figure 4.49. A) The gel content of PAAm-based hydrogels, B) The equilibrium mass swelling ratio of PAAm-based hydrogels. P(AAm-co-PL$_{carb}$) (black), P(AAm-co-PL$_{est}$) (red), and P(AAm-co-MBAA) (blue).

Swelling measurements evaluate the network properties of the synthesized hydrogels. Figure 4.49A shows that the gel fractions of P(AAm-co-MBAA) and P(AAm-co-PL$_{est}$) approach to complete monomer conversion, $G > 90\,\%$, except for their hydrogels $\alpha = 0.009$. In contrast, the gel fraction in P(AAm-co-PL$_{carb}$) hydrogels shows lower gel content at all α, in the range of 52 % - 44 %. Despite the low conversion P(AAm-co-PL$_{carb}$) hydrogels demonstrate significantly higher q_m between 42 and 70 depending on the crosslinking ratio (Figure 4.49B). The hydrophilicity of the photolinker can explain this. PL$_{carb}$ exhibits a considerably stronger affinity for hydrogen bonding than the hydrogels crosslinked by PL$_{est}$ and MBAA. With the same considerations, P(AAm-co-PL$_{est}$) hydrogels are slightly more swell than P(AAm-co-MBAA) hydrogels, and their q_m shows a trend line decreasing with an increase in crosslinking ratio.

The influence of NB labile bond chemistry on the rate of photodegradation is investigated by monitoring the swelling measurements of the hydrogels upon irradiation at 365 nm in the UV chamber

at the intensity of 10. 71 mW cm^{-2}, as illustrated in Figure 4.50.
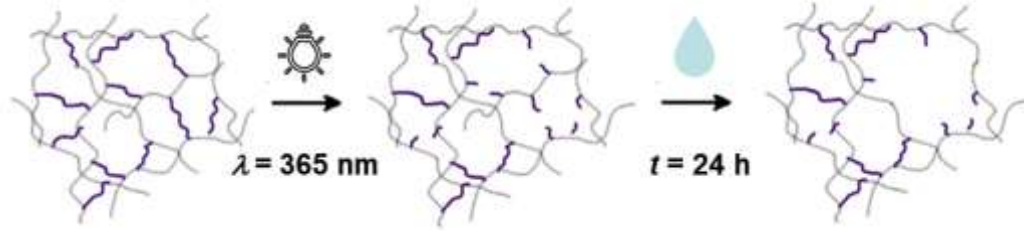
Figure 4.50. Schematic representation of photocleavage and swelling of hydrogels upon irradiation. Photolabile linkers (purple).

The equilibrium mass swelling ratio upon the UV irradiation, $q_{\mathrm{m}}^{\mathrm{UV}}$ is calculated by swelling using the following equation:

$$q_{\mathrm{m}}^{\mathrm{UV}} = \frac{m_{\mathrm{sw}}^{\mathrm{UV}}}{m_{\mathrm{sw}}} \tag{4.9}$$

Here, $m_{\mathrm{sw}}^{\mathrm{UV}}$ represent the swollen mass upon irradiation.

P(AAm-co-PL$_{\mathrm{carb}}$) hydrogel samples are irradiated at 365 nm for 900 s, 1800 s, 2700 s, and 3600 s in the UV chamber. The swelling measurements are followed for P(AAm-co-PL$_{\mathrm{carb}}$) hydrogels upon irradiation.
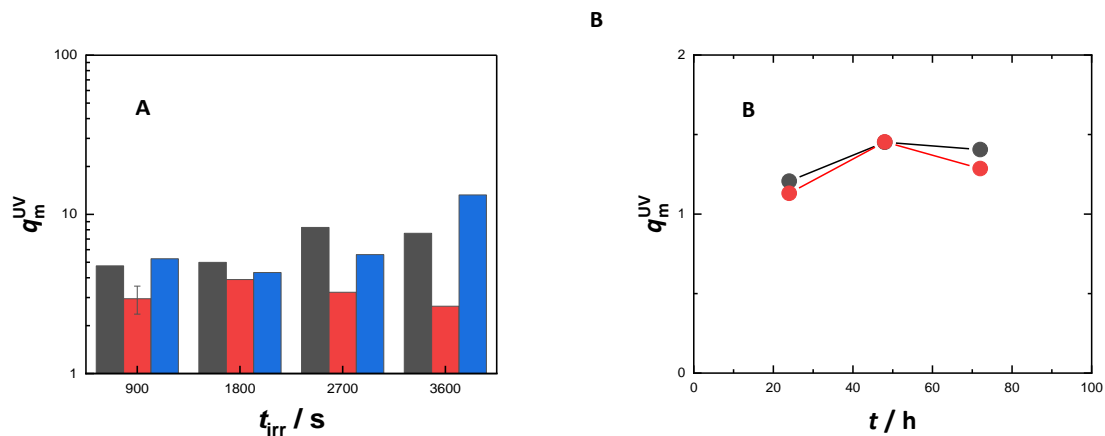
Figure 4.51. A) The equilibrium mass swelling ratio upon UV irradiation at different irradiation time for P(AAm-co-PL$_{\mathrm{carb}}$) hydrogels, α = 0.0015 (black), α = 0.003 (red), and α = 0.0045 (blue). B) The equilibrium mass swelling ratio upon the UV irradiation for P(AAm-co-PL$_{\mathrm{carb}}$) hydrogels at t_{irr} = 300 s, α = 0.003 (red), and α = 0.0045 (blue)

The structure-property relationship after UV irradiation depending on t_{irr} and α:

1. For P(AAm-co-PL$_{\mathrm{carb}}$) hydrogel with $\alpha = 0.0015$, there is a proportional increase in $q_{\mathrm{m}}^{\mathrm{UV}}$ with t_{irr}, up to 2700 s. However, the samples of these hydrogels irradiated at all t_{irr} are leached out. Thus, it is assumed that there is an increase in swelling due to a highly wet state.

2. For P(AAm-co-PL$_{\text{carb}}$) hydrogel of $\alpha = 0.003$, q_{m}^{UV} depends on t_{irr}. When irradiated for a longer time, q_{m}^{UV} is a decreasing trend. Their gels are yellowish gels after UV irradiations, indicating photodegradation.

3. For P(AAm-co-PL$_{\text{carb}}$) hydrogel of $\alpha = 0.0045$, q_{m}^{UV} increases proportionally with t_{irr} in the range of 1800 s to 3600 s, with the appearance of relatively dark yellowish gels after irradiation.

There is a decrease in q_{m}^{UV} when t_{irr} is increased from 900 s to 1800 s, indicating a lower limit to cleave labile bonds in the polymer network. There is a strong relationship between photodegradation and stiffness of the hydrogels (section 2.3.3). The other parameters are the irradiation conditions, such as irradiation time, light intensity, and light source. Figure 4.51 shows that P(AAm-co-PL$_{\text{carb}}$) hydrogels of $\alpha = 0.003$ and show almost no swelling for 72 h, $q_{\text{m}}^{\text{UV}} \approx 1$. Thus, no photodegradation is observed when $t_{\text{irr}} = 300$ s

4.3.4   3D photopatterning

The photocleavage performance of PL$_{\text{carb}}$ in solution state and gel state encourage to use them in 3D photopatterning. Subtractive photopatterning of the swollen hydrogels is accomplished via multi-photon lithography by using a state-of-the-art 3D printer (LightFab GmbH, Aachen). The photodegradable hydrogels are exposed to the pulse energies E_{p} ranging from 150 nJ to 40 nJ. The pulse duration is at 500 fs, with a variable repetition rate f_{rep} of 1.5 MHz and 10 MHz, at 1030 nm. The laser radiation is meticulously focused within the hydrogels using a 20 x / 0.4 objective, resulting in a focal diameter of approximately 2 µm. In the *z*-direction, the distance between two layers is precisely set at 3 µm, while *x*- and *y*-coordinates, the line separation is maintained at 2 µm. The polarization of the laser radiation is circular, remaining independent of the writing direction for the laser-induced structures. 3D patterns are generated on P(AAm-co-PL$_{\text{carb}}$) hydrogels by multi-photon lithography.

The photopatterning is carried out on the P(AAm-co-PL$_{\text{carb}}$) hydrogels at the repeating rate of 1.5 Hz by varying E_{p}. The microscopic images of the cubic patterns are presented in Figure 4.52.

The images visually represent 3D photopatterns on P(AAm-co-PL$_{\text{carb}}$) hydrogels generated by multi-photon absorption. The speckles on the irradiated area indicate bubble formations due to the high laser pulse energy due to surface erosion.[181] These pulses are absorbed by aqueous networks, causing extremely localized heating and sublimation in tiny volumes, forming a small vapor bubble during direct-laser contact. The high-speed processes are directly related to the laser energy and surface chemistry.[182]
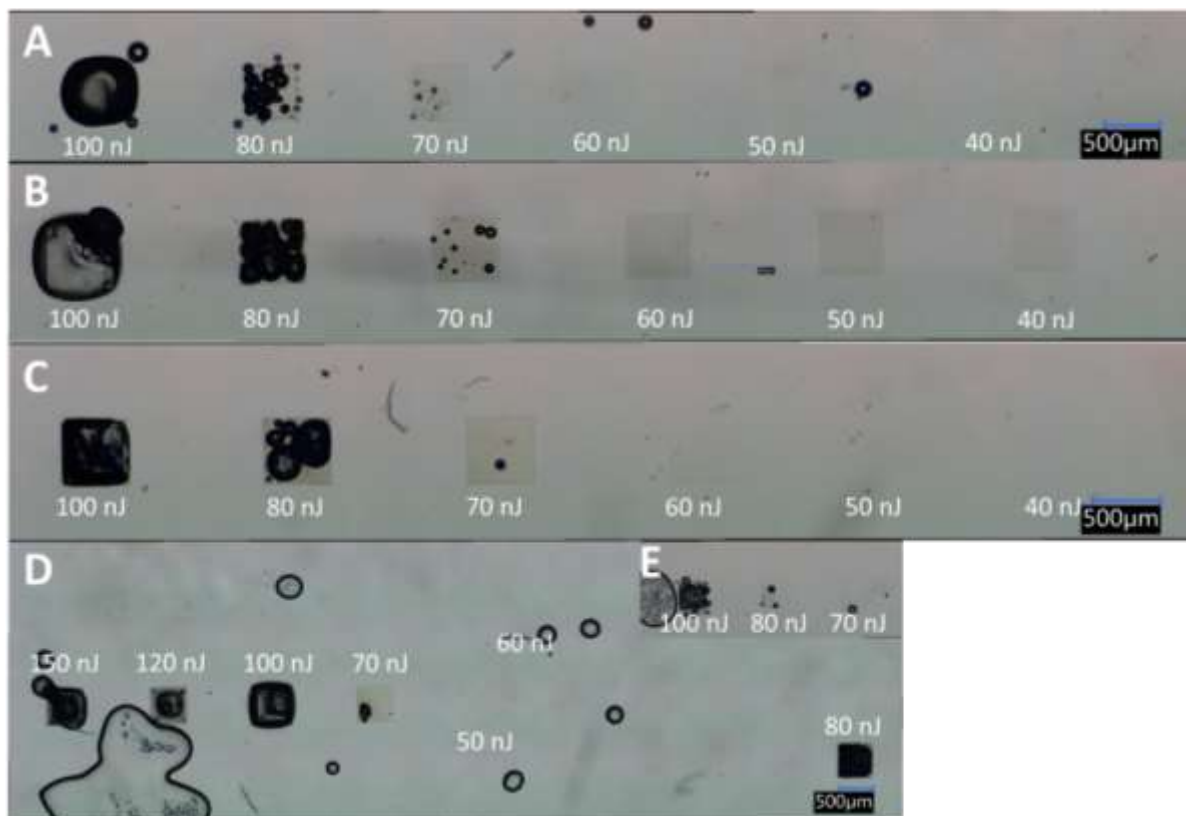
Figure 4.52. 3D patternning of P(AAm-co-PL$_{carb}$) A) $\alpha = 0.0015$ B) $\alpha = 0.003$ C) $\alpha = 0.0045$ D) $\alpha = 0.009$, and E) P(AAm-co-MBAA) $\alpha = 0.009$ hydrogels. The values represent the applied pulsed energy. $f_{rep} = 1.5$ MHz. The scale bar is 500 µm. (LightFab GmbH, Aachen).

As a result, the bubbles are seen when the pulsed energy $E_p > 60$ nJ. On the other, the assessment of photodegradation is based on optical appearance, distinguishing between the irradiated and non-irradiated areas. The yellowish volumes in the images indicate the regions where the crosslinked network undergoes cleavage. As in the reference gel, in the P(AAm-co-MBAA) hydrogel of $\alpha = 0.009$, its irradiated volumes show no color change at the pulsed energy of 70 nJ, 80 nJ, and 100 nJ. In P(AAm-co-PL$_{carb}$) hydrogels, it is observed that the yellowish appearance changes proportional to the crosslinking ratio. Based on this, the P(AAm-co-PL$_{carb}$) hydrogel at $\alpha = 0.0015$ is poor in 3D photopatterning. When the crosslinking ratio increases from 0.0015 to 0.003, the patterned volumes appear milky-white considering a weak performance. In contrast, yellowish volumes are visible for the hydrogels of $\alpha = 0.0045$ and $\alpha = 0.009$, with less bubble at $E_p = 70$ nJ, and partially yellowish at 60 nJ. However, the multi-photon absorption cannot be done when $E_p < 60$ nJ.

A staining experiment is conducted to identify the presence of the cleaved network. The idea is to observe distinct patterns that exhibit a deep yellow coloration, which varies depending on the reaction progress. This coloration phenomenon is expected from a chemical reaction between the dissolved 2,4-dinitrophenylhydrazine (DNPH) in HCl$_{(aq)}$ and the ketone group of the cleaved product (see Scheme 4.9).

Scheme 4.9. The reaction between DNPH and the cleaved polymer network in P(AAm-co-PL$_{carb}$) hydrogels

yellowish   dark yellow / orange
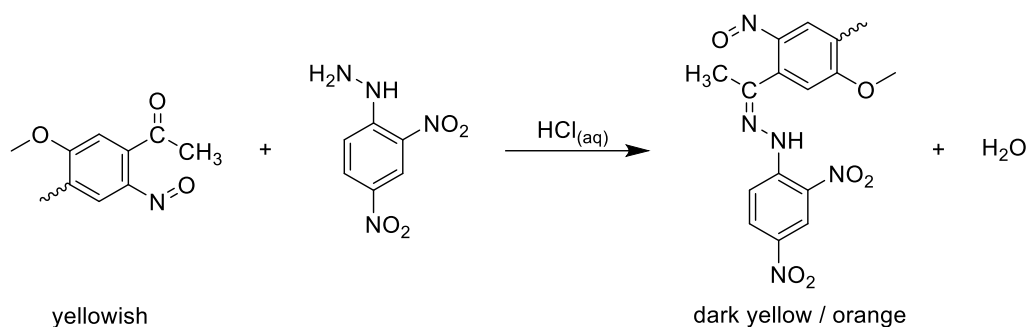
Based on the staining experiment, a vascular branch system is patterned by multi-photon absorption. The photopatterning is carried out on the P(AAm-co-PL$_{carb}$) hydrogels at the pulse energy of 60 nJ with the repeating rate of 1.5 Hz and 10 Hz. The microscopic images of the vascular branch system with staining are shown in Figure 4.53.
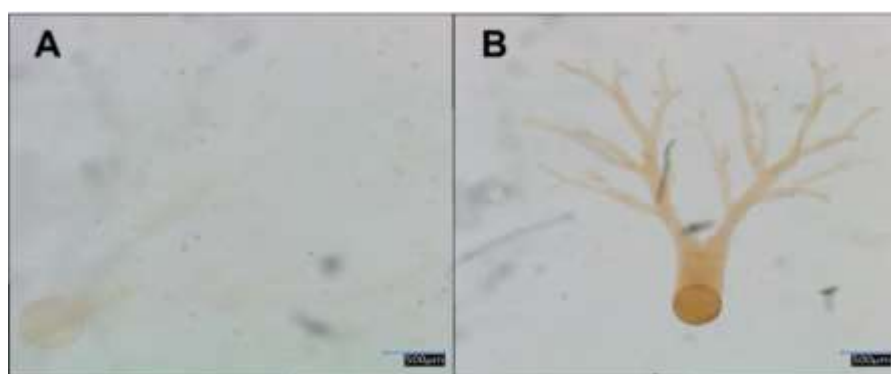
Figure 4.53. The images of vascular patterns on P(AAm-co-PL$_2$) hydrogel of α = 0.0045 with staining experiment at the pulsed energy of 60 MHz. A) f_{rep} = 1.5 MHz B) f_{rep} = 10 MHz. Scale bar 500 μm. Images from LightFab GmbH, Aachen.

Figure 4.53 illustrates a vascular branch model in P(AAm-co-PL$_{carb}$) hydrogel of α = 0.0045 through multi-photon absorption. A photocleavage process occurs within the polymer network, as indicated by staining in the vascular branches. However, this staining is relatively indistinct when using a repetition rate of 1.5 MHz, as seen in Figure 4.53A, In Figure 4.53B, when the repetition rate increases to 10 MHz, the staining is greatly improved, and a vascular branch is done. It is considered that the absorbed energy at a high repetition rate induces laser absorption that is finally feeding the chemical reaction by the repetition rate.

4.3.5 Conclusion

The UV-Vis characterizations of NB-based photo linkers demonstrate the photolytic activities depending on the chemistry of the cleave position. The photo linker of PL$_{carb}$, including carbamate labile bond, generally has a slightly higher quantum yield than that of PL$_{est}$ and PL$_{PEG}$, consisting of ester labile bonds in solution state. In contrast, the molar absorption coefficients are calculated higher when the

labile bond is ester. Among the P(AAm)-based copolymer hydrogels crosslinked by photo linkers at the same crosslinking ratio, P(AAm-co-PL$_{carb}$) hydrogel swells more because of the higher hydrophilicity of the polymer network. 3D photopatterning P(AAm-co-PL$_{carb}$) hydrogel, depending on multi-photon absorption, indicates the influence of process parameters. Finally, the vascularized model is successfully applied for P(AAm-co-PL$_{carb}$) hydrogel $\alpha = 0.0045$ at the pulse energy of 60 nJ and the repetition rate of 10 MHz.

5 SUMMARY

This thesis evaluates the suitability of some synthetic polymers, their solutions, and hydrogels in the context of their promising applications in biological systems. All comprehensive assessments consider the distinct characteristics and properties of the investigated polymer architectures and networks by matching the requirements of tissue engineering within the domains of 3D printing and microscale techniques. The functionalized synthetic polymers of PEG and P(AAm) are specifically designed to exhibit their structural properties that possess unique structural properties to enable them to perform specific functions in their materials. The hydrophilic polymer of PEG diols at various molar masses is successfully functionalized with different end-groups. PCL terminates the high molar mass of PEG backbones to enhance the structural properties in water. The biodegradable and water-resisted PCL improves the thermal properties of the triblock copolymers. PEG is also modified by methacrylate end groups, allowing water-soluble and photopolymerizable macromers of $PEG_{8K}DMA$. $PEG_{8K}DMA$ shows outstanding properties as an intelligent polymer. Its solutions and hydrogels show tunable properties by varying concentrations. The following functional form of PEG is synthesized as a macro crosslinker with NB-based photolabile precursor and methacrylate end groups used as a photodegradable polymer. Photo linkers functionalize the other synthetic P(AAm) to produce their copolymers and conventional networks with MBAAM. The hydrophilicity of P(AAm)-based copolymers is greatly improved with photodegradability.

In the first approach, with the aim of physical crosslinking via hydrophobic associations, amphiphilic triblock copolymers of PCL-PEG-PCL are synthesized by coordination-inserted ring opening polymerization initiated by PEG diols above the critical molar mass. It is demonstrated that the synthetic conditions of the reactions significantly affect the resultant composition of the product. Although the polydispersity of the synthesized triblock copolymers is in the expected range, the presence of PCL-rich side product is detected by SEC measurements. An efficient fractionation method to extract this fraction from the raw product is developed to understand the structure-property relationships. ^{1}H-NMR characterization proves the occurrence of the triblock structure with different block length ratios between the middle block of PEG and the end blocks of PCL. It is concluded that the hydrophilic PEG block dominates the thermal properties of the purified triblock copolymer, and their melting temperatures are around 60 °C. By DLS, the hydrodynamic radius of the aggregated R_D is determined between 250 nm and 470 nm, indicating the state of dispersion of the triblock copolymers in water. However, a sol-gel transition is not observed at an applicable temperature, even in concentrated solutions. It is considered that the critical temperature significantly shifts to higher temperatures by considering that PEG can display UCST properties.

Secondly, PEG diol (8000 g mol^{-1}) is functionalized by methacrylate end groups to allow the production of photo-crosslinked hydrogels in 3D printing approaches. The functional polymer of PEG$_{8K}$DMA is successfully synthesized with a high functionality of $f > 90$. PEG$_{8K}$DMA and PEG$_{8K}$DMA / PEG$_{100K}$ binary solutions are formulated to adjust the viscosity of the 3D inks with varying mass fractions. Concerning the relatively low viscosity profile of diluted and semi-diluted PEG$_{8K}$DMA solutions as a single-component ink, PEG$_{100K}$ is found to be applicable as a viscosity enhancer to adjust the flow behavior and by the introduction of entanglement above the critical concentration of PEG$_{100K}$, $\mu^* = 3.5$ m%. The resulting viscosity and flow behavior are the critical rheological parameters of the polymer solutions concerning their use in an extrusion-based 3D printing process. The binary solutions investigated comprise PEG$_{8K}$DMA mass fractions between 10 m% and 20 m%, and the viscosity is significantly increased up to 10 Pa s^{-1} zero-shear viscosity in the presence of the linear PEG$_{100K}$. Importantly, PEG$_{100K}$ is observed to result in a shear-thinning behavior, which is for the adjustment of 3D-printing parameters. In addition to the shear rate-dependent viscosity behavior, frequency-sweep measurements show the significant viscoelasticity of the formulated potential ink. Complex viscosity curves demonstrate an advanced structural behavior compared to simple polymeric solutions. The presence of entanglements in the final mixture is observed with the oscillation procedure. A weak-gel formation is seen by varying the PEG$_{100K}$ mass fraction. The binary precursor solutions are converted into semi-IPN networks by photopolymerization. According to the free-radical polymerization mechanism, two photoinitiators are used for crosslinking reactions. LAP initiates the photopolymerization in the UV light range at the wavelength of 365 nm. In comparison, the Ru initiator is activated in the presence of co-initiator APS in the visible light range at the wavelength of 405 nm. Swelling measurements and rheology characterize the semi-IPN PEG$_{8K}$DMA / PEG$_{100K}$ hydrogels. Typical semi-IPN properties are observed, in which the chemically crosslinked PEG$_{8K}$DMA provides the overall stability of the polymer networks. At the same time, linear trapped PEG$_{100K}$ plays the role of dissipating the loaded energy. Concerning the whole entanglement of PEG$_{100K}$ to the photo-crosslinked PEG$_{8K}$DMA network, photo initiation with LAP shows a good performance in converting it into hydrogels. The gel fraction shows a declining trend with an increase in PEG$_{100K}$ mass fraction. The solid properties of the hydrogels increase in modulus with an increase in PEG$_{8K}$DMA concentration and a decrease with an increase in PEG$_{100K}$ concentration. A similar trend is also observed for the swelling ratio. The swelling ratios of the IPN$_5$, IPN$_{7.5}$, IPN$_{10}$, and IPN$_{20}$ series of hydrogels significantly vary from approximately 1000 to 9 with the PEG$_{8K}$DMA and PEG$_{100K}$ mass fraction variation. Significantly, the network properties of the IPN20 series can be primarily varied by PEG$_{100K}$ mass fractions. However, it is observed that IPN$_{10}$, IPN$_{7.5}$, and IPN$_5$ hydrogels are more prone to be dominated by PEG$_{100K}$ components that can weaken the stiffness of semi-IPN PEG$_{8K}$DMA / PEG$_{100K}$ hydrogels.

The elastic modulus of IPN_{20} is measured up to 7500 Pa after synthesis, while in the swollen-equilibrium state, hydrogels show elastic moduli between 20 Pa and 50 Pa as a function of PEG_{100K} mass fraction. In 3D-printing method development, the printing quality of the binary solutions is tested by varying mass fraction of the components, needle diameter, and flow rate. Detailed tests on the effect of manufacturing parameters on the properties of printed structures using the LAP photoinitiator, provided the photoinitiation efficiency is observed as effective and directly impacts the created structures' print fidelity. It is observed that the most critical parameter is the mass fraction of PEG_{100K}. As the viscosity enhancer, significantly above the entanglement mass fraction, PEG_{100K} dramatically increases the flow stability of the ink and the print fidelity of the grid structures, showing the considerable contribution of the viscosity. Overall, the binary solution 20/10 (mass fraction of $PEG_{8K}DMA$ / PEG_{100K}) shows an optimum ink formulation. Since one primary parameter is the viscosity of the ink formulation, the other manufacturing parameters are evaluated for this specific composition. In this respect, the employment of the varying needle diameters affects the flow behavior of the inks during the extrusion. In the case of using the needle at smaller diameters, inconsistent capillary flow can be seen for the formulation. Applying these optimized extrusion parameters, the formulated inks of 20/5, 20/7.5, and 20/10 photo-crosslinked semi-IPN hydrogels in the presence of LAP. The gel fractions of the hydrogels, produced at the wavelength of 365 nm with the light intensity of 15 mW cm^{-2}, are around 60 %, and the swelling ratios are calculated around 20. The rheological investigation of the printed hydrogels demonstrates good viscoelastic properties. The plateau moduli of the swollen equilibrium printed hydrogels are calculated between 1500 Pa and 60 Pa depending on the PEG_{100K} fraction, showing the versatility of the approach.

Last, P(Aam)-based photocleavable hydrogels are prepared and investigated concerning their 3D-photopatterning properties. Two photo linkers are employed as crosslinkers, yielding copolymeric network structures. By varying the crosslinker ratio, the P(AAm)-based hydrogels are chemically crosslinked by PL_{est} and PL_{carb} and compared with the hydrogels crosslinked by MBAA. Although P(AAm-co-PL_{carb}) hydrogels exhibit lower conversion, their hydrogels swell much more than P(AAm-co-PL_{est}) and P(AAm-co-bis) hydrogels since the more hydrophilic chemical structure of PL_{carb} probably contributes to swelling properties of the P(AAm) network. Following the concept of this idea, photo linkers, PL_{est} and PL_{carb}, are analyzed in solution state by UV-Vis spectroscopy. Both photo linkers display similar absorption profiles in ethanol/water (1:1 v/v) in a UV light range. Their absorption maxima are detected at around 307 and 345 nm, respectively. Although PL_{est} has a higher molar extinction coefficient than PL_{carb}, the quantum yield is calculated 0.0419 and 0.1450 for PL_{est} and PL_{carb}, respectively. The carbamate functional group and the methyl substituent in the cleavage position are considered to enhance the photolytic efficiency of the PL_{carb}. Regarding photocleave performance in a

gel state, P(AAm-co-PL$_{carb}$) hydrogels are exposed to UV at 365 nm to investigate the relationship between irradiation time and crosslinking ratio. According to the mass swelling ratio upon irradiation, the crosslinked network responds to UV light as expected. Weaker hydrogels are observed as the crosslinking ratio decreases, especially those prepared at $\alpha = 0.0015$. Nevertheless, the mass-swelling ratio of the hydrogels is calculated from 14 to 2 in the tested irradiation time of 300 s, 1500 s, 2700 s, and 3600 s. The P(AAm-co-PL$_{carb}$) hydrogels of $\alpha = 0.003$ and $\alpha = 0.0045$ cannot be cleaved when the irradiation time is 300 s. As a result, 3D photopatterning of P(AAm-co-PL$_{carb}$) hydrogels is performed by multi-photon lithography. Similarly, the relationships between crosslinker ratio and process parameters are investigated by varying the pulse energy and repetition rate. As the crosslinking ratio increases, the required pulsed energy increases. However, bubble formations arise when the pulse energy exceeds 60 nJ at all P(AAm-co-PL$_{carb}$) hydrogels. On the other hand, when the crosslinking ratio decreases, weak 3D patterning is observed on the gel surfaces. The photocleavage is tested for the vascular branch system with a staining experiment; because of expectation, vascularized P(AAm-co-PL$_{carb}$) hydrogels of $\alpha = 0.0045$ are yellowish, indicating the presence of cleaved networks by multi-photon absorption.

In conclusion, this thesis comprehensively assesses synthetic hydrogels created from PEG and P(AAm) derivatives, focusing on their structural properties and potential. One of the key advantages of these hydrogels is their versatility, as they can be designed with tailorable physical and chemical properties. Exploring different crosslinking strategies for producing hydrogels also offers tunable mechanical and chemical properties. Moreover, the advanced manufacturing methods, 3D printing, and multi-photon lithography demonstrate the feasibility of fabricating functional PEG and P(AAm) hydrogels. These techniques highlight the potential for precise and customized fabrication, and this adaptability makes them promising candidates for various biomedical applications, particularly in cell encapsulation.

6 EXPERIMENTAL PART

6.1 Chemicals

ε-caprolactone	ε-CL	Sigma Aldrich	≥98.0%
Dibutyl tin oxide	Bu_2SnO	TCI Chemicals	-
Toluene	$C_6H_5CH_3$	Fisher Scientific	>99.8%
Petroleum ether 40/60	-	techn.	-
Chloroform	$CHCl_3$	Fisher Scientific	>99.8%
Poly(ethylene glycol) (8000 g mol^{-1})	PEG_{8K}	BioChemica	-
Poly(ethylene glycol) (35000 g mol^{-1})	PEG_{35K}	Sigma-Aldrich	-
Poly(ethylene glycol) (100000 g mol^{-1})	PEG_{100K}	Sigma-Aldrich	-
Dichloromethane	DCM	Sigma-Aldrich	≥ 99.5%
Triethylamine	TEA	Sigma-Aldrich	≥ 99.5%
Methacryloyl chloride	MAc	Sigma-Aldrich	97%
Acrylamide	AA	Sigma-Aldrich	≥ 99%
N,N'-Methylenebis(acrylamide)	MBAA	Sigma-Aldrich	99%
Sodium dihydrogen phosphate monohydrate	$NaH_2PO_4.H_2O$	Alfa Aesar	98%
Ammonium persulfate	APS	Sigma-Aldrich	≥ 98%
N, N, N', N'-tetramethylene diamine	TEMED	Alfa Aesar	99%
Taros 36886	PL_{est}	Taros Chemicals	-
Taros 38420	PL_{carb}	Taros Chemicals	-
Lithium-phenyl-2,4,6-trimethylbenzoylphosphinat	LAP	Sigma-Aldrich	≥ 95%

Pentamethylcyclopentadienylbis (triphenylphosphine) ruthenium (II) chloride	Ru	BLD Pharmatech	-
4-(4-(1-Hydroxyethyl)-2-methoxy-5-nitro phenoxy)butanoic acid	-	BLD-Pharmatech	95%
1-Hydroxybenzotriazol monohydrate	HOBt	Sigma-Aldrich	≥ 97%
2-(1H-Benzotriazole-1-yl)- 1,1,3,3-tetramethyluronium hexafluorophosphate	HBTU	Carbolution Chemicals	98%
N, N-Diisopropylethylamine	DIEA	Sigma-Aldrich	≥ 99%
Poly(ethylene glycol) diamine (M_n = 2000 g mol^{-1})	PEG$_{2K}$	IRIS-Biotech	-
Diethyl ether	-	techn.	-
Potassium carbonate	K_2CO_3	-	-
Ethanol	EtOH	techn.	-
(2,4-Dinitrophenyl) hydrazine	DNPH	Sigma Aldrich	97%
Concentrated hydrochloric acid	HCl$_{(aq)}$	tech.	37%

6.2   Methods

Size Exclusion Chromatography (SEC)

Molar mass and molar mass distribution ($PDI = \overline{M}_n/\overline{M}_w$) of all polymers are determined Size exclusion chromatography (SEC) using the solvent of THF-DMA-AcOH (flow rate: 1.000 mL/min, refractive index: 1.403) equipped of light scattering and RI detectors. The light scattering detector of *DAWN HELEOS* is used at a wavelength of 658 nm with a calibration constant of 3.0397 x 10^{-5} 1 (V cm)$^{-1}$, including cell type of K5. The RI instrument of *OptilaB Rex* is set with the calibration constant of 3.4629 x 10^{-5} RUI pixel^{-1}.

Nuclear Magnetic Resonance Spectroscopy (^{1}H-NMR)

^{1}H-NMR measurements are performed on a Bruker Avance I 300 nuclear magnetic resonance spectrometers (frequency [1]H: 300.13 MHz). The measurements are carried out at 298 K, the chemical shifts are given in parts per million (ppm) relative to the solvent signal.

Dynamic Light Scattering (DLS)

High-Performance Particle Sizer (HPPS, Malvern Instruments, laser 633 nm, angle 173°) are used to determine the hydrodynamic diameter of the micelles. All measurements are performed at 25 °C. The measurements of the aqueous polymer solution of 0.05 w/v % are performed in single-used polystyrene cuvettes. The water is filtered before use. The measurements are evaluated according to the *Non-Negative Least-Squares* algorithm.

Differential Scanning Calorimetry (DSC)

The thermal properties were characterized using a differential scanning calorimeter of DSC 821e (METTLER TOLEDO) with FRS5 furnace. The commercially purchased PEG_{8K}, PEG_{35K}, and PEG_{100K}, and the raw and purified PCL-PEG-PCL triblock copolymers are characterized in the temperature between of -10° C and 80° C under a liquid nitrogen atmosphere at a heating/cooling rate of 5 K min^{-1}. While PEG-based aqueous solutions of the aqueous solution of raw and purified PCL-PEG-PCL triblock copolymers are characterized in a temperature range of -30° C to 80° C at the same heating/cooling rate. The second heating-cooling cycle is used to evaluate thermal properties for all measurements.

Rotational Rheology

The rheological measurements are performed by AR-G2 rheometer from TA Instruments. A solvent trap is used to prevent water evaporation from the samples. Time-sweep measurements of solutions are monitored at 25 °C with cone plate geometry (2°, 40 mm) at the strain of 0.5 % and (1 Hz) 6.283 rad s^{-1} of angular frequency. Viscosity measurements of solutions are monitored at 25 °C with cone

plate geometry (2°, 40 mm), peak holds at 4.775 Pa, and continuous ramp between shear stress 10^{-1} - 10^3 s^{-1}, respectively. Oscillation deformation measurements are performed at 25 °C with a plate-plate geometry (20 mm), cone plate geometry (2°, 40 mm) for hydrogels and binary solutions, respectively. Strain-sweep is performed at a frequency of 0.628 rad s^{-1} in the strain of 0.01 % - 100 % for binary solutions and hydrogels. Frequency-sweeps are followed out with linear viscoelastic regime at a constant strain of 0.1 % or 1 % for hydrogels. The plateau moduli of hydrogels are calculated according to frequency-sweep measurements.

Capillary Rheology

Capillary extrusion is performed using *Zwicki* universal test machine with a syringe-needle system for 15 s. A uniaxial force is applied to a syringe at a constant velocity at room temperature. The capillary set-up consists of L_N= 44 ± 0.2 mm needle length, R_N= 0.475 mm of needle inner radius, and R_S= 7.950 mm inner radius of 10 ml syringe as shown in section 4.2. The capillary extrusions are carried out at constant velocity using 200 N load cell and pre-force is kept at 0.1 N.

UV-Vis Spectroscopy

The absorption spectrums are recorded using a UV-Vis Cary 3500 (*Agilent*) spectrophotometer by scanning from 200 nm to 800 nm. The samples are placed in quartz cuvettes with a path length of 1 cm. The measurements are carried out at 25 °C. The reference solvent is the solvent of the analyzed sample.

UV Curing

A hand-held lamp is used including a replacement tube UV light (Carl Roth, 365 nm, 6 W, 16 mm x 210 mm (diameter x length). Ru-initiated photocrosslinking is performed by *UV LED Solo P* (Opsytec Dr. Gröbel GmbH) point light source at the wavelengths of 405 nm. The spectroradiometer of *UVpad E* (Opsytec Dr. Gröbel GmbH) is used to measure the spectrum of the used light sources. During the measurement, the spectrum is shown on the graphic display and the irradiances for UVA, UVB, UVC and VIS are recorded. *UV-LED CHAMBER BSL-02* (Opsytec Dr. Gröbel GmbH) is used for UV irradiation of photo linkers and their hydrogels. The irradiance and time are monitored by integrating the UV-MAT Touch and UV-MAT.

Extrusion-based 3D Printing

The printing experiments are done with a extrusion-based 3D printing system (Bio V1 by Regemat 3D). It is equipped with a print head and light sources. The configuration of the printing head and the wide range of movements in *x-*, *y-* and *z*-direction allow a precise adjustment that allows the system to print

on different surfaces. The modular extrusion head is configured with different interchangeable extrusion tools. The printing head is also configured with four different tools with adjustment movement in the *x*- and *y*-direction. Two light sources are available for curing at 365 nm, and 405 nm. The software *Regemat3D Designer* is provided by the company Regemat 3D. STL file format and designing the self-made models via G-Code is suitable to manage manufacturing parameters. Before the process, syringe-needle system is prepared by following a standard calibration. 5 mL transparent piston including *Regemat* polyethylene and polypropylene syringe is used. The eextrusions of the inks are performed at room temperature.

Multi-photon Lithography

Subtractive photopatterning of swollen hydrogels is performed by multi-photon lithography by means of a 3D Printer by LightFab GmbH, Aachen. The device consists of a high dynamic 3D micro scanner with a high precision 3-axis system for stepping, a fiber chirped pulse amplification (FCPA) laser (Satsuma, Amplitude Systemes, Pessac, France), camera, vision system in automatic alignment, and CAD/CAM/nc software. The photodegradable hydrogels are exposed to pulse energies from 150 nJ to 40 nJ. With pulse duration adjusted at 500 fs, the repetition rate varied by 1.5 MHz and 10 MHz at a wavelength of 1030 nm. The laser radiation is focused inside hydrogels using the laser beam by means of a 20 x / 0.4 objective providing a focal diameter of approximately 2 µm. The writing speed was set to the maximum of 200 mm s^{-1} that the machine can provide with the given microscope objective. The distance between two layers in the *z*- directio*n* is set to 3 µm, while the line distance in *x*- and *y*-coordinates is 2 µm. The polarization of the laser radiation is circular and thus independent from the writing direction of the laser-induced structures.

6.3   Syntheses

Synthesis of PCL-PEG-PCL triblock copolymers

The monomer ε-CL distilled from CaH_2 is used in the reactions and stored over a molecular sieve before use. The synthesis of triblock copolymers is started with an azeotropic distillation of toluene-based solutions of the macro initiators of PEG_{8K}, PEG_{35K}, and PEG_{100K}. The used reactants of ε-CL and PEG diols are calculated according to yielding in 10 g products.

Table 6.1. Reactants for the synthesis of PCL-PEG-PCL triblock copolymers

Triblock copolymer	n_{CL} mmol	n_{PEG} mmol	m_{PEG} g	V_{CL} mL	m_{CL} g	m_{total} g	yield %
$C_1E_8C_1$	17.698	1.01	8.1	1.875	1.9	10.0	44.6
$C_3E_8C_3$	4.753	0.27	9.5	0.504	0.5	10.0	86.7
$C_5E_8C_5$	1.722	0.10	9.8	0.182	0.2	10.0	83.3
$C_1E_{35}C_1$	38.816	0.74	5.9	4.112	4.2	10.0	84.3
$C_3E_{35}C_3$	12.994	0.25	8.6	1.376	1.4	10.0	41.1
$C_5E_{35}C_5$	4.995	0.09	9.5	0.529	0.5	10.0	58.9
$C_1E_{100}C_1$	49.842	0.57	4.6	5.280	5.4	10.0	81.5
$C_3E_{100}C_3$	19.626	0.22	7.9	2.079	2.1	10.0	92.6
$C_5E_{100}C_5$	7.980	0.09	9.1	0.845	0.9	10.0	92.1

The PCL-PEG-PCL triblock copolymers are synthesized in 40 mL of azeotropically distilled toluene by coordination-inserted ROP of ε-CL initiated by PEG diols using 0.29 mmol of Bu_2SnO as a catalyst. The calculated amounts of ε-CL and PEG are contained under a nitrogen atmosphere at 130 °C for five hours. After that, the final solutions are cooled to room temperature. By adding enough chloroform, the viscous reaction solutions are diluted. The resulting products are precipitated drop by drop in excess ice-cold petroleum ether 40/60. The white powder products are obtained and dried at 35 °C under a vacuum overnight.

Purification of triblock copolymers

The triblock copolymers are purified at 10 % w/v concentration in 2 mL of toluene. An ultrasonic bath is used to increase the dissolution rate at room temperature. Each sample is treated by centrifugation until a clear supernatant is obtained over precipitation. The soluble fraction is transferred into a tared vial, and the insoluble fraction remains in the tared centrifugation tubes. Both fractions are weighed to calculate their mass fraction after being dried at 35 °C under vacuum.

Synthesis of PEG$_{8K}$DMA

The synthesis of PEG$_{8K}$DMA is performed as described in the literature [167]. Firstly, an azeotropic distillation is started using excess DCM at 60-70 $^{\circ}$C using Schlenk and a vacuum line. The distillation is performed until the PEG/DCM (w/v) ratio is approx. 1:2. After distillation, the system cools down to RT, and TEA is added (2.2:1) to the reaction vessel under Argon. Adding MAc to PEG solution slowly (4:1), the solution looks white-off. The reaction is conducted for at least 24 hours under protection from light.

The functionalization process is controlled via ^{1}H-NMR, by taking a sample from the reaction system. Following the spectroscopic data evaluation, the excess of MAc and TEA are added into the reaction vessel at the same ratio according to the functionalization degree of PEG$_{8K}$. After the functionalization reaches the desired value, the reaction solution is transferred into 1.5 M K$_2$CO$_3$ solution in the separatory funnel. The mixture is shaken vigorously for a few seconds and vented to the funnel to release CO$_2$. It is repeated until no more gas is released. The solution becomes a milky white colour. The mixture should be separated into two phases in the separation funnel. The organic phase containing the functionalized PEG$_{8K}$DMA is moved to the bottom as a denser phase. The top phase is aqueous (transparent), and the interphase is white. The organic phase is dried with anhydrous MgSO$_4$ until the mixture is clear.

It is precipitated in excess ice-cold diethyl ether. PEG$_{8K}$DMA is filtered as a white powder. The obtained product is dried under a vacuum at 35 $^{\circ}$C. It is stored at -20 $^{\circ}$C and defrosted prior to use. The product can be successfully obtained with a degree functionalization of $f > 90\%$ above the yield of 80 %.

Preparation of binary solutions

PEG-based polymer solutions are prepared in deionized water. PEG$_{8K}$DMA is synthesized at a high functionalization degree of ≥ 90, and PEG$_{100K}$ (*PDI* = 1.81) is commercially purchased. The miscible binary polymer solutions are prepared at different mass fractions at room temperature. The mass fraction ratios of PEG$_{8K}$DMA to PEG$_{100K}$ (PEG$_{8K}$DMA/PEG$_{100K}$) are varied. 10/0, 10/1, 10/3.5, and 10/5 are categorized as BS$_{10}$. 20/0, 20/1, 20/3.5, 20/5, 20/10 and 20/20 are categorized as BS$_{20}$. For the homo solutions of PEG$_{100K}$, for instance, their solutions are shown as , 0/1, 0/3.5, 0/5, and 0/10.

Table 6.2. The mass composition of PEG-based solutions.

Solution (ink)	PEG$_{8K}$DMA/ PEG$_{100K}$	m_{DMA} mg	m_{100K} mg	m_{water} mg
PEG$_{100K}$	0/0.5	0	0.5	995
	0/1	0	1	990
	0/1.5	0	1.5	985
	0/2	0	2	980
	0/2.5	0	2.5	975
	0/3	0	3	970
	0/4	0	4	960
	0/5	0	5	950
	0/10	0	10	900
	0/15	0	15	850
	0/20	0	20	800
	0/25	0	25	750
	0/30	0	30	700
	0/35	0	35	650
PEG$_{8K}$DMA	5/0	50	0	950
	10/0	100	0	900
	20/0	200	0	800
BS$_{10}$	10/1	100	10	890
	10/3.5	100	35	865
	10/5	100	50	850
BS$_{20}$	20/1	200	10	790
	20/3.5	200	35	765
	20/5	200	50	750
	20/10	200	100	700
	20/20	200	200	600

Synthesis of the Ru-initiated hydrogels

For the Ru-initiated hydrogels, PEG$_{8K}$DMA and PEG$_{100K}$ is dissolved in water as explained preparation of binary solutions, according to the mass fractions for both components. Stock solutions of Ru prepared at 50 mM and 5 mM, and APS stock solution is prepared at 500 mM (Table 6.3). The stock solutions of Ru are treated by the ultrasonic bath for a few minutes before adding into binary solutions. In general, Stock ruthenium solutions and stock solutions of APS are added to 1 g of PEG-based polymer solutions at the calculated amounts. Then, 300 µl of the precursor solutions are transferred into the Teflon molds (12 mm x 2 mm) to be irradiated by the point light source at 405 nm, at the distance of 1 cm. After photopolymerization, the hydrogels are put into water to test swelling by weighing of gel samples.

The water is replaced regularly for 2 days. The swollen samples are dried at 35 °C under vacuum.

Table 6.3. Formulation of precursor polymer solution for Ru-initiated photopolymerization

PEG$_{8K}$DMA	PEG$_{100K}$	Water	Ru$_{stock}$		APS$_{stock}$	
mg	mg	mg	mM	μL	mM	μL
200	0	800	50	10	500	80
200	0	800	50	40	500	200
200	0	800	50	40	500	400
200	0	800	50	80	500	400
200	0	800	50	200	500	40
200	0	800	50	40	500	400
200	10	790	50	40	500	400
200	35	765	50	40	500	400
200	50	750	50	40	500	400
200	0	800	5	20	500	400
200	10	790	5	20	500	400
200	35	765	5	20	500	400
200	50	750	5	20	500	400

Synthesis of poly(AAm-co-MBAA) hydrogels

The stock solutions of AAm, MBAA, NaH$_2$PO$_4$, APS and TEMED are freshly prepared with deionized water. The volume percentage of the used stock solution for a desired gel preparation is shown in Table 6.4. AAm is dissolved in water, and then stock solutions of MBAA, NaH$_2$PO$_4$, APS and TEMED are added, respectively. The prepared final solutions are transferred into the circle shape of Teflon molds (20 mm x 2 mm), and the molds is covered with petri dishes. The polymerization is performed for 1 hour. After polymerization, samples of hydrogel were put into water to test swelling by weighing of gel samples. The water is replaced regularly for at least 2 days. The swollen samples are dried at 35 °C under vacuum.

Table 6.4. The volume composition (% v/v) of stock solutions for the synthesis of Poly(AAm-co-MBAA) hydrogels

α	AAm (40 % w/v)	MBAA (2 % w/v)	NaH$_2$PO$_4$ (1.5 M)	APS (0.4 M)	TEMED (0.16 M)	Water
0.0090	37.5	15	1	4	4	38.5
0.0060	37.5	10	1	4	4	43.5
0.0045	37.5	7.5	1	4	4	46
0.0030	37.5	5	1	4	4	48.5
0.0015	37.5	2.5	1	4	4	51

Synthesis of poly(AAm-co-PL$_{est}$) and poly(Aam-co-PL$_{carb}$) hydrogels

The stock solutions of PL$_{est}$ and PL$_{carb}$ are prepared at different concentration as seen in

Table 6.5. According to desired crosslinker content. The stock solutions of AAm, NaH$_2$PO$_4$, APS and TEMED are freshly prepared (Table 6.4) with deionized water. AAm is dissolved in water, and then stock solutions of MBAA, NaH$_2$PO$_4$, APS and TEMED, according to the final volume ratio are added, respectively. The prepared solutions are transferred into the circle shape of Teflon molds (20 mm x 2 mm), and the molds is covered with petri dishes. The polymerization is performed for 1 hour. After polymerization, samples of hydrogel were put into water to test swelling by weighing of gel samples. The water is replaced regularly for at least 2 days. The swollen samples are dried at 35 °C under vacuum.

Table 6.5. The concentration of PL$_{est}$ and PL$_{carb}$ stock solution according to the desired hydrogels

α	c / mol L^{-1}
0.00075	0.41 x 10^{-2}
0.0015	0.82 x 10^{-2}
0.0030	1.65 x 10^{-2}
0.0045	2.49 x 10^{-2}
0.0060	3.30 x 10^{-2}
0.0075	4.14 x 10^{-2}
0.0090	4.98 x 10^{-2}

The stock solutions of AAm (40% (w/v)), NaH$_2$PO$_4$ (1.5 M), APS (0.4 M) and TEMED (0.16 M) are freshly prepared with deionized water. PL-based hydrogels of the volume composition of the used stock solutions for a desired gel preparation is shown in Table 6.6.

Table 6.6. The volume composition (% v/v) of stock solutions

AAm (40 % w/v)	Photo linker	NaH$_2$PO$_4$ (1.5 M)	APS (0.4 M)	TEMED (0.16 M)	Water
37.5%	38.5%	1%	4%	4%	15%

Staining test

100 mg of 2,4-Dinitrophenylhydrazine is dissolved in. 20 mL of concentrated HCl. The vascularized hydrogels put into 8-10 mL of the stock solution in a petri dish. After 30 mins, the images are taken under a microscope.

Synthesis of photodegradable dimethacrylated PEG-macro crosslinker (PL$_{PEG}$)

A NB-based moiety based on its proven photolytic efficiency is synthesized to create a photodegradable macromer according to the literature.[125] The synthesis of photodegradable macro crosslinker begins with synthesis of photodegradable moiety. It is suspended 1.22 mmol of 4-(4-(1-hydroxyethyl)-2-methoxy-5-nitrophenoxy) butanoic acid in 11 mL of DCM under argon atmosphere in a light-prevented flask. 3.71 mmol of TEA is added into a well-dispersed mixture and stirred inside an ice bath for 20 min resulting in a color change from opaque pale yellow to transparent yellow. Then 5 mmol of methacryloyl chloride is dispersed in 2.6 mL of DCM, afterwards slowly added into the solution. After removing the ice bath, the reaction solution is left stirring for 72 hours at room temperature. To remove impurities and the unreacted reagents, the reaction solution is washed with 1.5 mL (5 % w/v) sodium bicarbonate solution, 1.5 mL of diluted HCl (1 % v/v) and 1.5 mL of water. After observing the phase separation in the separatory funnel, DCM is evaporated from the organic phase. With the addition of 20 ml of H$_2$O/acetone (1:1) mixture, the product is left for stirring again at room temperature for overnight. Finally, the solution is filtered with 25 mL of DCM and subsequently washed with 1.5 mL of diluted HCl (1 % v/v) and 1.5 mL of water. The extracted phase is dried of magnesium sulfate and evaporated with rotavapor. A yellow oily product is obtained as a photodegradable moiety yield at 64 %.

0.27 mmol of the synthesized precursor is dissolved in 954 µL of N-methyl-2-pyrolidon (NMP) under Ar atmosphere. 0.29 mmol of the coupling agent HBTU and 0.36 mmol of HOBt are dissolved in 1.91 mL of N-methyl-2-pyrolidon and added dropwise into the precursor solution. It is followed by the addition of 0.52 mmol of N,N-Diisopropylethylamine (DIEA). 0.03 mmol of poly(ethylene glycol) diamine dissolved in 0.954 mL of NMP is added to the reaction solution. With the adding 1 mL of N-methyl-2-pyrolidon, the prepared reaction solution is left for 48 hours at room temperature protected from light. The white sticky crude product is precipitated the ice-cold diethyl ether. Diethyl ether is decanted after centrifugation, the product was dried at 35°C at 50 mbar. As the result, a yellow viscous oily photodegradable crosslinker is achieved with the yield of 35.7 %. The functionality is calculated, f = 74%.

7 REFERENCES

(1) Peppas, N. A.; Hoffman, A. S. Hydrogels. *Biomater. Sci.* **2020**, No. 1, 153–166. https://doi.org/10.1016/B978-0-12-816137-1.00014-3.

(2) Lanza, R.; Langer, R.; Vacanti, J.; Atala, A.; Eds. *Principles of Tissue Engineering*; Academic Press, 2020. https://doi.org/10.1016/B978-0-12-818422-6.00089-7.

(3) Liu, J.; Zheng, H.; Poh, P. S. P.; Machens, H. G.; Schilling, A. F. Hydrogels for Engineering of Perfusable Vascular Networks. *Int. J. Mol. Sci.* **2015**, *16* (7), 15997–16016. https://doi.org/10.3390/ijms160715997.

(4) Kisiday, J.; Jin, M.; Kurz, B.; Hung, H.; Semino, C.; Zhang, S.; Grodzinsky, A. J. Self-Assembling Peptide Hydrogel Fosters Chondrocyte Extracellular Matrix Production and Cell Division: Implications for Cartilage Tissue Repair. *Proc. Natl. Acad. Sci. U. S. A.* **2002**, *99* (15), 9996–10001. https://doi.org/10.1073/pnas.142309999.

(5) Zhu, J. Bioactive Modification of Poly(Ethylene Glycol) Hydrogels for Tissue Engineering. *Biomaterials* **2010**, *31* (17), 4639–4656. https://doi.org/10.1016/j.biomaterials.2010.02.044.

(6) Arda, K.; Ciledag, N.; Aktas, E.; Aribas, B. K.; Köse, K. Quantitative Assessment of Normal Soft-Tissue Elasticity Using Shear-Wave Ultrasound Elastography. *Am. J. Roentgenol.* **2011**, *197* (3), 532–536. https://doi.org/10.2214/AJR.10.5449.

(7) Achterberg, V. F.; Buscemi, L.; Diekmann, H.; Smith-Clerc, J.; Schwengler, H.; Meister, J. J.; Wenck, H.; Gallinat, S.; Hinz, B. The Nano-Scale Mechanical Properties of the Extracellular Matrix Regulate Dermal Fibroblast Function. *J. Invest. Dermatol.* **2014**, *134* (7), 1862–1872. https://doi.org/10.1038/jid.2014.90.

(8) Engler, A. J.; Sen, S.; Sweeney, H. L.; Discher, D. E. Matrix Elasticity Directs Stem Cell Lineage Specification. *Cell* **2006**, *126* (4), 677–689. https://doi.org/10.1016/j.cell.2006.06.044.

(9) Pereira, R. F.; Bártolo, P. J. 3D Photo-Fabrication for Tissue Engineering and Drug Delivery. *Engineering* **2015**, *1* (1), 090–112. https://doi.org/10.15302/J-ENG-2015015.

(10) Bagheri, A.; Jin, J. Photopolymerization in 3D Printing. *ACS Appl. Polym. Mater.* **2019**, *1* (4), 593–611. https://doi.org/10.1021/acsapm.8b00165.

(11) Mondschein, R. J.; Kanitkar, A.; Williams, C. B.; Verbridge, S. S.; Long, T. E. Polymer Structure-

Property Requirements for Stereolithographic 3D Printing of Soft Tissue Engineering Scaffolds. *Biomaterials* **2017**, *140*, 170–188. https://doi.org/10.1016/j.biomaterials.2017.06.005.

(12)   Lutolf, M. P. Biomaterials: Spotlight on Hydrogels. *Nat. Mater.* **2009**, *8* (6), 451–453. https://doi.org/10.1038/nmat2458.

(13)   Bryant, S. J.; Bender, R. J.; Durand, K. L.; Anseth, K. S. Encapsulating Chondrocytes in Degrading PEG Hydrogels with High Modulus: Engineering Gel Structural Changes to Facilitate Cartilaginous Tissue Production. *Biotechnol. Bioeng.* **2004**, *86* (7), 747–755. https://doi.org/10.1002/bit.20160.

(14)   Mezger, T. *The Rheology Handbook: For Users of Rotational and Oscillatory Rheometers*; Vincentz Network, 2020. https://doi.org/10.1515/9783748603702.

(15)   Ebagninin, K. W.; Benchabane, A.; Bekkour, K. Rheological Characterization of Poly(Ethylene Oxide) Solutions of Different Molecular Weights. *J. Colloid Interface Sci.* **2009**, *336* (1), 360–367. https://doi.org/10.1016/j.jcis.2009.03.014.

(16)   Ergungor, Z.; Smolinski, J. M.; Manke, C. W.; Gulari, E. Effect of Polymer-Surfactant Interactions on Elongational Viscosity and Atomization of Peo Solutions. *J. Nonnewton. Fluid Mech.* **2006**, *138* (1), 1–6. https://doi.org/10.1016/j.jnnfm.2006.03.014.

(17)   Whitby, C. P.; Scales, P. J.; Grieser, F.; Healy, T. W.; Kirby, G.; Lewis, J. A.; Zukoski, C. F. PAA/PEO Comb Polymer Effects on Rheological Properties and Interparticle Forces in Aqueous Silica Suspensions. *J. Colloid Interface Sci.* **2003**, *262* (1), 274–281. https://doi.org/10.1016/S0021-9797(03)00179-6.

(18)   Lacroix, C.; Grmela, M.; Carreau, P. J. Relationships between Rheology and Morphology for Immiscible Molten Blends of Polypropylene and Ethylene Copolymers under Shear Flow. *J. Rheol. (N. Y. N. Y).* **1998**, *42* (1), 41–62. https://doi.org/10.1122/1.550943.

(19)   Ferry, J. D. *Viscoelastic Properties of Polymers*; John Wiley & Sons, 1980. https://doi.org/10.1149/1.2428174.

(20)   Macosco, C. W. *Principles, Measurements and Applications*; VCH Publishes, 1994; Vol. 86.

(21)   Gross, B.; Ferry, J. D. Mathematical Structure of the Theories of Viscoelasticity. *Phys. Today* **1955**, *8* (4), 17–18. https://doi.org/10.1063/1.3061982.

(22)   Barnes, H. A. *A Handbook of Elementary Rheology*; Polymer Composites, 2000; Vol. 6.

(23)   Li, S. P.; Zhao, G.; Chen, H. Y. The Relationship between Steady Shear Viscosity and Complex

Viscosity. *J. Dispers. Sci. Technol.* **2005**, *26* (4), 415–419. https://doi.org/10.1081/DIS-200054555.

(24) Cox, W. P.; Merz, E. H. Correlation of Dynamic and Steady Flow Viscosities. *J. Polym. Sci.* **1958**, *28* (118), 619–622. https://doi.org/10.1002/pol.1958.1202811812.

(25) Winter, H. H. Three Views of Viscoelasticity for Cox-Merz Materials. *Rheol. Acta* **2009**, *48* (3), 241–243. https://doi.org/10.1007/s00397-008-0329-5.

(26) Morris, B. A. Rheology of Polymer Melts. *Sci. Technol. Flex. Packag.* **2017**, 121–147. https://doi.org/10.1016/b978-0-323-24273-8.00005-8.

(27) Syrjälä, S.; Aho, J. Capillary Rheometry of Polymer Melts - Simulation and Experiment. *Korea Aust. Rheol. J.* **2012**, *24* (3), 241–247. https://doi.org/10.1007/s13367-012-0029-7.

(28) Mooney, M.; Black, S. A. A Generalized Fluidity Power Law and Laws of Extrusion. *Rubber Chem. Technol.* **1953**, *26* (2), 311–322. https://doi.org/10.5254/1.3539817.

(29) Rabinowitsch, B. Über Die Viskosität Und Elastizität von Solen. *Zeitschrift für Phys. Chemie* **1929**, *145A* (1), 1–26. https://doi.org/10.1515/zpch-1929-14502.

(30) Porter, R. S.; Johnson, J. F. The Entanglement Concept in Polymer Systems. *Chem. Rev.* **1966**, *66* (1), 1–27. https://doi.org/10.1021/cr60239a001.

(31) Kol, R.; Nachtergaele, P.; De Somer, T.; D'Hooge, D. R.; Achilias, D. S.; De Meester, S. Toward More Universal Prediction of Polymer Solution Viscosity for Solvent-Based Recycling. *Ind. Eng. Chem. Res.* **2022**, *61* (30), 10999–11011. https://doi.org/10.1021/acs.iecr.2c01487.

(32) Cross, M. M. Rheology of Non-Newtonian Fluids: A New Flow Equation for Pseudoplastic Systems. *J. Colloid Sci.* **1965**, *20* (5), 417–437. https://doi.org/10.1016/0095-8522(65)90022-X.

(33) Liang, J. Z.; Zhong, L. Characterization of Elongation Viscosity for Polyethylene Melts. *Colloid Polym. Sci.* **2013**, *291* (7), 1595–1599. https://doi.org/10.1007/s00396-013-2893-1.

(34) Karakutuk, I.; Ak, F.; Okay, O. Diepoxide-Triggered Conformational Transition of Silk Fibroin: Formation of Hydrogels. *Biomacromolecules* **2012**, *13* (4), 1122–1128. https://doi.org/10.1021/bm300006r.

(35) Brown, T. E.; Carberry, B. J.; Worrell, B. T.; Dudaryeva, O. Y.; McBride, M. K.; Bowman, C. N.; Anseth, K. S. Photopolymerized Dynamic Hydrogels with Tunable Viscoelastic Properties through Thioester Exchange. *Biomaterials* **2018**, *178*, 496–503. https://doi.org/10.1016/j.biomaterials.2018.03.060.

(36) Zhou, Y.; Zhao, S.; Zhang, C.; Liang, K.; Li, J.; Yang, H.; Gu, S.; Bai, Z.; Ye, D.; Xu, W. Photopolymerized Maleilated Chitosan/Thiol-Terminated Poly (Vinyl Alcohol) Hydrogels as Potential Tissue Engineering Scaffolds. *Carbohydr. Polym.* **2018**, *184*, 383–389. https://doi.org/10.1016/j.carbpol.2018.01.009.

(37) Tong, X.; Du, L.; Xu, Q. Tough, Adhesive and Self-Healing Conductive 3D Network Hydrogel of Physically Linked Functionalized-Boron Nitride/Clay /Poly(N-Isopropylacrylamide). *J. Mater. Chem. A* **2018**, *6* (7), 3091–3099. https://doi.org/10.1039/c7ta10898b.

(38) Wang, Y. J.; Zhang, X. N.; Song, Y.; Zhao, Y.; Chen, L.; Su, F.; Li, L.; Wu, Z. L.; Zheng, Q. Ultrastiff and Tough Supramolecular Hydrogels with a Dense and Robust Hydrogen Bond Network. *Chem. Mater.* **2019**, *31* (4), 1430–1440. https://doi.org/10.1021/acs.chemmater.8b05262.

(39) Shao, C.; Chang, H.; Wang, M.; Xu, F.; Yang, J. High-Strength, Tough, and Self-Healing Nanocomposite Physical Hydrogels Based on the Synergistic Effects of Dynamic Hydrogen Bond and Dual Coordination Bonds. *ACS Appl. Mater. Interfaces* **2017**, *9* (34), 28305–28318. https://doi.org/10.1021/acsami.7b09614.

(40) Liang, Y.; Xue, J.; Du, B.; Nie, J. Ultrastiff, Tough, and Healable Ionic-Hydrogen Bond Cross-Linked Hydrogels and Their Uses as Building Blocks to Construct Complex Hydrogel Structures. *ACS Appl. Mater. Interfaces* **2019**, *11* (5), 5441–5454. https://doi.org/10.1021/acsami.8b20520.

(41) Lin, Y.; Zhang, H.; Liao, H.; Zhao, Y.; Li, K. A Physically Crosslinked, Self-Healing Hydrogel Electrolyte for Nano-Wire PANI Flexible Supercapacitors. *Chem. Eng. J.* **2019**, *367*, 139–148. https://doi.org/10.1016/j.cej.2019.02.064.

(42) Deng, Y.; Hussain, I.; Kang, M.; Li, K.; Yao, F.; Liu, S.; Fu, G. Self-Recoverable and Mechanical-Reinforced Hydrogel Based on Hydrophobic Interaction with Self-Healable and Conductive Properties. *Chem. Eng. J.* **2018**, *353*, 900–910. https://doi.org/10.1016/j.cej.2018.07.187.

(43) Hennink, W. E.; van Nostrum, C. F. Novel Crosslinking Methods to Design Hydrogels. *Adv. Drug Deliv. Rev.* **2012**, *64*, 223–236. https://doi.org/10.1016/j.addr.2012.09.009.

(44) Stojkov, G.; Niyazov, Z.; Picchioni, F.; Bose, R. K. Relationship between Structure and Rheology of Hydrogels for Various Applications. *Gels* **2021**, *7* (4), 255. https://doi.org/10.3390/gels7040255.

(45) Chang, B.; Ahuja, N.; Ma, C.; Liu, X. Injectable Scaffolds: Preparation and Application in Dental and Craniofacial Regeneration. *Materials Science and Engineering R: Reports*. 2017, pp 1–26. https://doi.org/10.1016/j.mser.2016.11.001.

(46) Chimene, D.; Kaunas, R.; Gaharwar, A. K. Hydrogel Bioink Reinforcement for Additive Manufacturing: A Focused Review of Emerging Strategies. *Adv. Mater.* **2020**, *32* (1), 1–22. https://doi.org/10.1002/adma.201902026.

(47) Thakur, T.; Xavier, J. R.; Cross, L.; Jaiswal, M. K.; Mondragon, E.; Kaunas, R.; Gaharwar, A. K. Photocrosslinkable and Elastomeric Hydrogels for Bone Regeneration. *J. Biomed. Mater. Res. - Part A* **2016**, *104* (4), 879–888. https://doi.org/10.1002/jbm.a.35621.

(48) Malda, J.; Visser, J.; Melchels, F. P.; Jüngst, T.; Hennink, W. E.; Dhert, W. J. A.; Groll, J.; Hutmacher, D. W. 25th Anniversary Article: Engineering Hydrogels for Biofabrication. *Adv. Mater.* **2013**, *25* (36), 5011–5028. https://doi.org/10.1002/adma.201302042.

(49) Bae, S. J.; Joo, M. K.; Jeong, Y.; Kim, S. W.; Lee, W. K.; Sohn, Y. S.; Jeong, B. Gelation Behavior of Poly(Ethylene Glycol) and Polycaprolactone Triblock and Multiblock Copolymer Aqueous Solutions. *Macromolecules* **2006**, *39* (14), 4873–4879. https://doi.org/10.1021/ma060153s.

(50) Regalado, E. J.; Selb, J.; Candau, F. Viscoelastic Behavior of Semidilute Solutions of Multisticker Polymer Chains. *Macromolecules* **1999**, *32* (25), 8580–8588. https://doi.org/10.1021/ma990999e.

(51) Escobar-Chávez, J. J.; López-Cervantes, M.; Naïk, A.; Kalia, Y. N.; Quintanar-Guerrero, D.; Ganem-Quintanar, A. Applications of Thermo-Reversible Pluronic F-127 Gels in Pharmaceutical Formulations. *J. Pharm. Pharm. Sci.* **2006**, *9* (3), 339–358.

(52) Séréro, Y.; Aznar, R.; Porte, G.; Berret, J. F.; Calvet, D.; Collet, A.; Viguier, M. Associating Polymers: From "Flowers" to Transient Networks. *Phys. Rev. Lett.* **1998**, *81* (25), 5584–5587. https://doi.org/10.1103/PhysRevLett.81.5584.

(53) Yu, L.; Zhang, H.; Ding, J. A Subtle End-Group Effect on Macroscopic Physical Gelation of Triblock Copolymer Aqueous Solutions. *Angew. Chemie Int. Ed.* **2006**, *45* (14), 2232–2235. https://doi.org/10.1002/anie.200503575.

(54) Nakaya–Yaegashi, K.; Ramos, L.; Tabuteau, H.; Ligoure, C. Linear Viscoelasticity of Entangled Wormlike Micelles Bridged by Telechelic Polymers: An Experimental Model for a Double Transient Network. *J. Rheol. (N. Y. N. Y).* **2008**, *52* (2), 359–377. https://doi.org/10.1122/1.2828645.

(55) Schmaljohann, D. Thermo- and PH-Responsive Polymers in Drug Delivery. *Adv. Drug Deliv. Rev.* **2006**, *58* (15), 1655–1670. https://doi.org/10.1016/j.addr.2006.09.020.

(56) Lowman, A. M.; Peppas, N. A. Analysis of the Complexation/Decomplexation Phenomena in

Graft Copolymer Networks. *Macromolecules* **1997**, *30* (17), 4959–4965. https://doi.org/10.1021/ma970399k.

(57)   Sperling, L. H. Interpenetrating Polymer Networks: An Overview; Advances in Chemistry, 1994; pp 3–38. https://doi.org/10.1021/ba-1994-0239.ch001.

(58)   Lohani, A.; Singh, G.; Bhattacharya, S. S.; Verma, A. Interpenetrating Polymer Networks as Innovative Drug Delivery Systems. *J. Drug Deliv.* **2014**, *2014*, 1–11. https://doi.org/10.1155/2014/583612.

(59)   James, J.; Thomas, G. V.; Akhina, H.; Thomas, S. Micro- and Nano-Structured Interpenetrating Polymer Networks: State of the Art, New Challenges, and Opportunities. In *Micro- and Nano-Structured Interpenetrating Polymer Networks: From Design to Applications*; Wiley, 2016; pp 1–27. https://doi.org/10.1002/9781119138945.ch1.

(60)   Zoratto, N.; Matricardi, P. Semi-IPNs and IPN-Based Hydrogels. *Polym. Gels* **2018**, 91–124. https://doi.org/10.1016/b978-0-08-102179-8.00004-1.

(61)   Yang, C.; Wang, X.; Yao, X.; Zhang, Y.; Wu, W.; Jiang, X. Hyaluronic Acid Nanogels with Enzyme-Sensitive Cross-Linking Group for Drug Delivery. *J. Control. Release* **2015**, *205*, 206–217. https://doi.org/10.1016/j.jconrel.2015.02.008.

(62)   Yue, K.; Trujillo-de Santiago, G.; Alvarez, M. M.; Tamayol, A.; Annabi, N.; Khademhosseini, A. Synthesis, Properties, and Biomedical Applications of Gelatin Methacryloyl (GelMA) Hydrogels. *Biomaterials* **2015**, *73*, 254–271. https://doi.org/10.1016/j.biomaterials.2015.08.045.

(63)   Nguyen, Q. T.; Hwang, Y.; Chen, A. C.; Varghese, S.; Sah, R. L. Cartilage-like Mechanical Properties of Poly (Ethylene Glycol)-Diacrylate Hydrogels. *Biomaterials* **2012**, *33* (28), 6682–6690. https://doi.org/10.1016/j.biomaterials.2012.06.005.

(64)   Choi, J. R.; Yong, K. W.; Choi, J. Y.; Cowie, A. C. Recent Advances in Photo-Crosslinkable Hydrogels for Biomedical Applications. *Biotechniques* **2019**, *66* (1), 40–53. https://doi.org/10.2144/btn-2018-0083.

(65)   Aycan, D.; Alemdar, N. Development of PH-Responsive Chitosan-Based Hydrogel Modified with Bone Ash for Controlled Release of Amoxicillin. *Carbohydr. Polym.* **2018**, *184*, 401–407. https://doi.org/10.1016/j.carbpol.2017.12.023.

(66)   Liu, S.; Yeo, D. C.; Wiraja, C.; Tey, H. L.; Mrksich, M.; Xu, C. Peptide Delivery with Poly(Ethylene Glycol) Diacrylate Microneedles through Swelling Effect. *Bioeng. Transl. Med.* **2017**, *2* (3), 258–267. https://doi.org/10.1002/btm2.10070.

(67)   Lim, W. S.; Chen, K.; Chong, T. W.; Xiong, G. M.; Birch, W. R.; Pan, J.; Lee, B. H.; Er, P. S.; Salvekar, A. V.; Venkatraman, S. S.; Huang, Y. A Bilayer Swellable Drug-Eluting Ureteric Stent: Localized Drug Delivery to Treat Urothelial Diseases. *Biomaterials* **2018**, *165*, 25–38. https://doi.org/10.1016/j.biomaterials.2018.02.035.

(68)   Schesny, M. K.; Monaghan, M.; Bindermann, A. H.; Freund, D.; Seifert, M.; Eble, J. A.; Vogel, S.; Gawaz, M. P.; Hinderer, S.; Schenke-Layland, K. Preserved Bioactivity and Tunable Release of a SDF1-GPVI Bi-Specific Protein Using Photo-Crosslinked PEGda Hydrogels. *Biomaterials* **2014**, *35* (25), 7180–7187. https://doi.org/10.1016/j.biomaterials.2014.04.116.

(69)   Jabbari, E.; Sarvestani, S. K.; Daneshian, L.; Moeinzadeh, S. Optimum 3D Matrix Stiffness for Maintenance of Cancer Stem Cells Is Dependent on Tissue Origin of Cancer Cells. *PLoS One* **2015**, *10* (7), e0132377. https://doi.org/10.1371/journal.pone.0132377.

(70)   Tian, F.; Lyu, J.; Shi, J.; Tan, F.; Yang, M. A Polymeric Microfluidic Device Integrated with Nanoporous Alumina Membranes for Simultaneous Detection of Multiple Foodborne Pathogens. *Sensors Actuators, B Chem.* **2016**, *225*, 312–318. https://doi.org/10.1016/j.snb.2015.11.059.

(71)   Athirasala, A.; Lins, F.; Tahayeri, A.; Hinds, M.; Smith, A. J.; Sedgley, C.; Ferracane, J.; Bertassoni, L. E. A Novel Strategy to Engineer Pre-Vascularized Full-Length Dental Pulp-like Tissue Constructs. *Sci. Rep.* **2017**, *7* (1), 3323. https://doi.org/10.1038/s41598-017-02532-3.

(72)   Levato, R.; Webb, W. R.; Otto, I. A.; Mensinga, A.; Zhang, Y.; van Rijen, M.; van Weeren, R.; Khan, I. M.; Malda, J. The Bio in the Ink: Cartilage Regeneration with Bioprintable Hydrogels and Articular Cartilage-Derived Progenitor Cells. *Acta Biomater.* **2017**, *61*, 41–53. https://doi.org/10.1016/j.actbio.2017.08.005.

(73)   Fan, L.; Liu, C.; Chen, X.; Zou, Y.; Zhou, Z.; Lin, C.; Tan, G.; Zhou, L.; Ning, C.; Wang, Q. Directing Induced Pluripotent Stem Cell Derived Neural Stem Cell Fate with a Three-Dimensional Biomimetic Hydrogel for Spinal Cord Injury Repair. *ACS Appl. Mater. Interfaces* **2018**, *10* (21). https://doi.org/10.1021/acsami.8b05293.

(74)   Sadeghi, A. H.; Shin, S. R.; Deddens, J. C.; Fratta, G.; Mandla, S.; Yazdi, I. K.; Prakash, G.; Antona, S.; Demarchi, D.; Buijsrogge, M. P.; Sluijter, J. P. G.; Hjortnaes, J.; Khademhosseini, A. Engineered 3D Cardiac Fibrotic Tissue to Study Fibrotic Remodeling. *Adv. Healthc. Mater.* **2017**, *6* (11), 1601434. https://doi.org/10.1002/adhm.201601434.

(75)   Zhou, L.; Chen, E.; Jin, W.; Wang, Y.; Zhou, J.; Wei, S. Monomer Zinc

Phthalocyanine/Upconversion Nanoparticle Coated with Hyaluronic Acid Crosslinked Gel as NIR Light-Activated Drug for: In Vitro Photodynamic Therapy. *Dalt. Trans.* **2016**, *45* (38). https://doi.org/10.1039/c6dt01929c.

(76)   Yu, J.; Zhang, Y.; Sun, W.; Wang, C.; Ranson, D.; Ye, Y.; Weng, Y.; Gu, Z. Internalized Compartments Encapsulated Nanogels for Targeted Drug Delivery. *Nanoscale* **2016**, *8* (17), 9178–9184. https://doi.org/10.1039/c5nr08895j.

(77)   Ding, Y.; Song, Z.; Liu, Q.; Wei, S.; Zhou, L.; Zhou, J.; Shen, J. An Enhanced Chemotherapeutic Effect Facilitated by Sonication of MSN. *Dalt. Trans.* **2017**, *46* (35), 11875–11883. https://doi.org/10.1039/c7dt02600e.

(78)   Poldervaart, M. T.; Goversen, B.; De Ruijter, M.; Abbadessa, A.; Melchels, F. P. W.; Öner, F. C.; Dhert, W. J. A.; Vermonden, T.; Alblas, J. 3D Bioprinting of Methacrylated Hyaluronic Acid (MeHA) Hydrogel with Intrinsic Osteogenicity. *PLoS One* **2017**, *12* (6), e0177628. https://doi.org/10.1371/journal.pone.0177628.

(79)   Lin, S.; Lee, W. Y. W.; Feng, Q.; Xu, L.; Wang, B.; Man, G. C. W.; Chen, Y.; Jiang, X.; Bian, L.; Cui, L.; Wei, B.; Li, G. Synergistic Effects on Mesenchymal Stem Cell-Based Cartilage Regeneration by Chondrogenic Preconditioning and Mechanical Stimulation. *Stem Cell Res. Ther.* **2017**, *8*, 1–12. https://doi.org/10.1186/s13287-017-0672-5.

(80)   Anseth, K. S.; Bowman, C. N.; Brannon-Peppas, L. Mechanical Properties of Hydrogels and Their Experimental Determination. *Biomaterials* **1996**, *17* (17), 1647–1657. https://doi.org/10.1016/0142-9612(96)87644-7.

(81)   Norioka, C.; Kawamura, A.; Miyata, T. Mechanical and Responsive Properties of Temperature-Responsive Gels Prepared: Via Atom Transfer Radical Polymerization. *Polym. Chem.* **2017**, *8* (39), 6050–6057. https://doi.org/10.1039/c7py01323j.

(82)   Basu, A.; Lindh, J.; Ålander, E.; Strømme, M.; Ferraz, N. On the Use of Ion-Crosslinked Nanocellulose Hydrogels for Wound Healing Solutions: Physicochemical Properties and Application-Oriented Biocompatibility Studies. *Carbohydr. Polym.* **2017**, *174*, 299–308. https://doi.org/10.1016/j.carbpol.2017.06.073.

(83)   Ilavsky M. Effect of Phase Transition on Swelling and Mechanical Behavior of Synthetic Hydrogels. *Responsive Gels Vol. Transitions I* **2005**, 109–173.

(84)   Sperling, L. H. Introduction to Physical Polymer Science. *Wiley* **1984**.

(85)   Ashammakhi, N.; Hasan, A.; Kaarela, O.; Byambaa, B.; Sheikhi, A.; Gaharwar, A. K.;

Khademhosseini, A. Bone Bioprinting: Advancing Frontiers in Bone Bioprinting (Adv. Healthcare Mater. 7/2019). *Adv. Healthc. Mater.* **2019**, *8* (7), 1970030. https://doi.org/10.1002/adhm.201970030.

(86)   Duan, B. State-of-the-Art Review of 3D Bioprinting for Cardiovascular Tissue Engineering. *Ann. Biomed. Eng.* **2017**, *45* (1), 195–209. https://doi.org/10.1007/s10439-016-1607-5.

(87)   Cui, X.; Boland, T.; D.D'Lima, D.; K. Lotz, M. Thermal Inkjet Printing in Tissue Engineering and Regenerative Medicine. *Recent Pat. Drug Deliv. Formul.* **2012**, *6* (2), 149–155. https://doi.org/10.2174/187221112800672949.

(88)   Saunders, R. E.; Derby, B. Inkjet Printing Biomaterials for Tissue Engineering: Bioprinting. *Int. Mater. Rev.* **2014**, *59* (8), 430–448. https://doi.org/10.1179/1743280414Y.0000000040.

(89)   Guillotin, B.; Souquet, A.; Catros, S.; Duocastella, M.; Pippenger, B.; Bellance, S.; Bareille, R.; Rémy, M.; Bordenave, L.; Amédée j, J.; Guillemot, F. Laser Assisted Bioprinting of Engineered Tissue with High Cell Density and Microscale Organization. *Biomaterials* **2010**, *31* (28), 7250–7256. https://doi.org/10.1016/j.biomaterials.2010.05.055.

(90)   Hribar, K. C.; Soman, P.; Warner, J.; Chung, P.; Chen, S. Light-Assisted Direct-Write of 3D Functional Biomaterials. *Lab on a Chip*. 2014, pp 268–275. https://doi.org/10.1039/c3lc50634g.

(91)   Ning, L.; Chen, X. A Brief Review of Extrusion-Based Tissue Scaffold Bio-Printing. *Biotechnology Journal*. 2017, p 1600671. https://doi.org/10.1002/biot.201600671.

(92)   Unagolla, J. M.; Jayasuriya, A. C. Hydrogel-Based 3D Bioprinting: A Comprehensive Review on Cell-Laden Hydrogels, Bioink Formulations, and Future Perspectives. *Appl. Mater. Today* **2020**, *18*, 100479. https://doi.org/10.1016/j.apmt.2019.100479.

(93)   Billiet, T.; Gevaert, E.; De Schryver, T.; Cornelissen, M.; Dubruel, P. The 3D Printing of Gelatin Methacrylamide Cell-Laden Tissue-Engineered Constructs with High Cell Viability. *Biomaterials* **2014**, *35* (1), 49–62. https://doi.org/10.1016/j.biomaterials.2013.09.078.

(94)   Blaeser, A.; Duarte Campos, D. F.; Puster, U.; Richtering, W.; Stevens, M. M.; Fischer, H. Controlling Shear Stress in 3D Bioprinting Is a Key Factor to Balance Printing Resolution and Stem Cell Integrity. *Adv. Healthc. Mater.* **2016**, *5* (3), 326–333. https://doi.org/10.1002/adhm.201500677.

(95)   Wüst, S.; Müller, R.; Hofmann, S. Controlled Positioning of Cells in Biomaterials—Approaches Towards 3D Tissue Printing. *J. Funct. Biomater.* **2011**, *2* (3), 119–154. https://doi.org/10.3390/jfb2030119.

(96)   Cui, X.; Boland, T. Human Microvasculature Fabrication Using Thermal Inkjet Printing Technology. *Biomaterials* **2009**, *30* (31), 6221–6227. https://doi.org/10.1016/j.biomaterials.2009.07.056.

(97)   Chang, C. C.; Boland, E. D.; Williams, S. K.; Hoying, J. B. Direct-Write Bioprinting Three-Dimensional Biohybrid Systems for Future Regenerative Therapies. *J. Biomed. Mater. Res. - Part B Appl. Biomater.* **2011**, *98 B* (1), 160–170. https://doi.org/10.1002/jbm.b.31831.

(98)   Ali, M.; Pages, E.; Ducom, A.; Fontaine, A.; Guillemot, F. Controlling Laser-Induced Jet Formation for Bioprinting Mesenchymal Stem Cells with High Viability and High Resolution. *Biofabrication* **2014**, *6* (4), 045001. https://doi.org/10.1088/1758-5082/6/4/045001.

(99)   Lin, Y.; Huang, G.; Huang, Y.; Tzeng, T. R. J.; Chrisey, D. Effect of Laser Fluence in Laser-Assisted Direct Writing of Human Colon Cancer Cell. *Rapid Prototyp. J.* **2010**, *16* (3), 202–208. https://doi.org/10.1108/13552541011034870.

(100)   Billiet, T.; Vandenhaute, M.; Schelfhout, J.; Van Vlierberghe, S.; Dubruel, P. A Review of Trends and Limitations in Hydrogel-Rapid Prototyping for Tissue Engineering. *Biomaterials* **2012**, *33* (26), 6020–6041. https://doi.org/10.1016/j.biomaterials.2012.04.050.

(101)   Kirchmajer, D. M.; Gorkin, R.; In Het Panhuis, M. An Overview of the Suitability of Hydrogel-Forming Polymers for Extrusion-Based 3D-Printing. *J. Mater. Chem. B* **2015**, *3* (20), 4105–4117. https://doi.org/10.1039/c5tb00393h.

(102)   Ozbolat, I. T.; Hospodiuk, M. Current Advances and Future Perspectives in Extrusion-Based Bioprinting. *Biomaterials* **2016**, *76*, 321–343. https://doi.org/10.1016/j.biomaterials.2015.10.076.

(103)   Ji, S.; Guvendiren, M. Recent Advances in Bioink Design for 3D Bioprinting of Tissues and Organs. *Front. Bioeng. Biotechnol.* **2017**, *5* (APR), 23. https://doi.org/10.3389/fbioe.2017.00023.

(104)   Guvendiren, M.; Molde, J.; Soares, R. M. D.; Kohn, J. Designing Biomaterials for 3D Printing. *ACS Biomater. Sci. Eng.* **2016**, *2* (10), 1679–1693. https://doi.org/10.1021/acsbiomaterials.6b00121.

(105)   Yu, J.; Park, S. A.; Kim, W. D.; Ha, T.; Xin, Y. Z.; Lee, J.; Lee, D. Current Advances in 3D Bioprinting Technology and Its Applications for Tissue Engineering. *Polymers (Basel).* **2020**, *12* (12), 1–30. https://doi.org/10.3390/polym12122958.

(106)   Ribeiro, A.; Blokzijl, M. M.; Levato, R.; Visser, C. W.; Castilho, M.; Hennink, W. E.; Vermonden, T.; Malda, J. Assessing Bioink Shape Fidelity to Aid Material Development in 3D Bioprinting. *Biofabrication* **2018**, *10* (1), 014102. https://doi.org/10.1088/1758-5090/aa90e2.

(107) Schwab, A.; Levato, R.; D'Este, M.; Piluso, S.; Eglin, D.; Malda, J. Printability and Shape Fidelity of Bioinks in 3D Bioprinting. *Chem. Rev.* **2020**, *120* (19), 11028–11055. https://doi.org/10.1021/acs.chemrev.0c00084.

(108) Nguyen, K. T.; West, J. L. Photopolymerizable Hydrogels for Tissue Engineering Applications. *Biomaterials* **2002**, *23* (22), 4307–4314. https://doi.org/10.1016/S0142-9612(02)00175-8.

(109) Macdougall, L. J.; Anseth, K. Bioerodible Hydrogels Based on Photopolymerized Poly(Ethylene Glycol)- Co-Poly(α-Hydroxy Acid) Diacrylate Macromers. *Macromolecules* **2020**, *53* (7), 2295–2298. https://doi.org/10.1021/acs.macromol.0c00030.

(110) Kim, I. S.; Jeong, Y. Il; Kim, S. H. Self-Assembled Hydrogel Nanoparticles Composed of Dextran and Poly(Ethylene Glycol) Macromer. *Int. J. Pharm.* **2000**, *205* (1–2), 109–116. https://doi.org/10.1016/S0378-5173(00)00486-5.

(111) Yu, C.; Schimelman, J.; Wang, P.; Miller, K. L.; Ma, X.; You, S.; Guan, J.; Sun, B.; Zhu, W.; Chen, S. Photopolymerizable Biomaterials and Light-Based 3D Printing Strategies for Biomedical Applications. *Chem. Rev.* **2020**, *120* (19), 10695–10743. https://doi.org/10.1021/acs.chemrev.9b00810.

(112) Yagci, Y.; Jockusch, S.; Turro, N. J. Photoinitiated Polymerization: Advances, Challenges, and Opportunities. *Macromolecules* **2010**, *43* (15), 6245–6260. https://doi.org/10.1021/ma1007545.

(113) Shih, H.; Lin, C. C. Visible-Light-Mediated Thiol-Ene Hydrogelation Using Eosin-Y as the Only Photoinitiator. *Macromol. Rapid Commun.* **2013**, *34* (3), 269–273. https://doi.org/10.1002/marc.201200605.

(114) Fairbanks, B. D.; Schwartz, M. P.; Bowman, C. N.; Anseth, K. S. Photoinitiated Polymerization of PEG-Diacrylate with Lithium Phenyl-2,4,6-Trimethylbenzoylphosphinate: Polymerization Rate and Cytocompatibility. *Biomaterials* **2009**, No. 35, 6702–6707. https://doi.org/10.1016/j.biomaterials.2009.08.055.

(115) Greant, C.; Van Durme, B.; Van Hoorick, J.; Van Vlierberghe, S. Multiphoton Lithography as a Promising Tool for Biomedical Applications. *Adv. Funct. Mater.* **2023**, 2212641. https://doi.org/10.1002/adfm.202212641.

(116) Chandler, E. M.; Berglund, C. M.; Lee, J. S.; Polacheck, W. J.; Gleghorn, J. P.; Kirby, B. J.; Fischbach, C. Stiffness of Photocrosslinked RGD-Alginate Gels Regulates Adipose Progenitor Cell Behavior. *Biotechnol. Bioeng.* **2011**, *108* (7), 1683–1692. https://doi.org/10.1002/bit.23079.

(117) Wang, X.; Jiang, M.; Zhou, Z.; Gou, J.; Hui, D. 3D Printing of Polymer Matrix Composites: A Review and Prospective. *Compos. Part B Eng.* **2017**, *110*, 442–458. https://doi.org/10.1016/j.compositesb.2016.11.034.

(118) Chan, V.; Jeong, J. H.; Bajaj, P.; Collens, M.; Saif, T.; Kong, H.; Bashir, R. Multi-Material Bio-Fabrication of Hydrogel Cantilevers and Actuators with Stereolithography. *Lab Chip* **2012**, *12* (1), 88–98. https://doi.org/10.1039/c1lc20688e.

(119) Lim, K. S.; Schon, B. S.; Mekhileri, N. V.; Brown, G. C. J.; Chia, C. M.; Prabakar, S.; Hooper, G. J.; Woodfield, T. B. F. New Visible-Light Photoinitiating System for Improved Print Fidelity in Gelatin-Based Bioinks. *ACS Biomater. Sci. Eng.* **2016**, *2* (10), 1752–1762. https://doi.org/10.1021/acsbiomaterials.6b00149.

(120) Rouillard, A. D.; Berglund, C. M.; Lee, J. Y.; Polacheck, W. J.; Tsui, Y.; Bonassar, L. J.; Kirby, B. J. Methods for Photocrosslinking Alginate Hydrogel Scaffolds with High Cell Viability. *Tissue Eng. - Part C Methods* **2011**, *17* (2). https://doi.org/10.1089/ten.tec.2009.0582.

(121) Whittaker, J. L.; Choudhury, N. R.; Dutta, N. K.; Zannettino, A. Facile and Rapid Ruthenium Mediated Photo-Crosslinking of Bombyx Mori Silk Fibroin. *J. Mater. Chem. B* **2014**, *2* (37), 6259–6270. https://doi.org/10.1039/c4tb00698d.

(122) Xiao, P.; Zhang, J.; Dumur, F.; Tehfe, M. A.; Morlet-Savary, F.; Graff, B.; Gigmes, D.; Fouassier, J. P.; Lalevée, J. Visible Light Sensitive Photoinitiating Systems: Recent Progress in Cationic and Radical Photopolymerization Reactions under Soft Conditions. *Prog. Polym. Sci.* **2015**, *41* (C), 32–66. https://doi.org/10.1016/j.progpolymsci.2014.09.001.

(123) Chen, M.; Zhong, M.; Johnson, J. A. Light-Controlled Radical Polymerization: Mechanisms, Methods, and Applications. *Chem. Rev.* **2016**, *116* (17), 10167–10211. https://doi.org/10.1021/acs.chemrev.5b00671.

(124) Alge, D. L. Photochemical Patterning of Cellular Microenvironments. In *Microscale Technologies for Cell Engineering*; Springer, 2015; pp 27–46. https://doi.org/10.1007/978-3-319-20726-1_2.

(125) Kloxin, A. M.; Kasko, A. M.; Salinas, C. N.; Anseth, K. S. Photodegradable Hydrogels for Dynamic Tuning of Physical and Chemical Properties. *Science*. 2009, pp 59–63. https://doi.org/10.1126/science.1169494.

(126) Yang, C.; Tibbitt, M. W.; Basta, L.; Anseth, K. S. Mechanical Memory and Dosing Influence Stem Cell Fate. *Nat. Mater.* **2014**, *13* (6), 645–652. https://doi.org/10.1038/nmat3889.

(127) Pelliccioli, A. P.; Wirz, J. Photoremovable Protecting Groups: Reaction Mechanisms and

Applications. *Photochem. Photobiol. Sci.* **2002**, *1* (7), 441–458. https://doi.org/10.1039/b200777k.

(128) Klán, P.; Šolomek, T.; Bochet, C. G.; Blanc, A.; Givens, R.; Rubina, M.; Popik, V.; Kostikov, A.; Wirz, J. Photoremovable Protecting Groups in Chemistry and Biology: Reaction Mechanisms and Efficacy. *Chem. Rev.* **2013**, *113* (1), 119–191. https://doi.org/10.1021/cr300177k.

(129) Levalley, P. J.; Neelarapu, R.; Sutherland, B. P.; Dasgupta, S.; Kloxin, C. J.; Kloxin, A. M. Photolabile Linkers: Exploiting Labile Bond Chemistry to Control Mode and Rate of Hydrogel Degradation and Protein Release. *J. Am. Chem. Soc.* **2020**, *142* (10), 4671–4679. https://doi.org/10.1021/jacs.9b11564.

(130) Wang, P. Photolabile Protecting Groups: Structure and Reactivity. *Asian J. Org. Chem.* **2013**, *2* (6), 452–464. https://doi.org/10.1002/ajoc.201200197.

(131) Griffin, D. R.; Kasko, A. M. Photodegradable Macromers and Hydrogels for Live Cell Encapsulation and Release. *J. Am. Chem. Soc.* **2012**, *134* (31), 13103–13107. https://doi.org/10.1021/ja305280w.

(132) Griffin, D. R.; Kasko, A. M. Photoselective Delivery of Model Therapeutics from Hydrogels. *ACS Macro Lett.* **2012**, *1* (11), 1330–1334. https://doi.org/10.1021/mz300366s.

(133) Holmes, C. P. Model Studies for New O-Nitrobenzyl Photolabile Linkers: Substituent Effects on the Rates of Photochemical Cleavage. *J. Org. Chem.* **1997**, *62* (8), 2370–2380. https://doi.org/10.1021/jo961602x.

(134) Salerno, C. P.; Cleaves, H. J. A Simple Synthesis of Photolabile α-Methyl Nitrobenzyl Compounds. *Synth. Commun.* **2004**, *34* (13), 2379–2386. https://doi.org/10.1081/SCC-120039491.

(135) Mikkelsen, R. J. T.; Grier, K. E.; Mortensen, K. T.; Nielsen, T. E.; Qvortrup, K. Photolabile Linkers for Solid-Phase Synthesis. *ACS Comb. Sci.* **2018**, *20* (7), 377–379. https://doi.org/10.1021/acscombsci.8b00028.

(136) DeForest, C. A.; Anseth, K. S. Cytocompatible Click-Based Hydrogels with Dynamically Tunable Properties through Orthogonal Photoconjugation and Photocleavage Reactions. *Nat. Chem.* **2011**, *3* (12), 925–931. https://doi.org/10.1038/nchem.1174.

(137) McKinnon, D. D.; Brown, T. E.; Kyburz, K. A.; Kiyotake, E.; Anseth, K. S. Design and Characterization of a Synthetically Accessible, Photodegradable Hydrogel for User-Directed Formation of Neural Networks. *Biomacromolecules* **2014**, *15* (7), 2808–2816. https://doi.org/10.1021/bm500731b.

(138) Kharkar, P. M.; Kiick, K. L.; Kloxin, A. M. Design of Thiol- and Light-Sensitive Degradable Hydrogels Using Michael-Type Addition Reactions. *Polym. Chem.* **2015**, *6* (31), 5565–5574. https://doi.org/10.1039/c5py00750j.

(139) Kharkar, P. M.; Scott, R. A.; Olney, L. P.; LeValley, P. J.; Maverakis, E.; Kiick, K. L.; Kloxin, A. M. Controlling the Release of Small, Bioactive Proteins via Dual Mechanisms with Therapeutic Potential. *Adv. Healthc. Mater.* **2017**, *6* (24), 1700713. https://doi.org/10.1002/adhm.201700713.

(140) Lunzer, M.; Shi, L.; Andriotis, O. G.; Gruber, P.; Markovic, M.; Thurner, P. J.; Ossipov, D.; Liska, R.; Ovsianikov, A. A Modular Approach to Sensitized Two-Photon Patterning of Photodegradable Hydrogels. *Angew. Chemie* **2018**, *130* (46), 15342–15347. https://doi.org/10.1002/ange.201808908.

(141) Romano, A.; Angelini, A.; Rossegger, E.; Palmara, G.; Castellino, M.; Frascella, F.; Chiappone, A.; Chiadò, A.; Sangermano, M.; Schlögl, S.; Roppolo, I. Laser-Triggered Writing and Biofunctionalization of Thiol-Ene Networks. *Macromol. Rapid Commun.* **2020**, *41* (10), 2000084. https://doi.org/10.1002/marc.202000084.

(142) Selimis, A.; Mironov, V.; Farsari, M. NoDirect Laser Writing: Principles and Materials for Scaffold 3D Printing. *Microelectron. Eng.* **2015**, 83–89. https://doi.org/10.1016/j.mee.2014.10.001.

(143) Bae, S. J.; Suh, J. M.; Sohn, Y. S.; Bae, Y. H.; Kim, S. W.; Jeong, B. Thermogelling Poly(Caprolactone-6-Ethylene Glycol-b-Caprolactone) Aqueous Solutions. *Macromolecules* **2005**, *38* (12), 5260–5265. https://doi.org/10.1021/ma050489m.

(144) Qi, H.; Zhou, H.; Tang, Q.; Lee, J. Y.; Fan, Z.; Kim, S.; Staub, M. C.; Zhou, T.; Mei, S.; Han, L.; Pochan, D. J.; Cheng, H.; Hu, W.; Li, C. Y. Block Copolymer Crystalsomes with an Ultrathin Shell to Extend Blood Circulation Time. *Nat. Commun.* **2018**, *9* (1), 3005. https://doi.org/10.1038/s41467-018-05396-x.

(145) Grossen, P.; Witzigmann, D.; Sieber, S.; Huwyler, J. PEG-PCL-Based Nanomedicines: A Biodegradable Drug Delivery System and Its Application. *J. Control. Release* **2017**, *260*, 46–60. https://doi.org/10.1016/j.jconrel.2017.05.028.

(146) Duda, A.; Hofman, A.; Slomkowski, S.; Penczek, S.; Zbigniew, F. Living Pseudoanionic Polymerization of Ecaprolactone. Poly(e-Caprolactone) Free of Cyclics and with Controlled End Groups. *Macromolecules* **1990**, *23* (6), 1640–1646. https://doi.org/10.1021/ma00208a013.

(147) Kricheldorf, H. R.; Boettcher, C. Polylactones 26. Lithium Alkoxide-initiated Polymerizations of

L-lactide. *Die Makromol. Chemie* **1993**, *194* (6), 1665–1669.

(148) Dubois, P.; Jérôme, R.; Teyssié, P. Aluminium Alkoxides: A Family of Versatile Initiators for the Ring-opening Polymerization of Lactones and Lactides. *Makromol. Chemie. Macromol. Symp.* **1991**, *42–43* (1), 103–116. https://doi.org/10.1002/masy.19910420108.

(149) Kowalski, A.; Duda, A.; Penczek, S. Kinetics and Mechanism of Cyclic Esters Polymerization Initiated with Tin(II) Octoate, 1: Polymerization of ε-Caprolactone. *Macromol. Rapid Commun.* **1998**, *19* (11), 567–572. https://doi.org/10.1002/(sici)1521-3927(19981101)19:11<567::aid-marc567>3.0.co;2-t.

(150) Bailey, F. E.; Koleske, J. V. *Alkylene Oxides and Their Polymers*; CRC Press, 2020. https://doi.org/10.1201/9781003066569.

(151) Theis, J.; Ritter, H. Formation of Epoxide-Amine Oligo-Adducts as OH-Functionalized Initiators for the Ring-Opening Polymerization of ε-Caprolactone. *Beilstein J. Org. Chem.* **2010**, *6*, 938–944. https://doi.org/10.3762/bjoc.6.105.

(152) Labet, M.; Thielemans, W. Synthesis of Polycaprolactone: A Review. *Chem. Soc. Rev.* **2009**, *38* (12), 3484–3504. https://doi.org/10.1039/b820162p.

(153) Brandrup, J.; Immergut, E. .; Grulke, E. . *Polymer Handbook. Fourth Edition*; Wiley Interscience Publication: New York, 1999.

(154) Kissin, Y. V. Molecular Weight Distributions of Linear Polymers: Detailed Analysis from GPC Data. *J. Polym. Sci. Part A Polym. Chem.* **1995**, *33* (2), 227–237. https://doi.org/10.1002/pola.1995.080330205.

(155) Inoue, S. Immortal Polymerization: The Outset, Development, and Application. *J. Polym. Sci. Part A Polym. Chem.* **2000**, *38*, 2861–2871.

(156) Corten, C.; Kretschmer, K.; Kuckling, D. Novel Multi-Responsive P2VP-Block-PNIPAAm Block Copolymers via Nitroxide-Mediated Radical Polymerization. *Beilstein J. Org. Chem.* **2010**, *6*, 756–765. https://doi.org/10.3762/bjoc.6.89.

(157) Sánchez-Soto, P. J.; Ginés, J. M.; Arias, M. J.; Novák, C.; Ruiz-Conde, A. Effect of Molecular Mass on the Melting Temperature, Enthalpy and Entropy of Hydroxy-Terminated PEO. *J. Therm. Anal. Calorim.* **2002**, *67* (1), 189–197. https://doi.org/10.1023/A:1013758518721.

(158) He, C.; Sun, J.; Deng, C.; Zhao, T.; Deng, M.; Chen, X.; Jing, X. Study of the Synthesis, Crystallization, and Morphology of Poly(Ethylene Glycol) - Poly(ε-Caprolactone) Diblock

Copolymers. *Biomacromolecules* **2004**, *5* (5), 2042–2047. https://doi.org/10.1021/bm049720e.

(159)   Wu, K.; Yu, L.; Ding, J. Synthesis of PCL-PEG-PCL Triblock Copolymer via Organocatalytic Ring-Opening Polymerization and Its Application as an Injectable Hydrogel - An Interdisciplinary Learning Trial. *J. Chem. Educ.* **2020**, *97* (11), 4158–4165. https://doi.org/10.1021/acs.jchemed.0c00325.

(160)   Zhang, Y.; Zhuo, R. X. Synthesis and in Vitro Drug Release Behavior of Amphiphilic Triblock Copolymer Nanoparticles Based on Poly (Ethylene Glycol) and Polycaprolactone. *Biomaterials* **2005**, *26* (33), 6736–6742. https://doi.org/10.1016/j.biomaterials.2005.03.045.

(161)   Zhu, Z.; Xiong, C.; Zhang, L.; Deng, X. Synthesis and Characterization of Poly (1 -Caprolactone) – Poly (Ethylene Glycol) Block Copolymer. *J. Polym. Sci. Part A Polym. Chem.* **1997**, *35*, 709–714.

(162)   Craig, D. Q. M.; Newton, J. M. Characterisation of Polyethylene Glycols Using Solution Calorimetry. *Int. J. Pharm.* **1991**, *74* (1), 43–48. https://doi.org/10.1016/0378-5173(91)90406-E.

(163)   Kambe, Y. Thermal Behaviour of Poly(Ethylene Oxide) as Revealed by Differential Scanning Calorimetry. *Polymer*. 1980, pp 352–355. https://doi.org/10.1016/0032-3861(80)90280-3.

(164)   An, J. H.; Kim, H. S.; Chung, D. J.; Lee, D. S. Thermal Behaviour of Poly(ε-Caprolactone)-Poly(Ethylene Glycol)-Poly(ε-Caprolactone) Tri-Block Copolymers. *J. Mater. Sci.* **2001**, *36*, 715–722.

(165)   Li, X.; Dong, X.; Zhou, J.; Bao, J.; Chen, S.; Lu, W.; Zhang, X.; Chen, W. Confined Crystallization and Melting Behaviors of Poly(Ethylene Glycol) End-Functionalized by Hydrogen Bonding Groups: Effect of Contents for Functional Units. *Polym. Cryst.* **2020**, *3* (5). https://doi.org/10.1002/pcr2.10158.

(166)   Fischer, E. W.; Sterzel, H. J.; Wegner, G. Investigation of the Structure of Solution Grown Crystals of Lactide Copolymers by Means of Chemical Reactions. *Kolloid-Zeitschrift Zeitschrift für Polym.* **1973**, *251* (11). https://doi.org/10.1007/BF01498927.

(167)   Ali, S.; Cuchiara, M. L.; West, J. L. Micropatterning of Poly(Ethylene Glycol) Diacrylate Hydrogels. *Methods Cell Biol.* **2014**, *121*, 105–119. https://doi.org/10.1016/B978-0-12-800281-0.00008-7.

(168)   Porter, R. S.; Johnson, J. F. Non-Newtonian Viscosity of Polymers. *J. Appl. Phys.* **1961**, *32* (11), 2326–2331. https://doi.org/10.1063/1.1777067.

(169) Zare, Y.; Park, S. P.; Rhee, K. Y. Analysis of Complex Viscosity and Shear Thinning Behavior in Poly (Lactic Acid)/Poly (Ethylene Oxide)/Carbon Nanotubes Biosensor Based on Carreau– Yasuda Model. *Results Phys.* **2019**, *13*, 102245. https://doi.org/10.1016/j.rinp.2019.102245.

(170) Jongschaap, R. J. J.; Wientjes, R. H. W.; Duits, M. H. G.; Mellema, J. Generalized Transient Network Model for Associative Polymer Networks. *Macromolecules* **2001**, *34* (4). https://doi.org/10.1021/ma0001640.

(171) Webers, S.; Hess, M.; Landers, J.; Schmidt, A. M.; Wende, H. Effect of Phase Transitions in Polymer Solutions on the Magnetic Response of Embedded Nanoparticles. *ACS Appl. Polym. Mater.* **2020**, *2* (7), 2676–2685. https://doi.org/10.1021/acsapm.0c00298.

(172) Cai, L. H.; Panyukov, S.; Rubinstein, M. Mobility of Nonsticky Nanoparticles in Polymer Liquids. *Macromolecules* **2011**, *44* (19), 7853–7863. https://doi.org/10.1021/ma201583q.

(173) Podgornik, R. Book Review: Polymer Physics. M. Rubinshtein and R. H. Colby, Oxford University Press, 2003. *J. Stat. Phys.* **2004**, *115* (5/6), 1757–1761. https://doi.org/10.1023/b:joss.0000028242.25527.8b.

(174) Elvin, C. M.; Vuocolo, T.; Brownlee, A. G.; Sando, L.; Huson, M. G.; Liyou, N. E.; Stockwell, P. R.; Lyons, R. E.; Kim, M.; Edwards, G. A.; Johnson, G.; McFarland, G. A.; Ramshaw, J. A. M.; Werkmeister, J. A. A Highly Elastic Tissue Sealant Based on Photopolymerised Gelatin. *Biomaterials* **2010**, *31* (32), 8323–8331. https://doi.org/10.1016/j.biomaterials.2010.07.032.

(175) Alvarez-Lorenzo, C.; Bromberg, L.; Concheiro, A. Light-Sensitive Intelligent Drug Delivery Systems. *Photochem. Photobiol.* **2009**, *85* (4), 848–860. https://doi.org/10.1111/j.1751-1097.2008.00530.x.

(176) Chatani, S.; Kloxin, C. J.; Bowman, C. N. The Power of Light in Polymer Science: Photochemical Processes to Manipulate Polymer Formation, Structure, and Properties. *Polym. Chem.* **2014**, *5* (7), 2187–2201. https://doi.org/10.1039/c3py01334k.

(177) Ruskowitz, E. R.; DeForest, C. A. Photoresponsive Biomaterials for Targeted Drug Delivery and 4D Cell Culture. *Nat. Rev. Mater.* **2018**, 1–17. https://doi.org/10.1038/natrevmats.2017.87.

(178) Kloxin, A. M.; Tibbitt, M. W.; Kasko, A. M.; Fairbairn, J. A.; Anseth, K. S. Tunable Hydrogels for External Manipulation of Cellular Microenvironments through Controlled Photodegradation. *Adv. Mater.* **2010**, *22* (1), 61–66. https://doi.org/10.1002/adma.200900917.

(179) Cameron, J. F.; Willson, C. G.; Fre, J. M. J. Photogeneration of Amines from R -Keto Carbamates : Photochemical Studies. **1996**, *7863* (9), 12925–12937.

(180) Il'ichev, Y. V.; Schwörer, M. A.; Wirz, J. Photochemical Reaction Mechanisms of 2-Nitrobenzyl Compounds: Methyl Ethers and Caged ATP. *J. Am. Chem. Soc.* **2004**, *126* (14), 4581–4595. https://doi.org/10.1021/ja039071z.

(181) Tibbitt, M. W.; Kloxin, A. M.; Dyamenahalli, K. U.; Anseth, K. S. Controlled Two-Photon Photodegradation of PEG Hydrogels to Study and Manipulate Subcellular Interactions on Soft Materials. *Soft Matter* **2010**, *6* (20), 5100–5108. https://doi.org/10.1039/c0sm00174k.

(182) Xiong, R.; Zhang, Z.; Shen, J.; Lin, Y.; Huang, Y.; Chrisey, D. B. Bubble Formation Modeling during Laser Direct Writing of Glycerol Solutions. *J. Micro Nano-Manufacturing* **2015**, *3* (1), 011004. https://doi.org/10.1115/1.4029264.

8 APPENDIX

8.1 Additional Information

Table 8.1. Relative ^{1}H-NMR signal intensities of all block copolymers fractions

TRIBLOCK COPOLYMERS	CHEMICAL SHIFTS, δ ppm						
	1.4	1.65	2.3	2.6	3.66	4.08	4.28
$C_1E_8C_1$	16.2	50	15.74	0.05	398.95	13.62	1.36
purified	15.25	50	33.07	0	1180.17	24.37	2.1
separated	20.65	50	19.4	0.06	293.26	17.5	1.31
$C_1E_{35}C_1$	4.1	50	4.17	0.3	275.29	3.79	0.07
purified	4.47	50	40.49	0.31	4729.26	47.92	0.68
separated	23.94	50	21.12	0	193.91	18.86	0.23
$C_1E_{100}C_1$	0.48	50	0.41	0.16	622.86	0.36	0.35
purified	0.34	50	0.49	0.3	909.99	0.26	0.16
separated	15.12	50	9.05	0.29	377.88	5.58	0.48
$C_3E_8C_3$	24.85	50	24.34	0.02	181.36	22.7	0.47
purified	22.25	50	24.5	0.03	183.9	22.96	0.28
separated	21.98	50	21.58	0.02	153.63	20.4	0.67
$C_3E_{35}C_3$	9.88	50	10.01	0.01	325.37	9.17	0.25
purified	7.61	50	7.76	0.01	563.01	6.81	0.29
separated	22.95	50	20.91	0	129.37	19.76	0.09
$C_3E_{100}C_3$	5.27	50	6.06	0.09	441.36	5.46	0.33
purified	1.23	50	2.46	0.01	1010.9	1.77	0.34
separated	22.1	50	17.49	0.06	168.79	15.17	0.65
$C_5E_8C_5$	10.74	50	25.58	0.21	87.7	23.61	0.84
purified	41.86	50	19.63	0	74.52	19.32	0.00
separated	7.08	50	22.59	0	79.44	21.46	0.42
$C_5E_{35}C_5$	15.5	50	15.53	0	160.47	14.53	0.21
purified	13.21	50	13.5	0	586.82	12.4	0.55
separated	23.57	50	23.51	0	39.39	21.98	0.00
$C_5E_{100}C_5$	18.09	50	19.86	0.3	1496.18	15.42	1.61
purified	11.02	50	2.37	0.01	574.18	2.63	0.27
separated	24.33	50	18.92	0.06	142.43	16.84	0.74
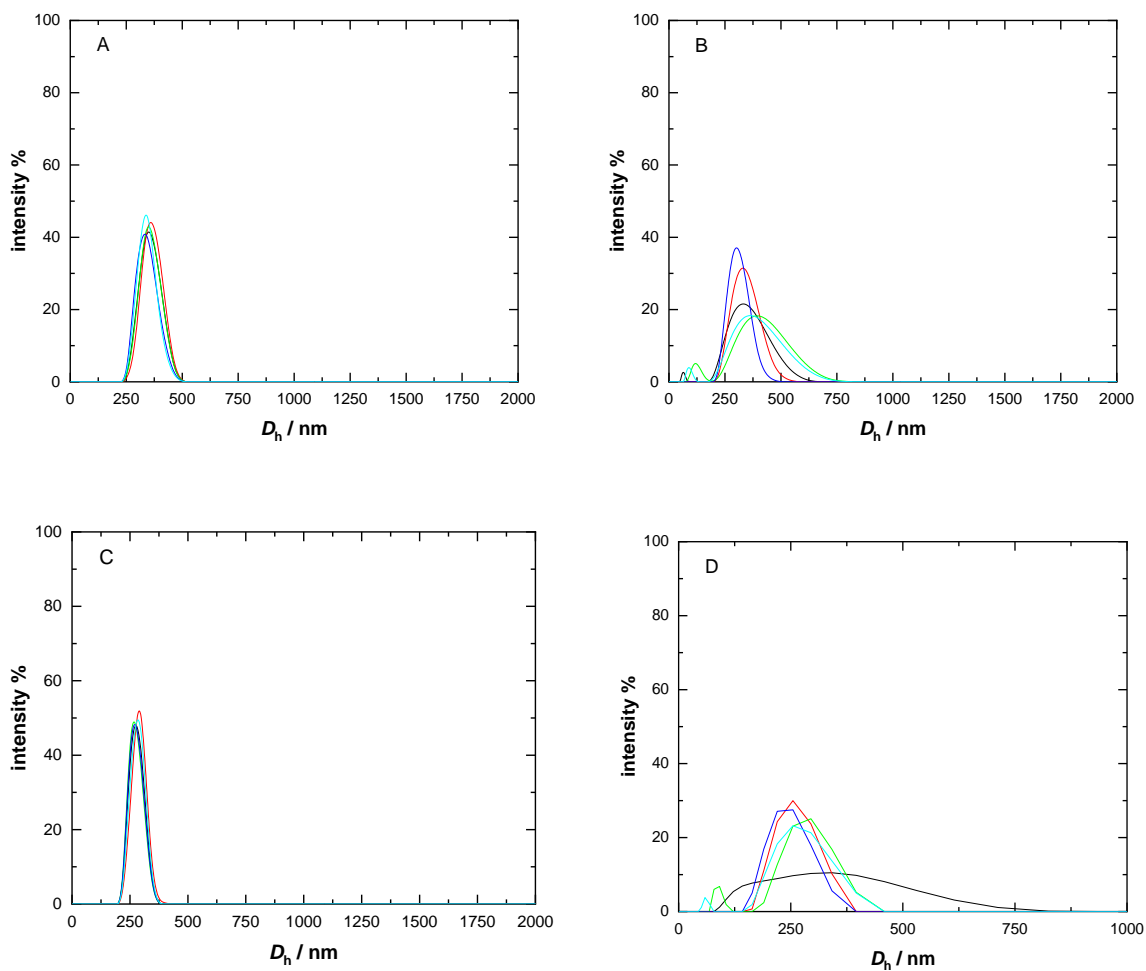
Figure 8.1. DLS curves of raw triblock copolymers. A) $C_1P_{35}C_1$, B) $C_3P_{35}C_3$, C) $C_3P_{100}C_3$ and D) filtrated $C_5P_{100}C_5$. The curves show five independent measurements.
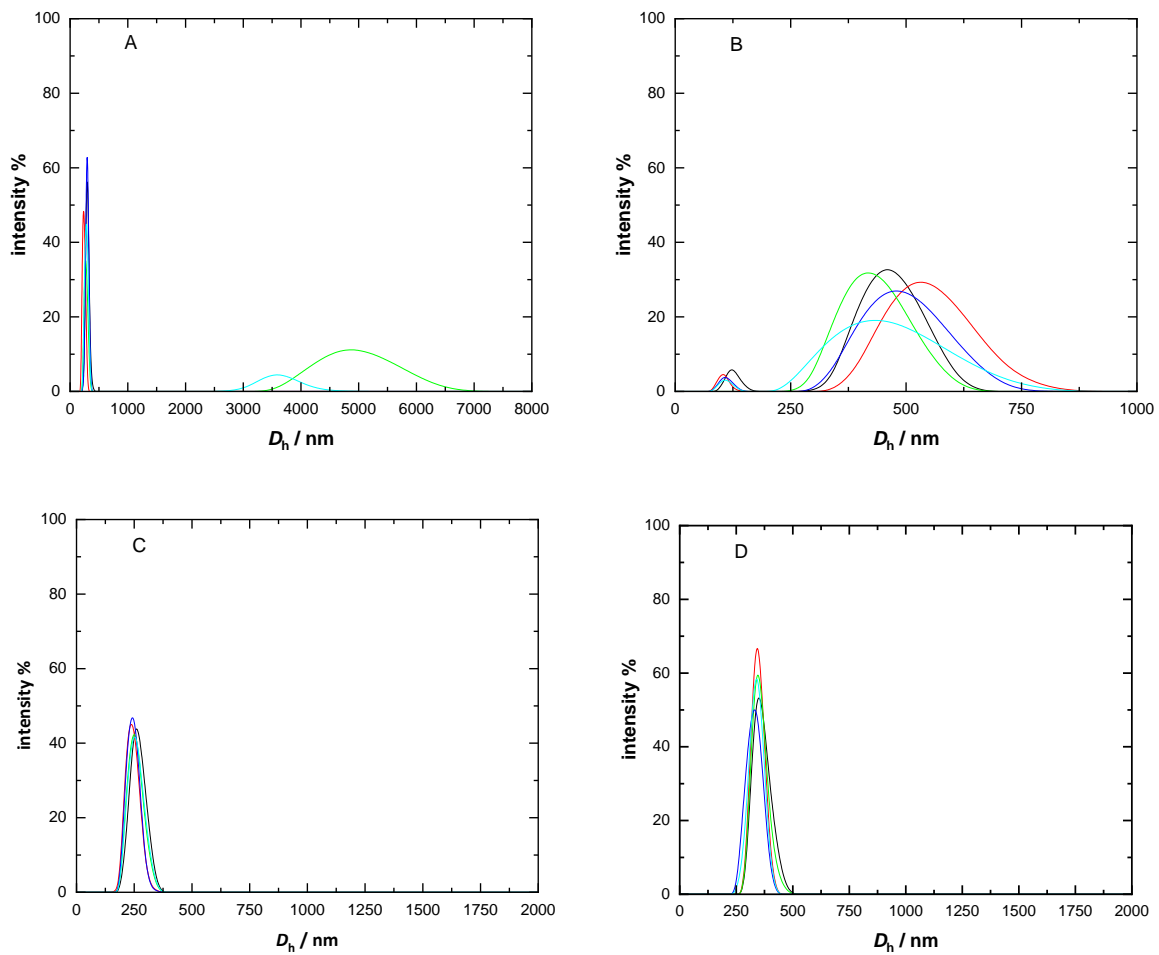
Figure 8.2. DLS curves of purified triblock copolymers: A) $C_1P_8C_1$, B) $C_1P_{35}C_1$, C) $C_1P_{100}C_1$ D) $C_3P_{35}C_3$. The curves show five independent measurements.
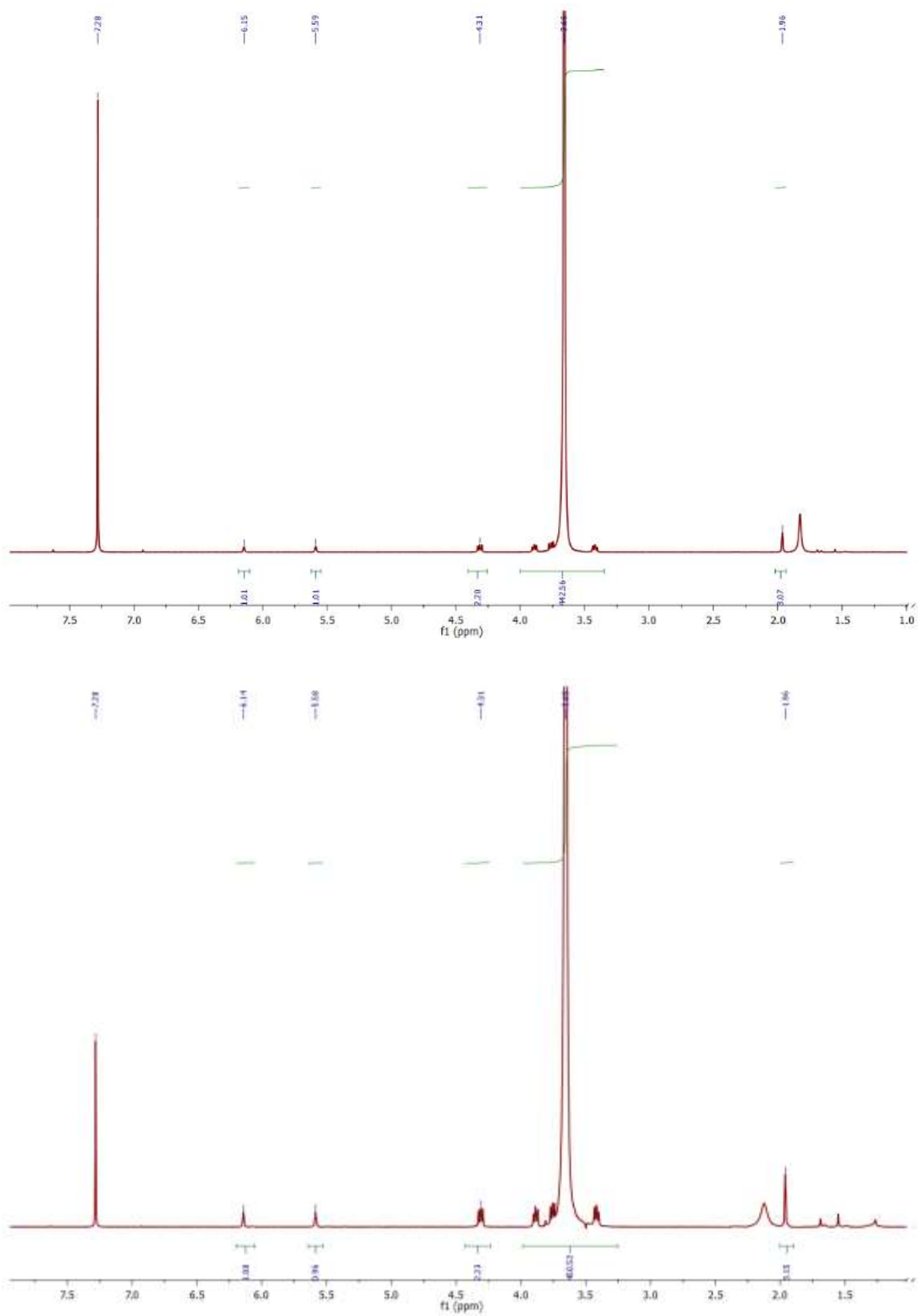
Figure 8.3. ¹H-NMR spectra of the synthesized PEG$_{8K}$DMA.
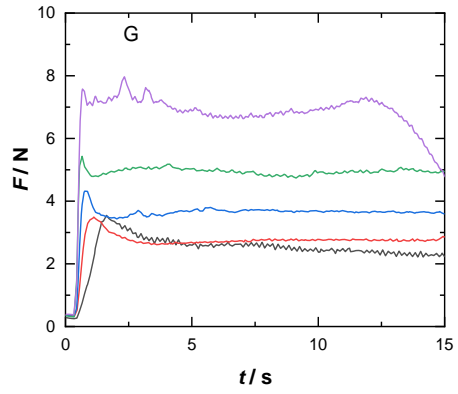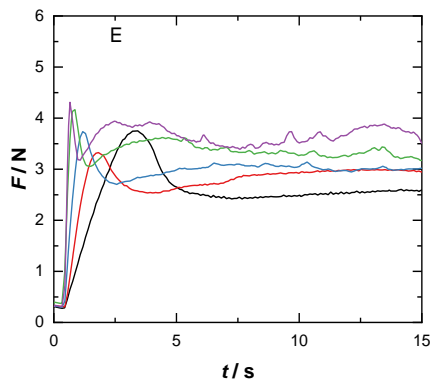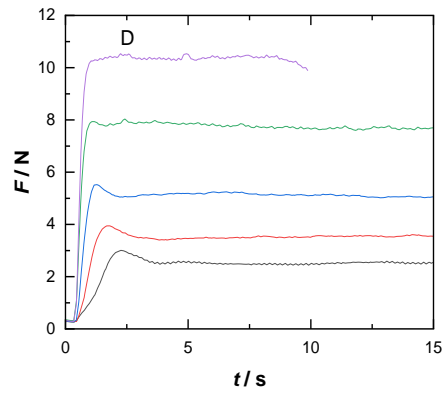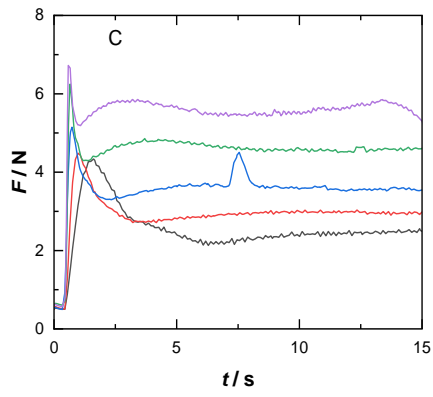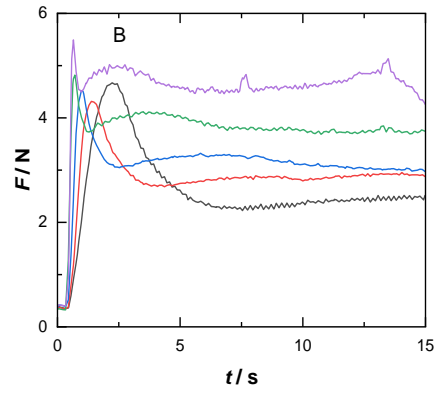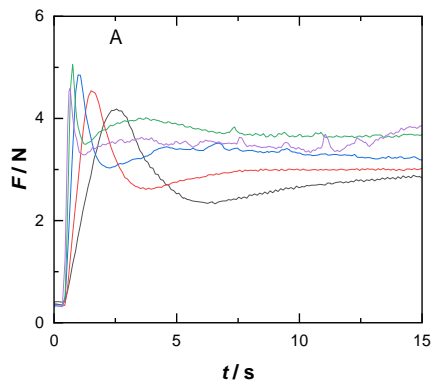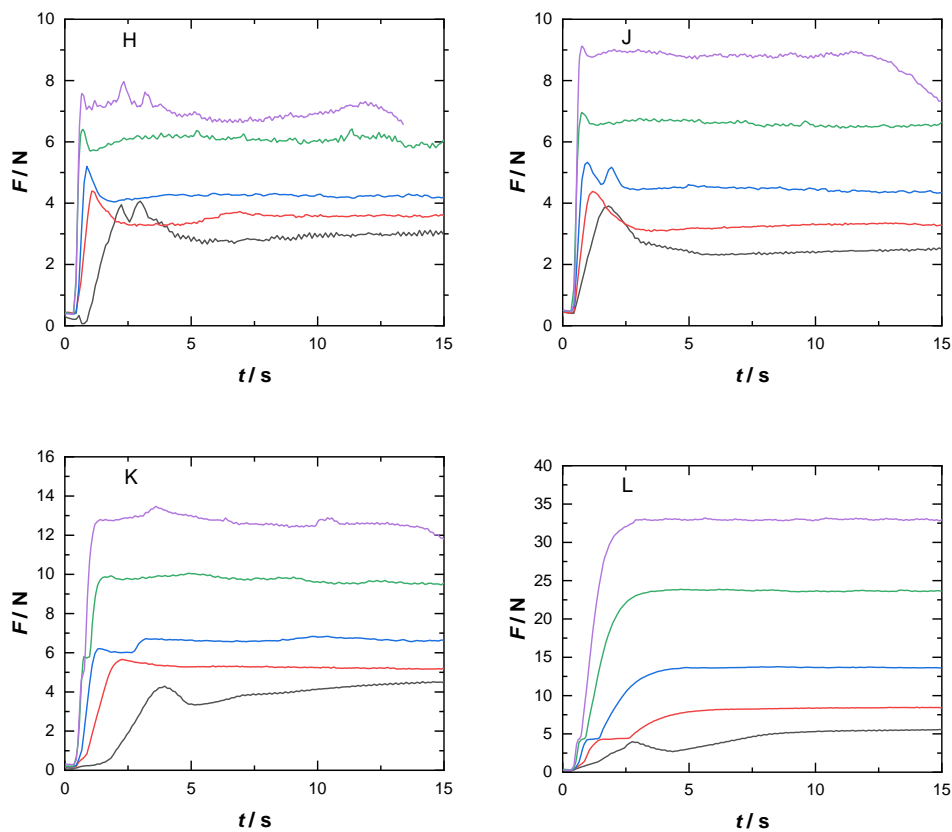
Figure 8.4. Capillary extrusion of PEG-based solutions: A) 0/1, B) 0/3.5, C) 0/5, D) 0/10. Capillary extrusion of BS_{10}: A) 10/0, B) 10/1, C)10/3.5, D) 10/5. capillary extrusion of BS_{20}: J) 20/3.5, K) 20/5, L) 20/10. The velocity of extrusions: 8.3 10^{-4} x m x s^{-1} (black), 16.7 10^{-4} m x s^{-1} (red), 33.3 10^{-4} m x s^{-1} (blue), 66.7 10^{-4} m x s^{-1} (green), and 100 x 10^{-4} m x s^{-1} (purple).
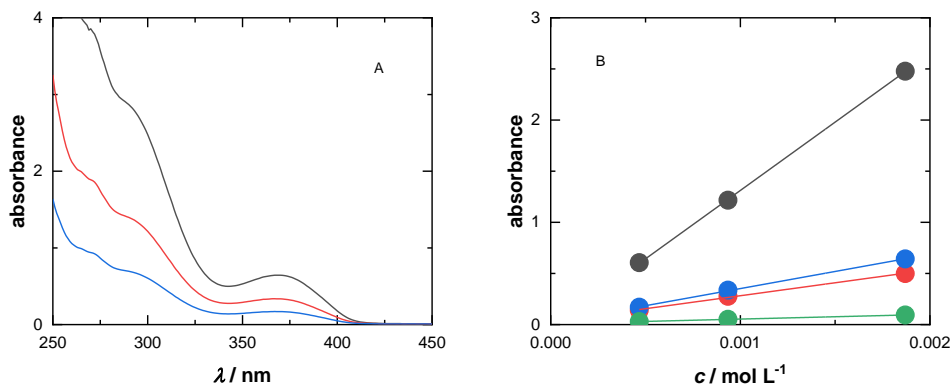
Figure 8.5.A) Absorbance spectra of LAP solution, c = 1.87 x 10^{-4} mol L^{-1} (black), c = 9.35 x 10^{-4} mol L^{-1} (red), c = 4.67 x 10^{-4} mol L^{-1} (blue) B) Calibration curves at 300 nm (black), 343 nm (blue) 366 nm(red), and 405 nm (green)
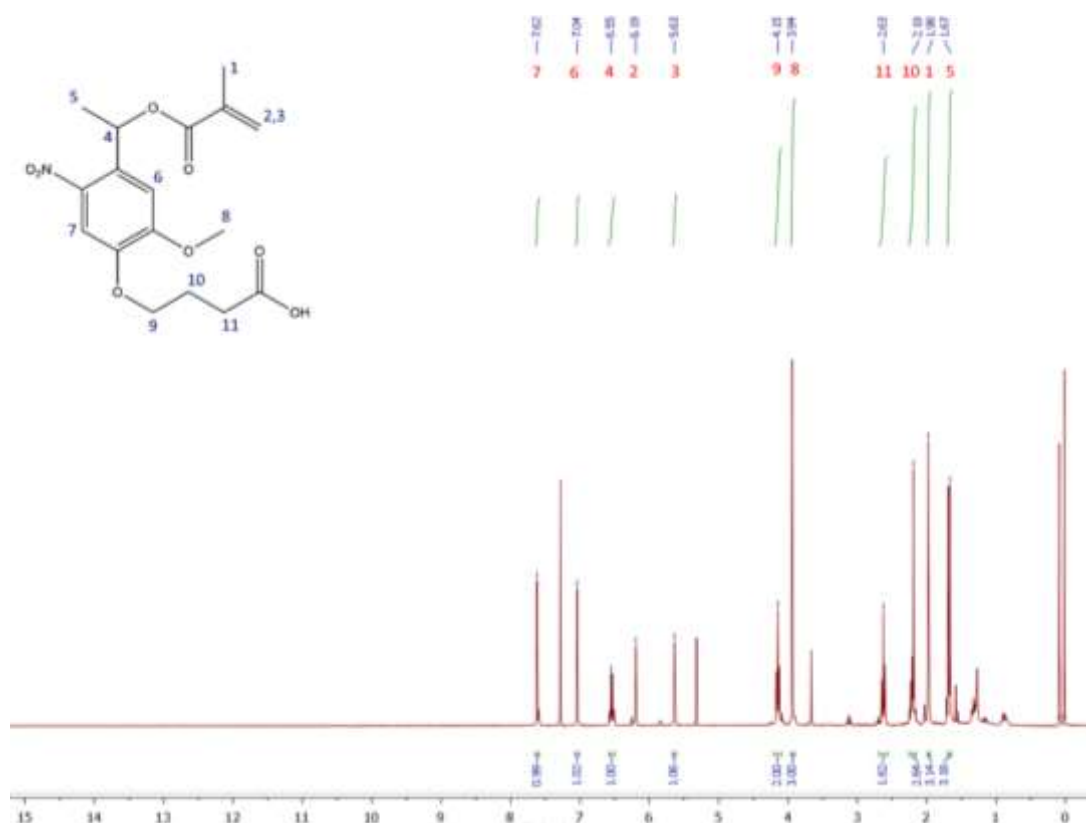
Figure 8.6. ¹H-NMR spectrum of the methacrylated o-nitrobenzylether moiety.
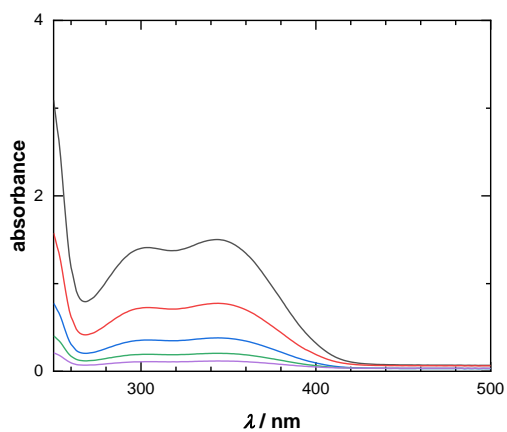
Figure 8.7.A) Absorption spectra of the aqueous solutions of the methacrylated o-nitrobenzylether moiety. $c = 5.37 \times 10^{-4}$ mol L^{-1} (black), $c = 2.68 \times 10^{-4}$ mol L^{-1} (red), $c = 1.34 \times 10^{-4}$ mol L^{-1} (blue), $c = 0.67 \times 10^{-4}$ mol L^{-1} (green), and $c = 0.34 \times 10^{-4}$ mol L^{-1} (purple)
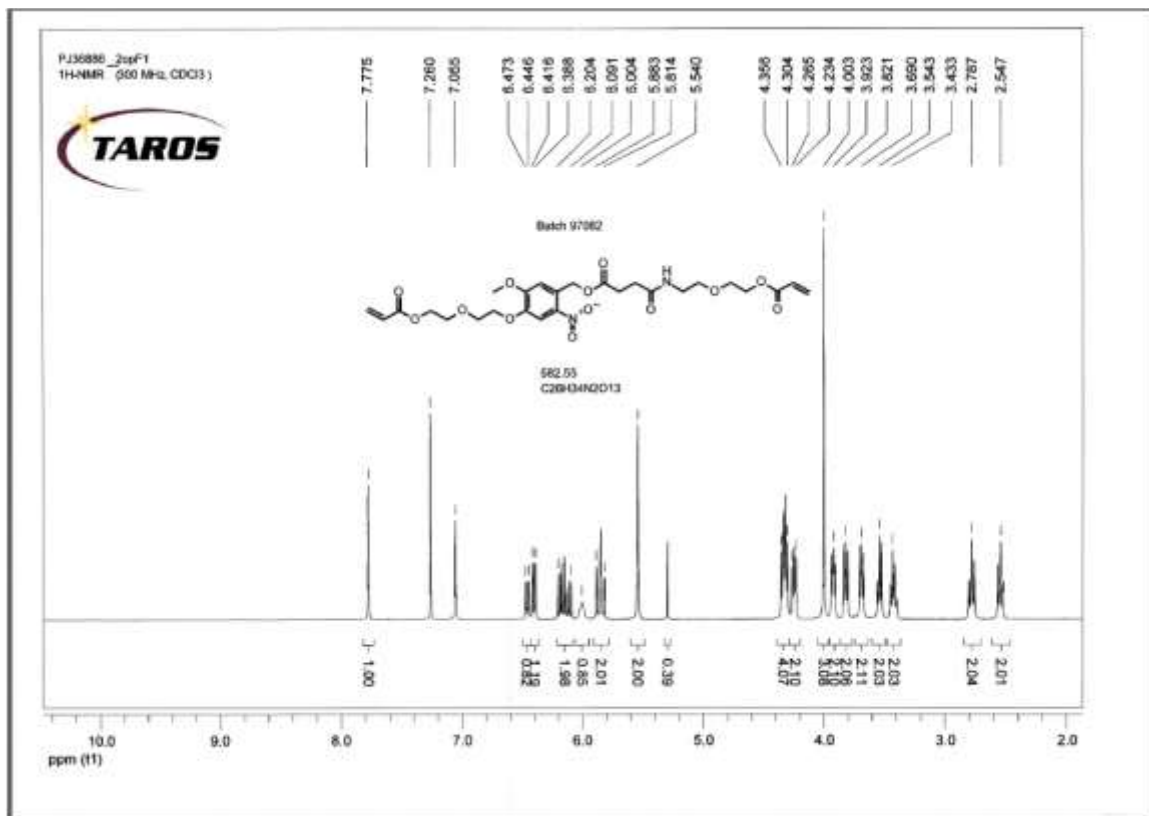
Figure 8.8. ^{1}H-NMR spectrum of PL$_{est}$
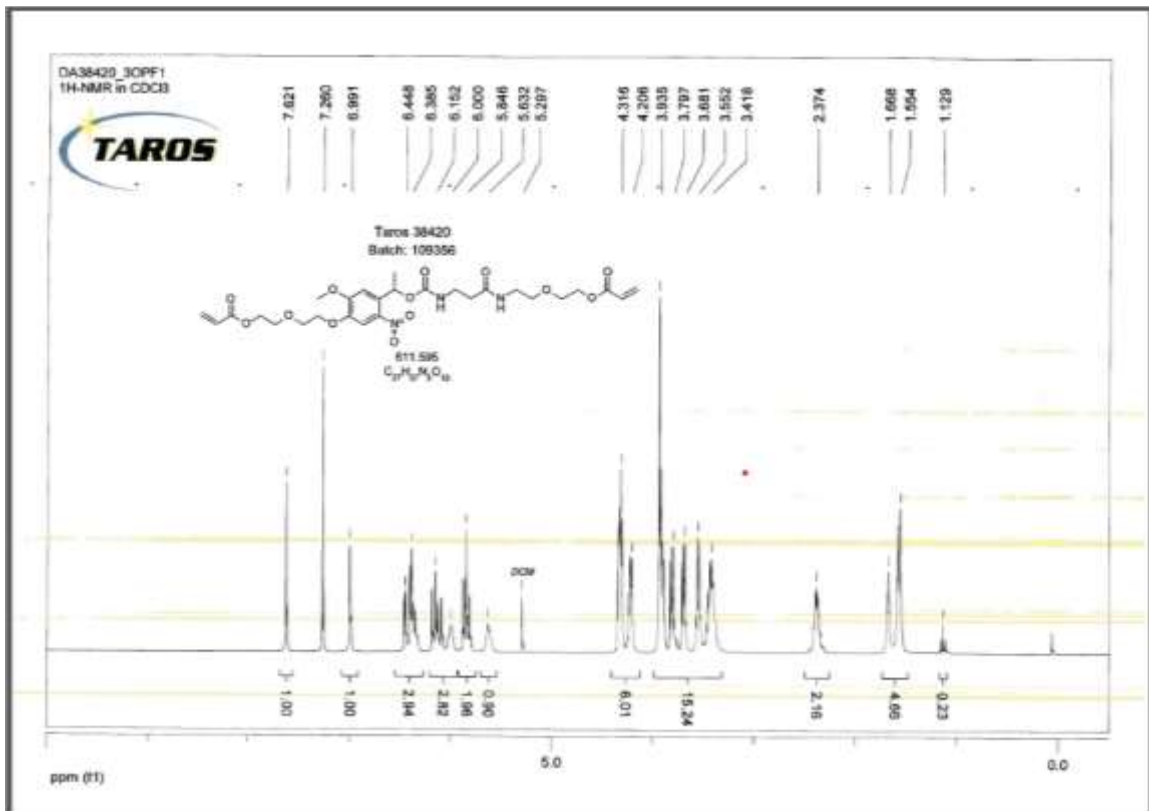
Figure 8.9. ^{1}H-NMR spectrum of PL$_{carb}$

8.2   List of Figures

125

8.3　List of Tables

8.4 List of Abbreviations

G	modulus
η	viscosity
σ	stress
γ	strain
$\dot{\gamma}$	shear rate
η_0	zero-shear viscosity
$\dot{\gamma}_{cr}$	critical strain rate
n	power-law index
K	flow consistency coefficient
σ_{max}	maximum stress
γ_{max}	maximum strain
δ	phase angle, solubility parameter
G^*	complex modulus
$\dot{\gamma}^*$	complex shear rate
ω	angular frequency
t	time
$\dot{\sigma}^*$	complex stress
τ_m	decay time
G'	storage modulus,
G''	loss modulus
η^*	complex viscosity
η'	real part of complex viscosity
η''	imaginary part of complex viscosity
v	flow rate,
ΔP	pressure drop
L	length
η_{cap}	capillary viscosity
F_η	viscous force
$\dot{\gamma}_{app}$	apparent wall shear rate
τ_{app}	apparent wall shear stress
$\dot{\gamma}_w$	true wall shear rate

τ_{w}	true wall shear stress
η_{w}	the true wall viscosity
c	concentration
c^{*}, c^{**}	critical concentrations
η_{∞}	infinite shear viscosity
λ	relaxation time
SN	single network
PEG	poly(ethylene glycol)
PAAm	poly(acrylamide)
PCL	poly(caprolactone)
LCST	lower critical solution temperature
UCST	upper critical solution temperature
PEGDA	poly(ethylene glycol) diacrylate
PEGDMA	poly(ethylene glycol) methacrylate
GelMA	gelatin methacrylate
MeHA	methacrylated hyaluronic acid
IPN	interpenetrating network
semi-IPN	semi-interpenetrating network
α	crosslinkling ratio
n_{monomer}	mole of monomer
$n_{\mathrm{crosslinker}}$	mole of crosslinker
G	gel content
Q_{m}	the mass swelling ratio
m_{sw}	swollen mass
m_{d}	dry mass
LVR	linear viscoelastic region
ω_{cross}	crossover frequency
G_0	plateau modulus
ρ	polymer density
R	universal gas constant
T	absolute temperature
M_{c}	molar mass between crosslinks
I2959	1-[4-(2-hydroxyethoxy)-phenyl]-2-hydroxy-2-methyl-1- propane-1-one
LAP	Lithium phenyl-2,4,6-trimethyl benzoyl phosphinate

VA-086	2,2'-azobis [2-methyl-N-(2-hydroxyethyl) propionamide]
Ru	Pentamethylcyclopentadienylbis (triphenylphosphine) ruthenium (II) chloride
APS	ammonium persulphate
PL	photo linker
NB	o-nitrobenzyl
LG	leaving group
DLS	dynamic light scattering
$\bar{M}_{PEG}$	the molar mass of PEG diols
$\bar{X}_n$	polymerization degree
$\bar{M}_n$	number-average molar mass
M_{CL}	mass of ε-cl
M_{MI}	molar mass of PEG macroinitiator
n_{CL}	moles of ε-CL
n_{EG}	moles of PEG
^{1}H-NMR	nuclear magnetic resonance spectroscopy
SEC	size exclusion chromatography
$\bar{M}_{n,theo}$	the theoretical total number-average molar mass
$\bar{M}_{n,NMR}$	the number-average molar mass calculated by ^{1}H-NMR
$\bar{M}_{n,SEC}$	the number-average molar mass calculated by SEC
χ	Huggin's constant
$\bar{n}_C$	the number of ε-CL repeating unit
$\bar{n}_E$	the number of ethylene glycol repeating unit
T_m	melting temperatures
T_c	crystallization temperatures
ΔH_m	melting enthalpy
D_h	hydrodynamic size
μ	mass fraction
μ^*, μ^{**}	critical mass fractions
m	slope
μ_e	entanglement mass fractions
BS	binary solution
R	radius
D	diameter
I	light intensity

d the layer thickness

I_0 initial light intensity, incident light intensity

A absorbance, area

ε molar extinction coefficient

k rate constant

ϕ quantum yield

N_A Avogadro's constant

υ frequency

V volume

h Planck's constant

q_m equilibrium mass swelling ratio

q_m^{UV} equilibrium mass swelling ratio upon the UV irradiation

m_0^{UV} swollen mass before UV exposure

E_p pulse energy

f_{rep} repetition rate
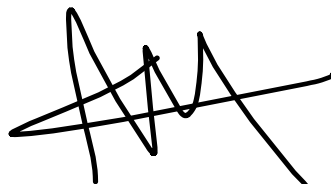
Erklärung zur Dissertation

gemäß der Promotionsordnung vom 12. März 2020

„Hiermit versichere ich an Eides statt, dass ich die vorliegende Dissertation selbstständig und ohne die Benutzung anderer als der angegebenen Hilfsmittel und Literatur angefertigt habe. Alle Stellen, die wörtlich oder sinngemäß aus veröffentlichten und nicht veröffentlichten Werken dem Wortlaut oder dem Sinn nach entnommen wurden, sind als solche kenntlich gemacht. Ich versichere an Eides statt, dass diese Dissertation noch keiner anderen Fakultät oder Universität zur Prüfung vorgelegen hat; dass sie - abgesehen von unten angegebenen Teilpublikationen und eingebundenen Artikeln und Manuskripten - noch nicht veröffentlicht worden ist sowie, dass ich eine Veröffentlichung der Dissertation vor Abschluss der Promotion nicht ohne Genehmigung des Promotionsausschusses vornehmen werde. Die Bestimmungen dieser Ordnung sind mir bekannt. Darüber hinaus erkläre ich hiermit, dass ich die Ordnung zur Sicherung guter wissenschaftlicher Praxis und zum Umgang mit wissenschaftlichem Fehlverhalten der Universität zu Köln gelesen und sie bei der Durchführung der Dissertation zugrundeliegenden Arbeiten und der schriftlich verfassten Dissertation beachtet habe und verpflichte mich hiermit, die dort genannten Vorgaben bei allen wissenschaftlichen Tätigkeiten zu beachten und umzusetzen. Ich versichere, dass die eingereichte elektronische Fassung der eingereichten Druckfassung vollständig entspricht."

Teilpublikationen:

-

25.09.2023, Caner Akıncı

Datum, Name und Unterschrift